ISSN 1997-308X
eISSN 2412-8767

ИЗВЕСТИЯ ВУЗОВ
ПОРОШКОВАЯ МЕТАЛЛУРГИЯ И ФУНКЦИОНАЛЬНЫЕ ПОКРЫТИЯ

POWDER METALLURGY AND FUNCTIONAL COATINGS

2023
Том 17 № 3
Vol. 17 No. 3
powder.misis.ru

ISSN 1997-308X
eISSN 2412-8767

POWDER METALLURGY AND FUNCTIONAL COATINGS

Scientific and Technical Journal
Founded in 2007
Four issues per year

2023
Vol. 17 No. 3
Том 17 № 3

ИЗВЕСТИЯ ВУЗОВ
ПОРОШКОВАЯ МЕТАЛЛУРГИЯ И ФУНКЦИОНАЛЬНЫЕ ПОКРЫТИЯ

Научно-технический журнал
Основан в 2007 г.
Выходит 4 раза в год

POWDER METALLURGY AND FUNCTIONAL COATINGS

SCIENTIFIC AND TECHNICAL JOURNAL
FOUNDED IN 2007
FOUR ISSUES PER YEAR

http://powder.misis.ru

ISSN 1997-308X
eISSN 2412-8767

Founder:

National University of Science
and Technology "MISIS"
Address: 4 bld. 1 Leninskiy Prosp., Moscow 119049, Russian Federation
http://www.misis.ru

Editor-in-Chief

Evgeny A. Levashov
Prof., Dr. Sci. (Eng.), Acad. of the RANS, NUST MISIS, Moscow, Russian Federation

Journal is included into the List of peer-reviewed scientific publications recommended by the Highest Attestation Commission of the Ministry of Education and Science of the Russian Federation for publishing the results of doctoral and candidate dissertations. Abstracting/Indexing: Scopus, Russian Science Citation Index (RSCI), Ulrich's Periodicals Directory, VINITI Database (Abstract Journal).

Editorial Board

M. I. Alymov – Dr. Sci. (Eng.), Corresponding Member of the RAS, Merzhanov Institute of Structural Macrokinetics and Materials Sciences of the RAS, Chernogolovka, Russia
A. P. Amosov – Prof., Dr. Sci. (Phys.-Math.), Samara State Technical University, Samara, Russia
G. A. Bagliuk – Prof., Dr. Sci. (Eng.), Acad. of the NASU, IPMS NASU, Kiev, Ukraine
I. V. Blinkov – Prof., Dr. Sci. (Eng.), NUST MISIS, Moscow, Russia
M. V. Chukin – Prof., Dr. Sci. (Eng.), Magnitogorsk State Technical University, Magnitogorsk, Russia
H. Danninger – Prof., Dr. Sci., Vienna University of Technology, Vienna, Austria
B. Derin – Assoc. Prof., Dr. Sci. (Phil.), Istanbul Technical University, Maslak, Istanbul, Turkey
V. Yu. Dorofeyev – Prof., Dr. Sci. (Eng.), South-Russian State Polytechnical University (NPI), Novocherkassk, Russia
Yu. Estrin – Prof., Dr. Sci. (Nat.), Monash University, Clayton, Australia
A. Ph. Ilyushchanka – Prof., Dr. Sci. (Eng.), Acad. of the NAS of Belarus, State Research and Production Powder Metallurgy Association, Minsk, Belarus
Yu. R. Kolobov – Prof., Dr. Sci. (Phys.-Math.), Federal Research Center of Problems of Chemical Pfysics and Medicinal Chemistry of the RAS, Chernogolovka, Russia
V. S. Komlev – Prof., Dr. Sci. (Eng.), Corresponding Member of the RAS, Institute of Metallurgy of the RAS, Moscow, Russia
I. Konyashin – Prof., Dr. Sci. (Econ.), Element Six GmbH, Burghaun, Germany
Yu. M. Korolyov – Prof., Dr. Sci. (Eng.), Scientific and Technical Association "Powder Metallurgy", Moscow, Russia
D. Yu. Kovalev – Dr. Sci. (Phys.-Math.), Merzhanov Institute of Structural Macrokinetics and Materials Sciences of the RAS, Chernogolovka, Russia
S. A. Kulinich – Assoc. Prof., PhD (Chem.), Tokai University, Hiratsuka, Kanagawa, Japan
S. V. Kuzmin – Prof., Dr. Sci. (Eng.), Corresponding Member of the RAS, Volgograd State Technical University, Volgograd, Russia
V. P. Kuznetsov – Prof., Dr. Sci. (Eng.), Ural Federal University, Ekaterinburg, Russia
Yu. V. Levinsky – Prof., Dr. Sci. (Eng.) Merzhanov Institute of Structural Macrokinetics and Materials Sciences of the RAS, Chernogolovka, Russia
A. E. Ligachyov – Prof., Dr. Sci. (Phys.-Math.), Prokhorov General Physics Institute of the RAS, Moscow, Russia
V. Yu. Lopatin – Cand. Sci., NUST MISIS, Moscow, Russia
A. A. Lozovan – Prof., Dr. Sci (Eng.), Moscow Aviation Institute (NRU), Moscow, Russia
V. I. Lysak – Prof., Dr. Sci. (Eng.), Acad. of the RAS, Volgograd State Technical University, Volgograd, Russia
A. V. Makarov – Dr. Sci. (Eng.), Corresponding Member of the RAS, M.N. Mikheev Institute of Metal Physics of the Ural Branch of the RAS, Ural Federal University, Ekaterinburg, Russia
L. L. Mishnaevsky – Dr. Habil. (Eng.), Technical University of Denmark, Roskilde, Denmark
A. S. Mukasyan – Prof., Dr. Sci. (Phys.-Math.), University of Notre Dame College of Engineering, Notre Dame, USA
S. A. Oglezneva – Prof., Dr. Sci. (Eng.), Perm National Research Polytechnical University, Perm, Russia
R. Orrù – Prof., Dr. Sci. (Eng.), University of Cagliari, Cagliari, Italy
I. B. Panteleev – Prof., Dr. Sci. (Eng.), St. Petersburg State Technological Institute (Technical University), St. Petersburg, Russia
F. Peizhong – Prof., Dr. Sci., China University of Mining and Technology, Xuzhou, P.R. China
C. Pengwan – Prof., Dr. Sci., Beijing Institute of Technology, Beijing, P.R. China
M. I. Petrzhik – Dr. Sci. (Eng.), NUST MISIS, Moscow, Russia
Yu. S. Pogozhev – Assoc. Prof., Cand. Sci. (Eng.), NUST MISIS, Moscow, Russia
V. V. Polyakov – Prof., Dr. Sci. (Phys.-Math.), Altai State University, Barnaul, Russia
A. A. Popovich – Prof., Dr. Sci. (Eng.)., Corresp. Member of the RANS, St. Petersburg State Polytechnical University (National Research University), St. Petersburg, Russia
S. E. Porozova – Dr. Sci. (Eng.), Perm National Research Polytechnical University, Perm, Russia
A. A. Rempel – Prof., Dr. Sci. (Phys.-Math.), Acad. of the RAS, Institute of Metallurgy of the Ural Branch of the RAS, Ekaterinburg, Russia
F. Rustichelli – Prof., Dr. Sci. (Phys.), University of Marches, Ancona, Italy
S. D. Shlyapin – Prof., Dr. Sci. (Eng.), Moscow Aviation Institute (NRU), Moscow, Russia
D. V. Shtansky – Dr. Sci. (Phys.-Math.), NUST MISIS, Moscow, Russia
A. N. Timofeev – Dr. Sci. (Eng.), JSC "Komposite", Korolev, Russia
P. A. Vityaz' – Prof., Dr. Sci. (Eng.), Acad. of the NAS of Belarus, Minsk, Belarus
A. A. Zaitsev – Assoc. Prof., Cand. Sci. (Eng.), NUST MISIS, Moscow, Russia
Zh. YongTing – Prof., Dr. Sci., Harbin Institute of Technology, Harbin, P.R. China
F. Zhengyi – Prof., Dr. Sci., Wuhan University of Technology, Wuhan, P.R. China

Editorial Staff

Address: NUST MISIS,
4 bld. 1 Leninskiy Prosp., Moscow 119049, Russian Federation

Phone: +7 (495) 638-45-35. ***E-mail:*** izv.vuz@misis.ru

Certificate of registration **No. FS77-27955** (12.04.2007)
Re-registration **PI No. FS77-79230** (25.09.2020)

PM & FC

© NUST MISIS, Moscow, 2023

Articles are available under Creative Commons Attribution Non-Commercial No Derivatives

Leading Editor: O.V. Sosnina
Executive Editor: A.A. Kudinova
Layout Designer: V.V. Rasenets

Signed print 20.09.2023. Format 60×90 $^1/_8$
Offset paper No. 1. Digital printing. Quires 10.0
Order 18135. Free price
Printed in the printing house of the MISIS Publish House
4 bld. 1 Leninskiy Prosp., Moscow, 119049 Russian Federation
Phone/fax: +7 (499) 236-76-17

ИЗВЕСТИЯ ВУЗОВ ПОРОШКОВАЯ МЕТАЛЛУРГИЯ И ФУНКЦИОНАЛЬНЫЕ ПОКРЫТИЯ

НАУЧНО-ТЕХНИЧЕСКИЙ ЖУРНАЛ
ОСНОВАН В 2007 Г.
ВЫХОДИТ 4 РАЗА В ГОД

http://powder.misis.ru

ISSN 1997-308X
eISSN 2412-8767

Учредитель: МИСИС УНИВЕРСИТЕТ НАУКИ И ТЕХНОЛОГИЙ

ФГАОУ ВО Национальный исследовательский технологический университет «МИСИС»
Адрес: 119049, Москва, Ленинский пр-т, 4, стр. 1
https://www.misis.ru

Главный редактор

Евгений Александрович Левашов
д.т.н., академик РАЕН, профессор, НИТУ МИСИС, г. Москва

Журнал включен в Перечень рецензируемых научных изданий, рекомендованных ВАК Минобрнауки РФ
для публикации результатов диссертаций на соискание ученых степеней.
Журнал включен в базы данных: Scopus, Russian Science Citation Index (RSCI), Ulrich's Periodicals Directory, РИНЦ, БД/РЖ ВИНИТИ.

Редакционная коллегия

М. И. Алымов – д.т.н., чл.-корр. РАН, проф., ИСМАН, г. Черноголовка
А. П. Амосов – д.ф.-м.н., проф., СамГТУ, г. Самара
Г. А. Баглюк – д.т.н., акад. НАНУ, проф., ИПМ НАН Украины, г. Киев
И. В. Блинков – д.т.н., проф., НИТУ МИСИС, г. Москва
П. А. Витязь – д.т.н., акад. НАНБ, проф., НАН Беларуси, г. Минск
В. Ю. Дорофеев – д.т.н., проф., ЮРГПУ (НПИ), г. Новочеркасск
А. А. Зайцев – к.т.н., доц., НИТУ МИСИС, г. Москва
А. Ф. Ильющенко – д.т.н., акад. НАН Беларуси, проф., ГНПО ПМ НАН Беларуси, г. Минск
Д. Ю. Ковалев – д.ф.-м.н., ИСМАН, г. Черноголовка
Ю. Р. Колобов – д.ф.-м.н., проф., ФИЦ ПХФ и МХ РАН, г. Черноголовка
В. С. Комлев – д.т.н., чл.-корр. РАН, проф., ИМЕТ РАН, г. Москва
Ю. М. Королев – д.т.н., проф., НТА «Порошковая металлургия», г. Москва
В. П. Кузнецов – д.т.н., проф., УрФУ, г. Екатеринбург
С. В. Кузьмин – д.т.н., чл.-корр. РАН, проф., ВолгГТУ, г. Волгоград
Ю. В. Левинский – д.т.н., проф., ИСМАН, г. Черноголовка
А. Е. Лигачев – д.ф.-м.н., проф., ИОФ РАН, г. Москва
А. А. Лозован – д.т.н., проф., МАИ (НИУ), г. Москва
В. Ю. Лопатин – к.т.н., доц., НИТУ МИСИС, г. Москва
В. И. Лысак – д.т.н., акад. РАН, проф., ВолгГТУ, г. Волгоград
А. В. Макаров – д.т.н., чл.-корр. РАН, ИФМ УрО РАН, УрФУ, г. Екатеринбург
С. А. Оглезнева – д.т.н., проф., ПНИПУ, г. Пермь
И. Б. Пантелеев – д.т.н., проф., СПбГТИ (ТУ), г. Санкт-Петербург
М. И. Петржик – д.т.н., проф., НИТУ МИСИС, г. Москва
Ю. С. Погожев – к.т.н., доц., НИТУ МИСИС, г. Москва
В. В. Поляков – д.ф.-м.н., проф., АлтГУ, г. Барнаул
А. А. Попович – д.т.н., чл.-корр. РАЕН, проф., СПбГПУ, г. Санкт-Петербург
С. Е. Порозова – д.т.н., проф., ПНИПУ, г. Пермь
А. А. Ремпель – д.ф.-м.н., акад. РАН, проф., ИМЕТ УрО РАН, г. Екатеринбург
А. Н. Тимофеев – д.т.н., АО «Композит», г. Королев, Московская обл.
М. В. Чукин – д.т.н., проф., МГТУ, г. Магнитогорск
С. Д. Шляпин – д.т.н., проф., МАИ (НИУ), г. Москва
Д. В. Штанский – д.ф.-м.н., проф. НИТУ МИСИС, г. Москва
C. Pengwan – Dr. Sci., Prof., Beijing Institute of Technology, Beijing, P.R. China
H. Danninger – Dr. Sci., Prof., Vienna University of Technology, Vienna, Austria
B. Derin – Dr. Sci. (Phil.), Assoc. Prof., Istanbul Technical University, Maslak, Istanbul, Turkey
Yu. Estrin – Dr. Sci. (Nat.), Prof., Monash University, Clayton, Australia
F. Peizhong – Dr. Sci., Prof., China University of Mining and Technology, Xuzhou, P.R. China
F. Zhengyi – Dr. Sci., Prof., Wuhan University of Technology, Wuhan, P.R. China
I. Konyashin – Dr. Sci. (Econ.), Prof., Element Six GmbH, Burghaun, Germany
S. A. Kulinich – PhD (Chem.), Associate Prof., Tokai University, Hiratsuka, Kanagawa, Japan
L. L. Mishnaevsky – Dr. Habil. (Eng.), Technical University of Denmark, Roskilde, Denmark
A. S. Mukasyan – Dr. Sci. (Phys.-Math.), Prof., University of Notre Dame College of Engineering, Notre Dame, USA
R. Orrù – Dr. Sci. (Eng.), Prof., University of Cagliari, Cagliari, Italy
F. Rustichelli – Dr. Sci. (Phys.), Prof., University of Marches, Ancona, Italy
Zh. YongTing – Dr. Sci., Prof., Harbin Institute of Technology, Harbin, P.R. China

Редакция журнала

Адрес: 119049, Москва,
Ленинский пр-т, 4, стр. 1. НИТУ МИСИС

Тел.: +7 (495) 638-45-35. ***Эл. почта:*** izv.vuz@misis.ru

Свидетельство о регистрации № **ФС77-27955** от 12.04.2007 г.
Перерегистрация 25.09.2020 г. **ПИ № ФС77-79230**

ПМ и ФП ИЗВЕСТИЯ ВУЗОВ

© НИТУ МИСИС, Москва, 2023

Статьи доступны под лицензией Creative Commons Attribution Non-Commercial No Derivatives

Ведущий редактор: О.В. Соснина
Выпускающий редактор: А.А. Кудинова
Дизайн и верстка: В.В. Расенець

Подписано в печать 20.09.2023. Формат 60×90 $^{1}/_{8}$
Бум. офсетная № 1. Печать цифровая. Усл. печ. л. 10,0
Заказ 18135. Цена свободная
Отпечатано в типографии Издательского Дома МИСИС
119049, г. Москва, Ленинский пр-т, стр. 1
Тел./факс: +7 (499) 236-76-17

Contents

Production Processes and Properties of Powders

Self-Propagating High-Temperature Synthesis

Refractory, Ceramic and Composite Materials

Porous Materials and Biomaterials

Materials and coatings fabricated using the additive manufacturing technologies

Nanostructured Materials and Functional Coatings

Содержание

Процессы получения и свойства порошков

Самораспространяющийся высокотемпературный синтез

Тугоплавкие, керамические и композиционные материалы

Пористые материалы и биоматериалы

Материалы и покрытия, получаемые методами аддитивных технологий

Наноструктурированные материалы и функциональные покрытия

Contents

Содержание

Production Processes and Properties of Powders
Процессы получения и свойства порошков

UDC 54.057; 537.226.86; 661

https://doi.org/10.17073/1997-308X-2023-3-6-13

Research article
Научная статья

Natural and thermally stimulated aging of nanosized powders of cobalt ferrospinel

A. A. Nevmyvaka[1], **V. A. Zhuravlev**[2], **V. I. Itin**[1]

[1] **Tomsk Scientific Center of the Siberian Branch of the Russian Academy of Sciences**
10/4 Akademicheskii Prosp., Tomsk 634055, Russia
[2] **National University Tomsk State University**
36 Lenina Prosp., Tomsk 634050, Russia

kaa151@mail.ru

Abstract. This article presents the production of nanosized powders of cobalt ferrospinel through mechanochemical synthesis, resulting in an average particle size ranging from 3 to 15 nm. The elemental composition of the nanopowders, analyzed using *X*-ray fluorescent analysis, is found to be nonstoichiometric and can be represented by the formula: $Co_{0.7\pm0.05}Fe_{2.3\pm0.05}O_4$. When the duration of mechanochemical synthesis exceeds 25 min, the spinel phase constitutes approximately 90 vol. % in the samples. Additionally, the samples contain hematite phases, the beta modification of iron hydroxide, and an *X*-ray amorphous phase. Natural aging at room temperature leads to significant changes in the phase composition of the nanopowders. Specifically, there is an increase in the content of spinel phase, while the content of hematite and the amorphous phase decrease significantly. Furthermore, the saturation magnetization and effective field of anisotropy of the cobalt ferrospinel nanopowders exhibit noticeable increments. Consequently, thermal aging of the powders accelerates the changes in phase composition, structural parameters, and magnetic properties, as well as enhances the transformation extent during the formation of cobalt ferrospinel.

Keywords: mechanochemical synthesis, cobalt ferrospinel, nanopowders, natural aging, thermally stimulated aging, magnetic anisotropy

Acknowledgements: The research was supported by the TSU Competitiveness Improvement Program (“Priority-2030”) and the Ministry of Science and Higher Education of the Russian Federation under project № 121031800148-5.

For citation: Nevmyvaka A.A., Zhuravlev V.A., Itin V.I. Natural and thermally stimulated aging of nanosized powders of cobalt ferrospinel. *Powder Metallurgy and Functional Coatings*. 2023;17(3):6–13. https://doi.org/10.17073/1997-308X-2023-3-6-13

Естественное и термостимулированное старение наноразмерных порошков феррошпинели кобальта

А. А. Невмывака[1], **В. А. Журавлев**[2], **В. И. Итин**[1]

[1] **Томский научный центр Сибирского отделения Российской академии наук**
634055, Россия, г. Томск, Академический пр-т, 10/4
[2] **Научно-исследовательский Томский государственный университет**
634050, Россия, г. Томск, Ленина пр-т, 36

kaa151@mail.ru

Аннотация. Методом механохимического синтеза получены наноразмерные порошки кобальтовой феррошпинели со средним размером частиц в интервале 3–15 нм. Элементный состав нанопорошков, исследованный методом рентгеновского флуоресцентного анализа, нестехиометрический и соответствует формуле $Co_{0,7\pm0,05}Fe_{2,3\pm0,05}O_4$. При времени механохимического синтеза 25 мин и выше содержание шпинельной фазы достигает 90 об. %, в образцах также присутствуют фазы гематита, бета-модификации гидроксида железа и рентгеноаморфной фазы. В результате естественного старения при комнатной температуре фазовый состав нанопорошков существенно меняется: увеличивается содержание шпинельной фазы, а гематита и аморфной фазы уменьшается в несколько раз. Также заметно возрастают намагниченность насыщения и эффективное поле анизотропии нанопорошков кобальтовой феррошпинели. Таким образом, термостимулированное старение порошков существенно ускоряет процессы изменения фазового состава, структурных параметров и магнитных свойств и увеличивает степень превращения при образовании феррошпинели кобальта.

Ключевые слова: механохимический синтез, кобальтовая феррошпинель, нанопорошки, естественное старение, термическое старение, магнитная анизотропия

Благодарности: Работа выполнена при поддержке Программы повышения конкурентоспособности ТГУ («Приоритет-2030) и Министерства науки и высшего образования Российской Федерации (проект № 121031800148-5).

Для цитирования: Невмывака А.А., Журавлев В.А., Итин В.И. Естественное и термостимулированное старение наноразмерных порошков феррошпинели кобальта. *Известия вузов. Порошковая металлургия и функциональные покрытия*. 2023;17(3): 6–13. https://doi.org/10.17073/1997-308X-2023-3-6-13

Introduction

Mechanochemical synthesis involves the mechanical processing of solid mixtures, leading to various processes such as substance disintegration, accelerated mass transfer, homogenization of mixture components, and activation of chemical interactions among solid reagents. The utilization of mechanical grinding in planetary high-energy mills has proven to be an effective method for producing powders, including magnetic powders, with microcrystalline unit sizes reaching as low as 10 nm or even lower. This approach facilitates the acceleration of interactions between nanocrystalline particles, which becomes particularly significant in the synthesis of multicomponent systems. In such cases, both mechanical and chemical forces come into play within the contact area between particles [1–9].

Finely dispersed magnetic powders with the particle sizes up to 10 nm garnered significant attention from researchers [10]. The small sizes of these powders and their unique properties make them suitable for targeted delivery of genetic material and medications to injured organs, enhancing magnetic resonance imaging contrast and other applications [11].

However, nanosized magnetic powders suffer from agglomeration, which tends to increase as the particle size decreases. Ultrasonic treatment in a liquid phase has proven effective in mitigating this drawback. It is worth noting that extended operation or storage leads to changes in physicochemical properties, commonly referred to as aging.

The phenomenon of aging in ferromagnetic materials exhibits universal characteristics. A study [12] investigated universality in various nonequilibrium lattice models with second-order phase transitions. Experimental data obtained from systems quenched from a high-temperature state at the critical temperature were utilized.

The exponent of the autocorrelation function and the asymptotic value of the dissipation coefficient were identified as universal variables. Monte Carlo simulation were conducted to analyze these universal variables in different lattice models.

Aging effects were further examined in [13; 14] for a specific case involving behavior of multilayer magnetic structures. The study revealed that aging effects occur not only during nonequilibrium critical behavior at $T = T_c$, (where T_c represents the critical temperature of ferromagnetic ordering) but also in wide temperature range with $T \leq T_c$. In such magnetic structures, such as films with nanosized layers, an increase in the relaxation time results in deceleration of correlation and relaxation properties. These effects must be considered in the development and utilization of various magnetic structures.

Subsequent research by these authors [15] focused on calculating the temperature dependencies of equilibrium magnetic resistance values for a multilayer structure Co/Cu(100)/Co with varying thicknesses of cobalt magnetic layers. The theoretical results exhibited good agreement with experimental data, indicating an increase in the magnetic resistance coefficient in accordance with magnetic laws as temperature decreases and cobalt layer thickness increases.

The relaxation behavior of magnetization in the magnetic superstructure Co/Cu was investigated in [16]. The authors' analysis demonstrated that the relaxation behavior follows the pattern of full aging. The relaxation index, as a function of temperature, reveals distinct abnormalities during the equilibrium phase transition from an antiferromagnetic superstructure to paramagnetic layers.

Significant interest lies in studies examining the influence of aging on ferromagnetism in hydrogen-induced magnetic semiconductors with high Curie point [17]. It is known that these compounds exhibit a substantial increase in magnetization at 300 K after hydrogenation, particularly in cobalt- and iron-doped ZnO. The induced magnetization in paramagnetic ZnCo(5 %)O and ZnFe(5 %)O granules largely diminishes during storage due to material degradation.

In most cases, aging in materials is caused by decomposition of oversaturated solid solutions [18]. Depending on how the crystalline lattice constant changes, decomposition mechanisms can be categorized as continuous or discontinuous. Single-phase decomposition occurs when only one set of X-ray reflections from lattice of the initial solid solution is observed, while discontinuous decomposition involves a dropwise change in the lattice constant and the appearance of multiple sets of X-ray reflections.

In massive ferromagnetic materials undergoing single-phase aging, a single Curie point is observed, and its position gradually shifts with aging. In the case of two-phase aging, two Curie points exist, but one of them diminishes over time [18].

This study explores the influence of natural aging (at ambient temperature) and thermally stimulated aging (resulting from annealing at different temperatures) on the chemical and phase compositions, structural parameters, and key magnetic properties of nanosized powders of cobalt ferrospinel.

Experimental

In order to synthesize cobalt ferrospinel nanoparticles, the following reaction was employed:

$$2FeCl_3{\cdot}6H_2O + CoCl_2 + Ca(OH)_2 + 3Na_2CO_3 =$$
$$= CoFe_2O_4 + CaCl_2 + 6NaCl + 3CO_2{\uparrow} + 7H_2O.$$

The initial reagents used were of high purity, including pure, chemically pure, and pure for analysis grades. Furthermore, an inert component, sodium chloride, was added to the system in weight ratio of $m_{\text{r.m.}} : m_{\text{NaCl}} = 1:2$. This addition aimed to reduce the heating degree of reacting mixture (r.m) and thereby prevent particles aggregation in the final product. Subsequently, the system comprising the initial reagents and the inert component was placed in steel quenched barrels of a planetary mill with water cooling (acceleration: 60g). The ball to powder weigh ratio was maintained atc 20:1. The duration of mechanical processing or mechanochemical activation was varied between 5 and 60 min.

After the completion of mechanic activation, the resulting final product was extracted from the planetary mill barrels, washed with distilled water using a centrifuge (ROTANTA 430R, «Hettich», Germany) until all salts were completely removed, and dried at room temperature.

Natural aging of the cobalt ferrospinel nanosized powder was achieved through maturation in an exicator for 25 and 10,000 h, while thermally stimulated aging was conducted in an electric furnace over a temperature range of 100–600 °C for 60 min.

The chemical and phase compositions, morphology, dispersity, structure parameters, and magnetic properties of the cobalt ferrospinel nanopowders were analyzed following the procedures outlines in references [19–21].

Result and discussion

Electron microscopy images of cobalt ferrospinel nanoparticles and a histogram depicting the distribution of particle sizes can be found in references [20; 22]. The analysis revealed that the nanoparticles, ranging in size from 3 to 15 nm, exhibit a spherical shape and tend to aggregate weakly.

These results were corroborated and validated at the Engelgardt Institute of Molecular Biology, Russian Academy of Sciences (Moscow) during an investigation into the impact of cobalt ferrite magnetic particles on the spatial arrangement of DNA molecules [20]. By utilizing specially prepared suspensions and electron microscopy, the authors determined the average nanoparticle size to be within the range of 4.0 to 6.5 nm, consistent with the previously obtained results at the Tomsk Scientific Center, Siberian Branch, Russian Academy of Sciences. Furthermore, it was observed that the cobalt ferrospinel nanoparticles tend to form aggregates. Structural analysis using small-angle X-ray scattering indicated that the distribution of nanoparticle sizes encompasses particles with radii in the ranges of both 1 to 4 nm and 5 to 15 nm, which aligns with the observations made in reference [20].

The elemental composition of the synthesized nanosized powders of cobalt ferrospinel conforms to the formula $Co_{0.7\pm0.05}Fe_{2.3\pm0.05}O_4$. In addition to the main components, the powder contains impurities of manganese up to 0.15 wt. % and chromium up to 0.3–0.4 wt. %, which originated from the wear of steel balls. Consequently, X-ray fluorescent analysis demonstrated that the chemical composition of cobalt ferrospinel deviates significantly from its stoichiometric composition.

Figure 1 depicts the phase composition of cobalt ferrospinel as a function of the duration of mechanochemical processing.

For short duration of processing, the samples exhibit significant heterogeneity. Alongside the spinel phase, the presence of hematite and the beta modification of iron hydroxide phase is observed, along with approximately 10 % of X-ray amorphous phase. However, as the processing duration reached 25 min and beyond, the volume fraction of the spinel phase increases and stabilizes at around 90 %.

In order to assess the effects of natural aging, the structural and magnetic properties of cobalt ferrospinel were compared immediately after synthesis (within one day) with those after being held at ambient temperature for approximately 14 months (over 10,000 h). Table 1 provides a summary of the phase composition and structural properties of cobalt ferrite during natural aging.

During the maturation process of the nanopowders for over 10,000 h, a significant transformation in the phase composition is observed. The aged product no longer contains any traces of the hematite phase or the beta modification of iron hydroxide phase (β-FeO(OH)). Additionally, the content of the amorphous phase decreases substantially, from 3.0 to 1.0 vol. %, while the main product, the spinel phase, increases to 99 vol. % (refer to Table 1). The lattice constant of the nanopowders experiences a slight decrease, and the elastic microstresses, which are initially very high after mechanochemical synthesis of the nanosized powders, exhibit a reduction. The average particle size only changes by a maximum of 5–9 %.

Table 2 summarizes the magnetic properties of the synthesized nanopowders. The specific saturation magnetization (σ, Gs·cm^3/g) is estimated using two methods. In the third column, the magnetization is determined by linear extrapolation of the high field segment of σ(*H*) to zero magnetizing field ($H \to 0$), while in the fourth column, it is determined by extrapolating $\sigma(H^{-1})$ to its value at $H \to \infty$.

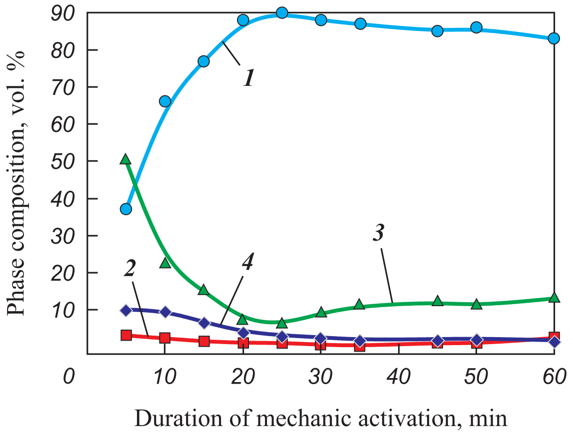

Fig. 1. The phase composition of cobalt ferrospinel as a function of the duration of mechanochemical synthesis
1 – cobalt ferrospinel, ***2*** – α-Fe_2O_3,
3 – β-FeO(OH), ***4*** – amorphous phase

Рис. 1. Зависимость фазового состава от продолжительности механохимического синтеза для кобальтовой феррошпинели
1 – кобальтовая феррошпинель, ***2*** – α-Fe_2O_3,
3 – β-FeO(OH), ***4*** – аморфная фаза

The effective fields of magnetic anisotropy (H_A) are determined by studying the second derivative of the magnetization curve, σ(*H*), following the procedure outlined in reference [21]. The effective constants of magnetic anisotropy (K_{eff}) for the materials under consideration are calculated using the equation:

$$H_A = \frac{2K_{eff}}{M_S},$$

where $M_S = \sigma\rho$ represents the saturation magnetization of unit volume in A/m and ρ denotes the specific weight of the synthesized powders in N/m^3.

The specific magnetization of the nanopowders and the field intensity of effective magnetic anisotropy experience significant changes during 10,000 h natural aging period at ambient temperature. The magnetization of the aged samples increases by approximately 14 % for cobalt ferrospinel (refer to Table 2). This increase in magnetization exceeds what can be attributed solely to changes in phase composition resulting from the transformation of nonmagnetic amorphous phase and antiferromagnetic hematite into the spinel phase.

It is plausible to assume that this effect is associated either with a decrease in the thickness of the nonmagnetic ("dead") surface layer of the ferrospinel nanoparticles or with a substantial reduction in the defect structure of the nanoparticle's crystalline structure upon aging. Notably, during natural aging, the value of the effective field of anisotropy for cobalt ferrospinel increases significantly. This increase can be attributed to the magnetic anisotropy primarily formed by the contribution of Co^{2+} ions, which exhibit a strong spin-orbital interaction (see Table 2).

Thermal processing can greatly stimulate diffusion processes responsible for changes in phase composition, structural parameters, and magnetic properties in nanosized ferrimagnetic powders. Therefore, in this study, powders of cobalt ferrite obtained with varying durations of mechanochemical processing were subjected to homogenizing annealing at temperatures of 100, 300 and 600 °C.

Table 1. **The influence of aging at ambient temperature on phase composition and structural properties of cobalt ferrospinel**

Таблица 1. **Влияние продолжительности старения при комнатной температуре на фазовый состав и структурные параметры кобальтовой феррошпинели**

Aging duration, h	Phase composition, vol.%				Lattice constant *a*, nm	Average particle size*, nm		Δ*d*/*d*, 10^{-3}
	Spinel	Hematite	β-FeO(OH)	Amorphous phase		TEM	XSA	
25	90.0	1.0	6.0	3.0	0.8376	8.5	9.2	8.8
> 10,000	99.0	–	–	1.0	0.8370	–	9.6	7.2

* According to transmission electron microscopy (TEM) and *X*-ray structural analysis (XSA).

Table 2. **The influence of aging and annealing temperature on basic magnetic properties of cobalt ferrospinel**

Таблица 2. **Влияние продолжительности старения и температуры отжига после синтеза на основные магнитные характеристики кобальтовой феррошпинели**

Annealing temperature, °C	Aging duration, h	Specific magnetization σ, Gs·cm^3/g		H_A, Oe	$K_{eff}\cdot 10^5$, erg·cm^3
		$H \to 0$	$H \to \infty$		
20	25	22.3	36.1	1740	2.07
20	10,000	31.0	41.4	2300	1.75
100	25	55.4	–	1750	–
300	25	60.6	–	2500	–
600	25	58.8	–	4250	–

Figure 2 depicts the relationship between the content of the spinel phase, average sizes of crystallites, internal elastic microstresses, and specific saturation magnetization for cobalt ferrospinel. It presents these parameters as a function of both the duration of synthesis and the annealing temperature.

Annealing at a temperature of 100 °C has a minimal impact on the structural properties of cobalt ferrospinel. It primarily results in a slight increase in the content of the spinel phase. However, at higher annealing temperatures, there is a notable increase in the average particle size and a significant (around 3–5 times) reduction in the internal elastic microstresses. These changes in structural parameters subsequently have a substantial effect on the magnetic properties of ferrimagnetic nanopowders.

Table 2 provides a summary of the main magnetic properties, including the specific saturation magnetization and the effective field of magnetic crystallographic anisotropy, for nanosized powders of cobalt ferrite. These properties are analyzed in relation to the duration of mechanochemical synthesis and various modes of thermal processing.

The increase in magnetization is most pronounced in samples synthesized in less than 25 min. This increase can be attributed to the growth in average particle size, leading to a reduction in the relative volume of the "dead" surface layer and a decrease in the extent of the defect structure within crystallites. The dependences of the effective field of magnetic anisotropy are more complex, as they involve a competition between volumetric and surface anisotropy, as well as contribution of magnetoelastic interactions.

Changes in the effective field of magnetic anisotropy of cobalt ferrospinel nanoparticles upon aging warrant individual discission. As reported in [23], the effective

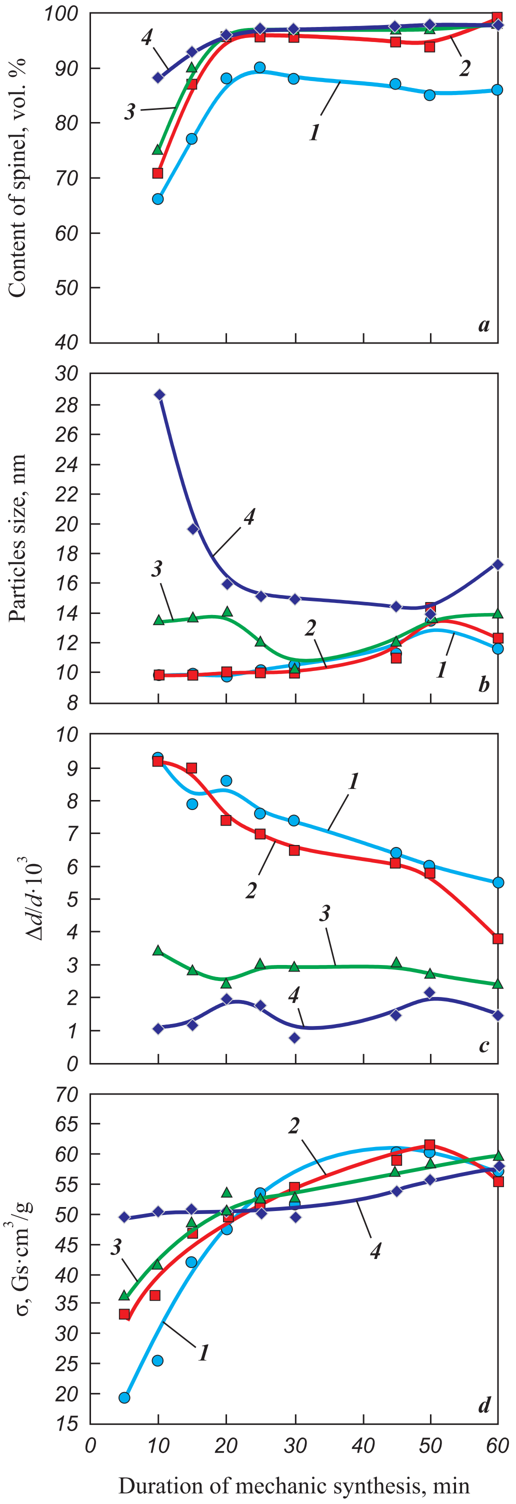

Fig. 2. The content of the spinel phase (***a***), average particle size (***b***), internal elastic microstresses (***c***) and saturation magnetization (***d***) as a function of mechanochemical synthesis time and subsequent heat treatment temperature
1 – *t* = 20 °C, ***2*** – 100 °C, ***3*** – 300 °C, ***4*** – 600 °C

Рис. 2. Зависимости содержания шпинельной фазы (***a***), среднего размера частиц (***b***), внутренних упругих микронапряжений (***c***) и намагниченности насыщения (***d***) от продолжительности механохимического синтеза и температуры последующей термической обработки
1 – *t* = 20 °C, ***2*** – 100 °C, ***3*** – 300 °C, ***4*** – 600 °C

constant of magnetic anisotropy of the nanoparticles can be expressed as the sum of the following components:

$$K_{eff} = K_{\text{MKA}} + \lambda_S \sigma = \left(1 - \frac{V_S}{V_V}\right) K_V + \frac{V_S}{V_V} K_S + \lambda_S \sigma,$$

where the first and the second terms account for the contributions of volumetric and surface magnetocrystalline anisotropies, respectively, while the latter term represents the contribution of magnetoelastic interactions. Here K_V and K_S denote the constants of anisotropy for the internal volume and surface layer, respectively; λ_S is the coefficient of ferrimagnetic magnetostriction; $\sigma = (\Delta d/d)E$ represents the value of internal elastic microstresses, where E is the Young modulus; V_S is the volume of the excited surface layer; V_V is the non-excited internal volume.

Considering the negligible changes in the sizes of ferromagnetic particles during natural aging, the field changes, and hence the effective constant of anisotropy, are primarily governed by the decrease in internal elastic microstresses with aging. This implies a change in the contribution of the magnetoelastic component to the total energy of crystal anisotropy. Consequently, the magnetostriction coefficient for nanosized powders of ferrimagnetic compounds can be estimated using the following equation

$$\lambda_S = \delta H_{\text{A}} \frac{M_S}{2E} \delta \frac{\Delta d}{d},$$

where δH_{A} denotes the change in the field of magnetic anisotropy during aging.

The magnetostriction constant obtained for cobalt ferrite nanoparticles is $68 \cdot 10^{-6}$, which is approximately half the value observed for massive crystals. It should be noted that estimating such values for materials after annealing is problematic due to difficulties in separating the contributions of surface anisotropy and magnetoelastic interactions.

Table 3. **The chemical composition of cobalt ferrospinel nanopowders as a function of the duration of mechanochemical activation**

Таблица 3. **Влияние времени активации нанопорошков кобальтовой феррошпинели на ее химический состав**

Duration of mechanic activation, min	Content, at. %		Chemical formula
	Fe	Co	
10	43.34	23.04	$Co_{1.04}Fe_{1.96}O_4$
20	48.95	17.94	$Co_{0.80}Fe_{2.2}O_4$
30	14.73	48.94	$Co_{0.69}Fe_{2.31}O_4$

Therefore, nanosized powders of oxide ferrimagnetic materials produced through mechanochemical synthesis exist in a metastable state and tend to transition into a stable state during aging at ambient temperature. The evolution of phase composition, structural parameters, and magnetic properties provides evidence of relaxation processes upon aging.

One such processes is crystallization of the amorphous phase, although its influence on changes in phase composition and magnetic properties is minimal due to its negligible content compared to the spinel phase. Regarding hematite, its absence after aging is likely due to its dissolution in the spinel phase.

X-ray fluorescent analysis of the elemental phase of the synthesized samples revealed that, in all cases after mechanochemical synthesis, the concentrations of components do not correspond to their stoichiometric ratio (Table 3). Furthermore, the cubic lattice is maintained, with a lattice constant lower than that of materials in bulk form, and the elastic stresses are very high.

It can be hypothesized that over prolonged aging, hematite undergoes dissolution in the spinel phase through solid-phase diffusion under high stress conditions. Consequently, the chemical composition of the ferrimagnetic material approaches stoichiometry. Substantial evidence supporting this notion includes a notable increase in specific saturation magnetization and alterations in the effective field of magnetic anisotropy. The primary processes governing the changes in magnetic properties of nanosized powders during thermally stimulated aging are the reduction in the significance of the surface layer and the extent of magnetic defect structure.

Conclusions

1. It has been experimentally shown that cobalt ferrite nanoparticles synthesized through mechanochemical methods using iron chloride (III) crystallohydrate exhibit weak agglomeration, a spherical shape, and sizes in ranging from 3 to 15 nm. The elemental composition of the synthesized nanopowders is non-stoichiometric and can be described by the formula: $Co_{0.7\pm0.05}Fe_{2.3\pm0.05}O_4$.

2. *X*-ray fluorescent analysis (XFA) reveals significant changes in the phase composition of cobalt ferrite nanopowders during aging (>10,000 h after synthesis at ambient temperature):

– the content of the desired product (spinel phase) increases to 99.0 vol. %;

– no impurity phases of hematite and iron hydroxide are detected;

– the final product after aging only exhibits traces of an amorphous phase.

3. Both natural and thermally stimulated aging result to an increase in the average particle size and a significant decrease in internal elastic microstresses (indicating a reduction in the defect structure of cobalt ferrite nanopowders).

4. Aging is accompanied by a significant increase in saturation magnetization due to an increase in the content of the ferrimagnetic phase and a decrease in the fraction of the surface "dead" layer and the defect structure of the ferrimagnetic material.

References / Список литературы

1. Boldyrev V.V. Research on the mechanochemistry of solid. *Vestnik Rossiiskogo fonda fundamental'nykh issledovanii*. 2004;3(37):38–59. (In Russ.).

Болдырев В.В. Исследования по механохимии твердых веществ. *Вестник Российского фонда фундаментальных исследований*. 2004;3(37):38–58.

2. Michalchuk A.L., Boldyreva E.V., Belenguer A.M., Emmerling F., Boldyrev V.V. Tribochemistry, mechanical alloying, mechanochemistry: What is in a name? *Frontiers in Chemistry*. 2021;9:685789. https://doi.org/10.3389/fchem.2021.685789

3. Takacs L. The historical development of mechanochemistry. *Chemical Society Reviews*. 2013;42(18):7649–7659. https://doi.org/10.1039/C2CS35442J

4. Ghada A.Al Bazedi, Aiman Eid Al-Rawajfeh, Mona A. Abdel-Fatah, Mohammad R. Alrbaihat, Ehab AlShamaileh. Synthesis of nanomaterials by mechanochemistry. In: *Handbook of greener synthesis of nanomaterials and compounds. Vol. 1: Fundamental principles and methods*. Elsevier, 2021. P. 405–418. https://doi.org/10.1016/B978-0-12-821938-6.00011-6

5. Delogu F., Gorrasi G., Sorrentino A. Fabrication of polymer nanocomposites via ball milling: Present status and future perspectives. *Progress in Materials Science*. 2017;86: 75–126. https://doi.org/10.1016/j.pmatsci.2017.01.003

6. Avvakumov E., Senna M., Kosova N. Soft mechanochemical synthesis: a basis for new chemical technologies. Boston, Dordrecht, London: Kluver Academic Publ., 2001. 208 p. https://doi.org/10.1007/b114163

7. Gubin S.P., Koksharov Yu.L., Khomutov G.B., Yurkov G.Yu. Magnetic nanoparticles: preparation, structure and properties. *Russian Chemical Reviews*. 2005;74(6): 489–520.

Губин С.П., Кокшаров Ю.Л., Хомутов Г.Б., Юрков Г.Ю. Магнитные наночастицы: методы получения, структура и свойства. *Успехи химии*. 2005;74(6):539–574.

8. Said M. Al Azar, Ahmad A. Mousa. Mechanical and physical methods for the metal oxide powders production. In: *Metal oxide powder technologies*. Elsevier, 2020. P. 169–187. https://doi.org/10.1016/B978-0-12-817505-7.00008-7

9. Tsuzuki T. Mechanochemical synthesis of nanoparticles. In: *Encyclopedia of Nanomaterials*. 1st Ed. Elsevier, 2023. P. 39–47. https://doi.org/10.1016/B978-0-12-822425-0.00058-0

10. Gusev A.I., Rempel A.A. Nanocrystalline Materials. Cambridge International Science Publishing, 2004. 351 p.

Гусев А.И., Ремпель А.А. Нанокристаллические материалы. М.: Физматлит, 2001. 224 с.

11. Mikhaylov G., Mikac U., Magaeva A.A., Itin V.I., Naiden E.P., Psakhye I., Babes L., Reinheckel T., Peters Ch., Zeiser R., Bogyo M., Turk V., Psakhye S.G., Turk B., Vasiljeva O. Ferri-liposomes as an MRI-visible drug-delivery system for targeting tumours and their microenvironment. *Nature Nanotechnology*. 2011;6(9):594–602. https://doi.org/10.1038/nnano.2011.112

12. Chatelain Ch. On universality in ageing ferromagnets. *Journal of Statistical Mechanics: Theory and Experiment*. 2004;6:P06006. https://dx.doi.org/10.1088/1742-5468/2004/06/P06006

13. Prudnikov V.V., Prudnikov P.V., Purtov A.N., Mamonova M.V. Aging effects in the nonequilibrium behavior of multilayer magnetic superstructures. *JETP Letters*. 2016;104(11):776–783. https://doi.org/10.1134/S0021364016230132

Прудников В.В., Прудников П.В., Пуртов А.Н., Мамонова М.В. Эффекты старения в неравновесном поведении многослойных магнитных сверхструктур. *Письма в журнал экспериментальной и теоретической физики*. 2016;104(11–12):797–805.

14. Prudnikov V.V., Prudnikov P.V., Mamonova M.V. Non-equilibrium critical behavior of model statistical systems and methods for the description of its features. *Physics-Uspekhi*. 2017;60(8):762–797. https://doi.org/10.3367/UFNe.2017.02.038067

Прудников В.В., Прудников П.В., Мамонова М.В. Особенности неравновесного критического поведения модельных статистических систем и методы их описания. *Успехи физических наук*. 2017;187(8):817–855. https://doi.org/10.3367/UFNr.2017.02.038067

15. Prudnikov V.V., Prudnikov P.V., Mamonova M.V. Aging effects in the nonequilibrium behavior of magnetic superstructures and their manifestation in magnetoresistance. *Journal of Experimental and Theoretical Physics*. 2018;127(4):731–741. https://doi.org/10.1134/S1063776118100060

Прудников В.В., Прудников П.В., Мамонова М.В. Эффекты старения в неравновесном поведении магнитных сверхструктур и их проявление в магнитосопротивлении. *Письма в журнал экспериментальной и теоретической физики*. 2018;154(4(10)):855–867. http://dx.doi.org/10.1134/S0044451018100140

16. Mukherjee T., Pleimling M., Binek Ch. Probing equilibrium by nonequilibrium dynamics: Aging in Co/Cr superlattices. *Physical Review B*. 2010;82(13):134425. https://doi.org/10.1103/PhysRevB.82.134425

17. Singhal R.K., Samariya A., Kumar S., Xing Y.T., Saitovitch E. Influence of ageing on H-induced ferromagnetism in $Zn_{1-x}M_xO$ (M = Co, Fe, Mn). *Materials Letters*. 2010;64(16):1846–1849. https://doi.org/10.1016/j.matlet.2010.05.016

18. Encyclopedia of inorganic materials. Vol. 2. Kyiv: Glavnaya redaktsiya Ukrainskoi sovetskoi entsiklopedii. 1977. 816 p.

Энциклопедия неорганических материалов. Т. 2. Киев: Главная редакция Украинской советской энциклопедии, 1977. 816 с.

19. Naiden E.P., Itin V.I., Magaeva A.A., Terekhova O.G., Kostikova V.A., Zagrebin L.V., Shestov S.S. Effect of conditions of the mechanochemical synthesis and heat treatment on the phase composition, structural parameters, and magnetic properties of nanodimensional powders of cobalt spinel ferrite. *Russian Journal of Non-Ferrous Metals*. 2012;53(5):399–403.
https://doi.org/10.3103/S1067821212050100

Найден Е.П., Итин В.И., Магаева А.А., Терехова О.Г., Костикова В.А., Загребин Л.В., Шестов С.С. Влияние условий механохимического синтеза и термической обработки на фазовый состав, структурные параметры и магнитные свойства наноразмерных порошков феррошпинели кобальта. *Известия вузов. Порошковая металлургия и функциональные покрытия*. 2011;(1):3–8.

20. Yevdokimov Yu.M., Pershina A.G., Salyanov V.I., Magaeva A.A., Popenko V.I., Shtykova E.V., Dadinova L.A., Skuridin S.G. Superparamagnetic cobalt ferrite nanoparticles “blow up” the spatial ordering of double-stranded DNA molecules. *Biophysics*. 2015;60(3):341–347.
https://doi.org/10.1134/S0006350915030057

21. Kreslin V.Yu., Naiden E.P. Automatic complex for a study of the characteristics of hard magnetic materials. *Instruments and Experimental Techniques*. 2002;45(1):55–57.
https://doi.org/10.1023/A:1014548225622

Креслин В.Ю., Найден Е.П. Автоматизированный комплекс для исследования свойств магнитожестких материалов. *Приборы и техника эксперимента*. 2002;(1):63–66.

22. Terekhova O.G., Itin V.I., Magaeva A.A., Naiden E.P. Mechanochemical synthesis of nanodimensional ferrite powders from salt systems. *Russian Journal of Non-Ferrous Metals*. 2008;49(4):319–323.
https://doi.org/10.3103/S1067821208040202

Терехова О.Г., Итин В.И., Магаева А.А., Найден Е.П., Иванов Ю.Ф., Максимов Ю.М., Болдырев В.В. Механохимический синтез наноразмерных порошков ферритов из солевых систем. *Известия вузов. Порошковая металлургия и функциональные покрытия*. 2008;(1):45–50.

23. Naiden E.P., Zhuravlev V.A., Itin V.I., Terekhova O.G., Tyukpiekov A.N. Magnetic properties of nanosized hexaferrite powders. *Journal of Structural Chemistry*. 2004;45(1):S106–S110.
https://doi.org/10.1007/s10947-006-0103-4

Найден Е.П., Журавлев В.А., Итин В.И., Терехова О.Г., Тюкпиеков А.Н. Магнитные свойства наноразмерных порошков гексаферрита. *Журнал структурной химии*. 2004;45(7):S106–S111.

Information about the Authors

Anna A. Nevmyvaka – Cand. Sci. (Chem.), Senior Research Scientist, Tomsk Scientific Center, Siberian Branch of the Russian Academy of Sciences.
ORCID: 0000-0003-0716-8685
E-mail: kaa151@mail.ru

Viktor A. Zhuravlev – Cand. Sci. (Phys.-Math.), Assistant Professor of the Department of Radioelectronics, Tomsk State University.
ORCID: 0000-0002-6097-9965
E-mail: ptica@mail.tsu.ru

Volya I. Itin – Cand. Sci. (Phys.-Math.), Leading Researcher, Tomsk Scientific Center, Siberian Branch of the Russian Academy of Sciences.
ORCID: 0009-0002-5248-0360
E-mail: galitina@mail.ru

Сведения об авторах

Анна Алексеевна Невмывака – к.х.н., старший научный сотрудник Томского научного центра Сибирского отделения РАН.
ORCID: 0000-0003-0716-8685
E-mail: kaa151@mail.ru

Виктор Алексеевич Журавлев – к.ф.-м.н., доцент кафедры радиоэлектроники Научно-исследовательского Томского государственного университета.
ORCID: 0000-0002-6097-9965
E-mail: ptica@mail.tsu.ru

Воля Исаевич Итин – к.ф.-м.н., ведущий научный сотрудник Томского научного центра Сибирского отделения РАН.
ORCID: 0009-0002-5248-0360
E-mail: galitina@mail.ru

Contribution of the Authors

A. A. Nevmyvaka – conducted experiments on the mechanochemical synthesis of nanopowders, wrote the manuscript.
V. A. Zhuravlev – conducted *X*-ray phase analysis and investigated the magnetic properties of nanopowders, wrote the manuscript.

V. I. Itin – determined the purpose of the work, participated in the discussion of the results, wrote the manuscript.

Вклад авторов

А. А. Невмывака – проведение экспериментов по механохимическому синтезу нанопорошков, написание текста статьи.
В. А. Журавлев – проведение рентгенофазового анализа и исследование магнитных свойств нанопорошков, подготовка текста статьи.
В. И. Итин – определение цели работы, участие в обсуждении результатов, подготовка текста статьи.

Received 21.10.2022
Revised 21.03.2023
Accepted 23.03.2023

Статья поступила 21.10.2022 г.
Доработана 21.03.2023 г.
Принята к публикации 23.03.2023 г.

Self-Propagating High-Temperature Synthesis
Самораспространяющийся высокотемпературный синтез

UDC 621.762

https://doi.org/10.17073/1997-308X-2023-3-14-21

Research article
Научная статья

Thermal explosions in (Ti, Zr, Hf, Nb, Ta) carbon mixtures

S. G. Vadchenko[1], A. S. Sedegov[2], I. D. Kovalev[1]

[1] **Merzhanov Institute of Structural Macrokinetics and Materials Science of the Russian Academy of Sciences**
8 Akademik Osipyan Str., Chernogolovka, Moscow region 142432, Russia
[2] **National University of Science and Technology "MISIS"**
4 bld. 1 Leninskiy Prosp., Moscow 119049, Russia

vadchenko@ism.ac.ru

Abstract. This research focuses on investigating the ignition and thermal explosion behavior of (Ti, Zr, Hf, Nb, Ta) + 5C mixtures that have been mechanically activated. First, we mechanically activated the metal powder mixtures to produce composite particles consisting of Ti, Zr, Hf, Nb, and Ta, followed by the addition of carbon, and re-activation. An activation time of 120 min at 347 rpm resulted in the formation of solid solutions from the metals in the mixture, while large tantalum particles were preserved. The resulting mixtures were then pressed into pellets, which were heated in argon until ignition occurred. The ignition process involves multiple phases, with the first being inert heating, followed by progressive heating at $t = 420 \div 450$ °C, and a subsequent endothermic phase transformation at 750–770 °C. The temperature then rises rapidly, resulting in a thermal explosion that forms complex carbides, leaving some unreacted tantalum behind. The (Ti, Zr, Hf, Nb, Ta)C_5 activated mixtures and high entropy solid solution are unstable and release titanium and zirconium carbides when heated above 1300 °C, causing changes to the composition of the (Ti, Zr, Hf, Nb, Ta)C_5 final product. When diluted by adding 25 and 50 % of the final product, the effective activation energy E_a for the (Ti, Zr, Hf, Nb, Ta) + 5C reaction in the 1100–1580 °C temperature range was found to be 34 kJ/mol.

Keywords: high-entropy alloys, high-entropy carbides, ceramics, mechanical activation, thermal explosion

For citation: Vadchenko S.G., Sedegov A.S., Kovalev I.D. Thermal explosions in (Ti, Zr, Hf, Nb, Ta) carbon mixtures. *Powder Metallurgy and Functional Coatings*. 2023;17(3):14–21. https://doi.org/10.17073/1997-308X-2023-3-14-21

Тепловой взрыв в смесях (Ti, Zr, Hf, Nb, Ta) с углеродом

С. Г. Вадченко[1], А. С. Седегов[2], И. Д. Ковалев[1]

[1] **Институт структурной макрокинетики и проблем материаловедения им. А.Г. Мержанова РАН**
Россия, 142432, Московская обл., г. Черноголовка, ул. Акад. Осипьяна, 8
[2] **Национальный исследовательский технологический университет «МИСИС»**
Россия, 119049, г. Москва, Ленинский пр-т, 4, стр. 1

vadchenko@ism.ac.ru

Аннотация. В работе исследованы закономерности воспламенения и теплового взрыва механически активированных смесей (Ti, Zr, Hf, Nb, Ta) + 5C. Их готовили в 2 этапа – вначале проводили механическую активацию смесей порошков металлов для получения композитных частиц Ti, Zr, Hf, Nb, Ta, затем добавляли углерод и проводили дополнительную активацию. При активации в течение 120 мин при скорости вращения барабанов 347 об/мин формировались твердые растворы на основе входящих в состав металлов и оставались крупные частицы тантала. Из полученных смесей прессовали таблетки, которые нагревали в атмосфере аргона до воспламенения. Процесс воспламенения включает в себя несколько стадий. На первой стадии происходит инертный нагрев. При $t = 420 \div 450$ °С начинается прогрессивный разогрев образца до температур 750–770 °С, при которых происходит фазовый переход, сопровождающийся эндотермическим эффектом. После фазового перехода температура резко повышается, и происходит тепловой взрыв, в результате чего формируются сложные карбиды и остается непрореагировавший тантал. Активированная смесь и высокоэнтропийный твердый раствор

(Ti, Zr, Hf, Nb, Ta)C_5 нестабильны, и при нагреве выше 1300 °С из них выделяются карбиды. При этом изменяется состав твердого раствора (Ti, Zr, Hf, Nb, Ta)C_5. С использованием последнего для разбавления активированной смеси на 25 % и 50 % для реакции (Ti, Zr, Hf, Nb, Ta) + 5C в интервале температур 1100–1580 °С была определена эффективная энергия активации E_a = 34 кДж/моль.

Ключевые слова: высокоэнтропийные сплавы, высокоэнтропийные карбиды, керамика, механическое активирование, тепловой взрыв

Для цитирования: Вадченко С.Г., Седегов А.С., Ковалев И.Д. Тепловой взрыв в смесях (Ti, Zr, Hf, Nb, Ta) с углеродом. *Известия вузов. Порошковая металлургия и функциональные покрытия*. 2023;17(3):14–21. https://doi.org/10.17073/1997-308X-2023-3-14-21

Introduction

Since 2004, high-entropy alloys (HEA) and high-entropy ceramics based on oxides, borides, carbides, nitrides, and hydrides have been subject of intensive research [1]. Among these materials, high-entropic carbides (HEC) have received particular attention due to their unique features [1–3]. Specifically, Ti, Zr, Hf, Nb and Ta-based HECs form stable monophase compound [4–7] with exceptional mechanical properties [8–11], low thermal conductivity [12], good oxidation resistance [13–15] and biocompatibility [16; 17].

To date, more than 20 manufacturing processes for high-entropy alloys have been developed [1]. Among the most common processes are mechanical activation (MA), spark plasma sintering (SPS), reduction from oxides, and hot pressing. Additionally, self-propagating high-temperature synthesis (SHS) can be utilized to produced HEAs by exploiting the exothermic reactions between group IV–V transition metals and carbon, boron, nitrogen or silicon [18; 19]. The SHS product is typically processed using spark plasma sintering to obtain a single-phase HEC. Although SHS is a rapid and advantageous process, the thermal explosion and combustion of HEC multicomponent mixtures have not been extensively studied.

The aim of this study is to examine the kinetics and product formation during a thermal explosion in (Ti, Zr, Hf, Nb, Ta) + C_5 mixtures.

Materials and methods

We utilized commercially available domestic powders:

– hafnium (Hf), GFM-1 grade (TU 48-4-176-85 Specs), 99.1 % purity, 180 μm average particle size;

– tantalum (Ta), TaP-1 grade (TU 1870-258-00196109-01 Specs), 99.9 % purity, d = 40÷63 μm;

– titanium (Ti), PTM-1 grade (TU 14-22-57-92 Specs), 99.2 % purity, d = 5÷15 μm;

– niobium (Nb), NbP-1a grade (GOST 26252-84), 99.7 % purity, d < 63 μm;

– zirconium (Zr), PCrK-1 grade, (TU 48-4-234-84 Specs), 99.6% purity, d = 40÷63 μm;

– graphite powder, (GOST 23463-79), 99.9999 % purity, ASC 8–4, $d \leq 140$ μm.

Activation and ignition occurred in argon of 99.998 % purity. The powder mixture was prepared in two stages. In the first stage, an equimolar mixture of Ta + Ti + Nb + Zr + Hf was activated in an Activator 2S planetary mill (Activator, Novosibirsk, Russia). The mixture was placed in pre-vacuumed steel drums and subsequently filled with argon at 6 atm. The ball-to-powder weight ratio was 1:18, with a ball weight of 360 g (5–7 mm diameter) and powder weight of 20 g. The drum rpm was 347 and the milling time was 120 min, resulting in the production of a metallic composite.

To prevent oxidation and self-ignition, the composite powder was unloaded in an argon-filled glove box. Graphite powder was added to the mixture inside the glove box to create (Ti, Zr, Hf, Nb, Ta)C_5. The resulting mixture was similarly activated for 60 min and then passivated. The drum was open for 1–2 s to allow air in, then closed and held for 10–12 h. To obtain a homogeneous mixture with the (Ti, Zr, Hf, Nb, Ta)C_5 high-entropy alloy made by SHS, a portion of the composite/graphite powder was stirred in a porcelain mortar for 30 min. The final product concentrations in these mixtures were 25 and 50 %. Samples, measuring 3 mm in diameter and up to 1.0–1.5 mm in height, were pressed from the mixtures.

The procedure for the ignition temperature test is depicted in Figure 1 [20]. The cylindrical samples were positiond on a flat thermocouple that was 30 μm thick, and then placed into either a boron nitride or graphite crucible. The crucible was subsequently placed on an electric graphite strip heater and heated to the ignition or melting temperature. The accuracy of temperature measurement was validated using the Zn, Al and Cu melting points as a reference. The margin of error at $t \leq 1100$ °C was no more than ±10 °C. The thermocouple readings were recorded at 1 kHz.

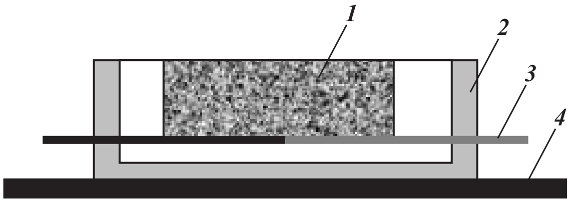

Fig. 1. Sample ignition temperature measurements
1 – sample, ***2*** – crucible, ***3*** – thermocouple, ***4*** – graphite strip heater

Рис. 1. Схема измерения температуры воспламенения образцов
1 – образец, ***2*** – тигель, ***3*** – термопара, ***4*** – графитовый ленточный нагреватель

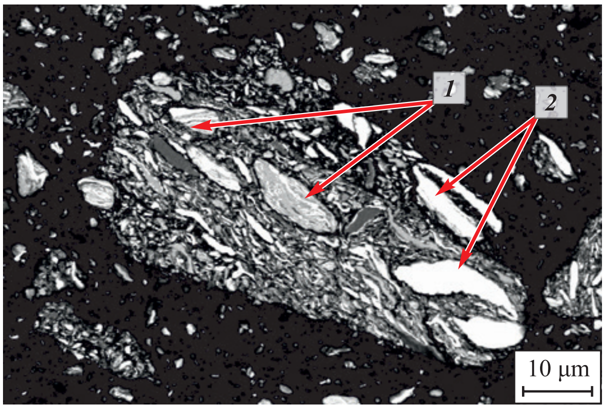

Fig. 2. Microstructure of a (Ti, Zr, Hf, Nb, Ta) mixture particle after activation and passivation
1 – layered inclusions, ***2*** – tantalum particles

Рис. 2. Микроструктура частицы смеси (Ti, Zr, Hf, Nb, Ta) после активации и пассивации
1 – слоистые включения, ***2*** – частицы тантала

For XRD of the initial samples and products after ignition, we employed a DROn 3M diffractometer with CuK_α-radiation (Burevestnik, St. Petersburg, Russia). Furthermore, we used an LEO 1450 VP microscope (Carl Zeiss, Germany) for canning electron microscopy (SEM).

Results and discussion

Figure 2 depicts the thin section microstructure of the initial Ti, Zr, Hf, Nb, and Ta composite particles. It was not possible to produce homogeneous composite particles from the metal powder mixture, as the particles contained both layered inclusions (*1*) and individual large tantalum particles (*2*).

Due to insufficient probe positioning accuracy, it was not possible to analyze smaller particles and layers. However, the SEM analysis indicated that they included all of the original elements. XRD analysis (Figure 3) indicated that the metal peaks had shifted to the left, indicating the formation of solid solutions. The tantalum and niobium peaks were nearly identical. The small peak located at approximately 40° was close to the 100 % titanium peak. Ti was found to form solid solutions with tantalum, niobium, hafnium and zirconium.

The formation of solid solutions was confirmed by the plateau observed in the thermal curves at various heating rates (V) during the initial stage ($t < 450$ °C), as shown in Figure 4. A thermal curve of the heating of the titanium sample was also included for comparison.

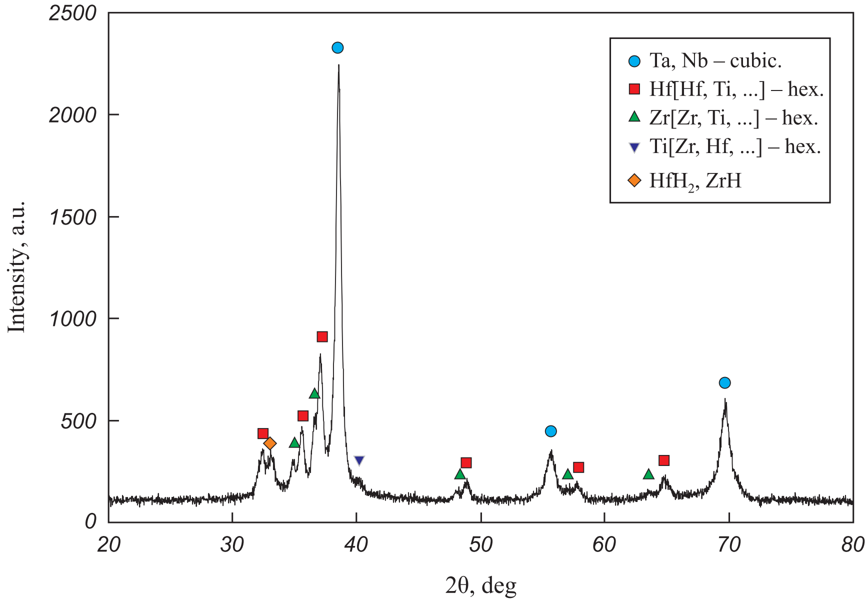

Fig. 3. XRD image of the (Ti, Zr, Hf, Nb, Ta) + 5C mixture after activation and passivation

Рис. 3. Рентгенограмма смеси (Ti, Zr, Hf, Nb, Ta) + 5C после процессов активации и пассивации

The ignition temperature (t_{ig}) at high heating rates is 1030 °C. The temperature decreases with the heating rate down to 760 °C. The thermal curves suggest that this decrease is due to a phase transformation with a significant endothermic effect, resulting in an isothermal segment in thermal curves. The α–β-transformation temperatures for titanium, zirconium, and hafnium in the Group IV metals in the mixture are $t_{\alpha-\beta}$ = 882, 865 and 1743 °C, respectively. These temperatures are considerabely higher than those indicated on the thermal curves. It should be noted that the formation of solid solutions during mechanical activation can lead to a decrease in the α–β-transformation temperature in titanium. Okamoto H. and Lyakishev N.P. [21; 22] reported that $t_{\alpha-\beta}$ for titanium-zirconium equiatomic solid solutions can drop to 560–600 °C. Polymorphic transformations in Ti–Nb metastable solid solutions can occur at t = 425÷600 °C [23].

Polymorphic transformation generally enhances diffusion coefficients. This, in turn, accelerates the reaction between the solid solutions and carbon and $t_{\alpha-\beta}$ become the critical temperature of thermal explosion (t_c). The sample heating rates at the initial stage (V_1) and after ignition (V_2) were recorded as follows:

t_c, °C	760	760	770	790	830	1000
V_1, °C/s	45	47	53	68	95	240
V_2, °C/s	4250	5400	9400	11,300	8700	6500

It can be seen that the heating rate of the V_2 sample above the critical temperature is two orders of magnitude greater than the V_1 average heating rate at the initial heating stage (up to 450 °C), indicating a thermal explosion.

Figure 5 displays the XRD image of the thermal explosion products of the activated (Ti, Zr, Hf, Nb, Ta) + 5C mixture. The ignition is triggered by the formation of carbides or solid solutions of carbon in the metals, but it does not lead to the formation of the final product. Due to the short holding time at high temperatures and rapid cooling, some of the metals do not have sufficient time to react. Comparing the XRD images in Figure 3 and 5, it can be observed that the peak intensity ratio changes after the thermal explosion due to the formation of hafnium and niobium carbides.

To investigate the reaction kinetics in this system, we diluted the initial mixture with the (Ta, Ti, Nb, Zr, Hf)C_5 final product obtained by SHS. Figure 6 illustrates the thermal curves for the samples containing 25 and 50 % of the final product.

Figure 7 shows the XRD images of the products obtained by adding 25 and 50 % of the final product to the (Ti, Zr, Hf, Nb, Ta) + 5C activated mixture, and the XRD image of the final product.

The XRD images of the products obtained by heating the diluted mixture are nearly identical. The main phase formed by dilution retains its cubic lattice, but the lattice parameters differ. The XRD images reveal peaks of titanium and zirconium carbide. The XRD images of the activated mixture (see Figure 3) exhibit weakly pronounced titanium and zirconium peaks. When heated

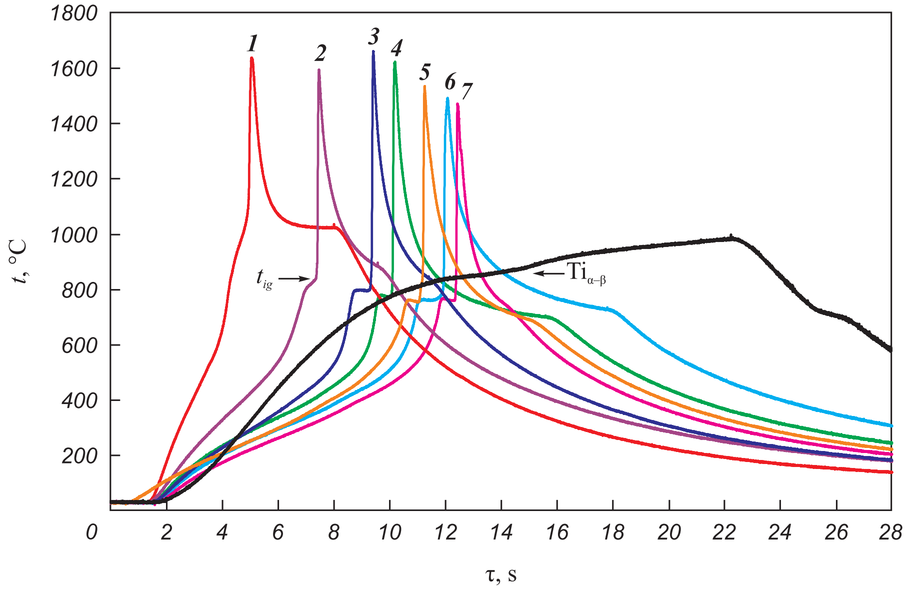

Fig. 4. Thermal curves for various heating rates of the (Ti, Zr. Hf, Nb, Ta) + 5C mixture and titanium samples
V, °C/s: 240 (***1***), 95 (***2***), 72 (***3***), 68 (***4***), 53 (***5***), 47 (***6***) and 45 (***7***)

Рис. 4. Термограммы при различных скоростях нагрева образцов из смеси (Ti, Zr. Hf, Nb, Ta) + 5C и образца из титана
V, °C/c: 240 (***1***), 95 (***2***), 72 (***3***), 68 (***4***), 53 (***5***), 47 (***6***) и 45 (***7***)

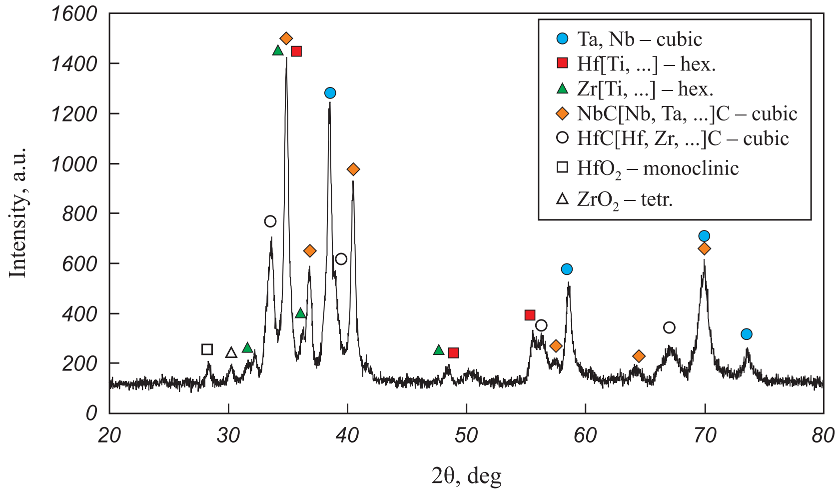

Fig. 5. XRD image of the thermal explosion products of the activated (Ti, Zr, Hf, Nb, Ta) + 5C mixture

Рис. 5. Рентгенограмма продуктов теплового взрыва активированной смеси (Ti, Zr, Hf, Nb, Ta) + 5C

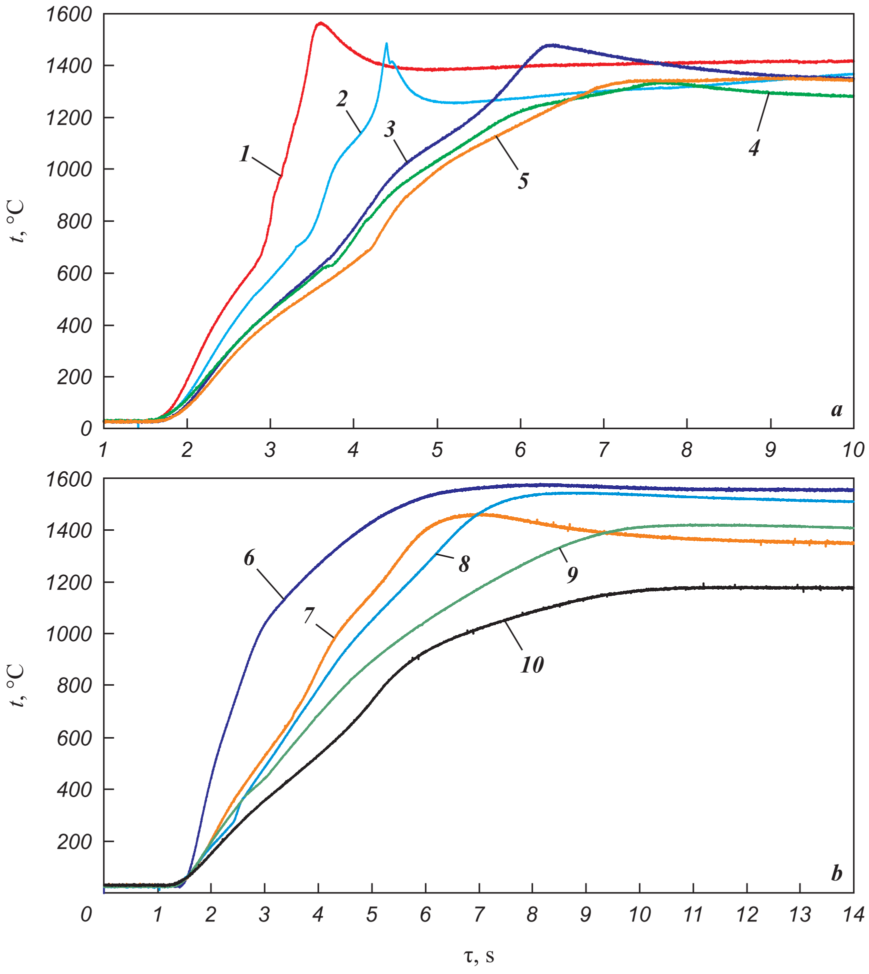

Fig. 6. Thermal curves for various heating rates of the (Ti, Zr, Hf, Nb, Ta) + 5C mixtures containing 25 (***a***) and 50 % (***b***) of the (Ti, Zr, Hf, Nb, Ta)C_5 final product
a – V = 550 °C/s (***1***), 480 (***2***), 310 (***3***), 280 (***4***) and 140 (***5***)
b – V = 730 °C/s (***6***), 340 (***7***), 310 (***8***), 295 (***9***) and 190 (***10***)

Рис. 6. Термограммы при различных скоростях нагрева образцов из смесей (Ti, Zr, Hf, Nb, Ta) + 5C, содержащих 25 (***a***) и 50 % (***b***) конечного продукта (Ti, Zr, Hf, Nb, Ta)C_5
a – V = 550 °C/c (***1***), 480 (***2***), 310 (***3***), 280 (***4***) и 140 (***5***)
b – V = 730 °C/c (***6***), 340 (***7***), 310 (***8***), 295 (***9***) и 190 (***10***)

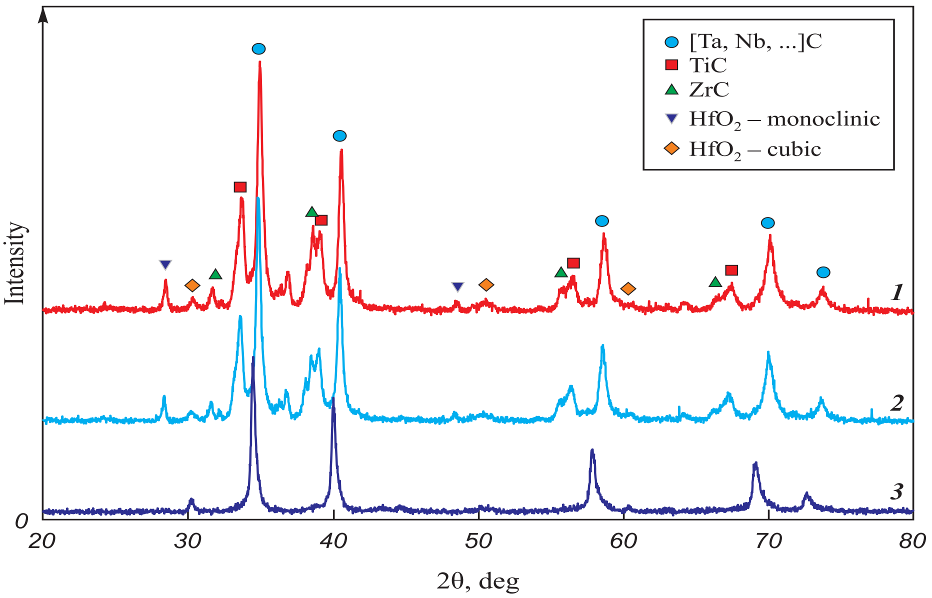

Fig. 7. XRD images of the products obtained by heating the activated (Ti, Zr, Hf, Nb, Ta) + 5C mixture diluted by 25 % (***1***) and 50 % (***2***) of the (Ti, Zr, Hf, Nb, Ta)C_5 final product (***3***)

Рис. 7. Рентгенограммы продуктов нагрева активированной смеси (Ti, Zr, Hf, Nb, Ta) + 5C, разбавленной на 25 % (***1***) и 50 % (***2***), и конечного продукта (Ti, Zr, Hf, Nb, Ta)C_5 (***3***)

above 1300 °C, the peaks of Ti and Zr carbide become visible. We can conclude that the solid solutions formed after activation and the dilution of high-entropy phase are unstable at high temperatures ($t > 1300$ °C), resulting in the release of titanium and zirconium carbides. The composition of the (Ti, Zr, Hf, Nb, Ta)C_5 high-entropy phase also changes.

Since the compositions of the ignition products of the diluted mixture are nearly identical, we used the max temperature vs. heating rate curves for the two dilutions to estimate the activation energy using the Kissinger equation. The reaction rate in the diluted mixtures decreased significantly, and the sample overheating was low. Furthermore, the temperature gradient across the relatively thin samples (about 1 mm thick) was insignificant. Considering these factors, we estimated the activation energy for the reaction forming the (Ti, Zr, Hf, Nb, Ta)C_5 high-entropic phase as follows:

$$\ln\left(\frac{\beta}{T_{\max}^{2}}\right) = \ln\left(\frac{AR}{E_{a}}\right) - \frac{E_{a}}{RT_{\max}},$$

where β is the heating rate, degrees/s; E_a is the activation energy, kJ/mol; $R = 8.314$ J/(mol·K) is the gas constant; A is the pre-exponential factor of the Arrhenius equation (particle collision frequency, s^{-1}); $T_{\max}$ is the max temperature, K.

Figure 8 shows the $\ln\left(\frac{\beta}{T_{\max}^{2}}\right)$ vs. $T_{\max}^{-1}$ curve.

The activation energy E_a for the reaction of the (Ti, Zr, Hf, Nb, Ta) + 5C activated mixtures diluted with the final product in the temperature range of 1100–1580 °C, was found to be 34 kJ/mol. This value is significantly lower, by 75–80 %, than the value estimated from previous experimental data on gasless combustion of metal-carbon systems [24]. One possible explanation for this discrepancy is that the mechanical activation process resulted in an increase in the reactivity of the metals, which may be attributed to the grinding

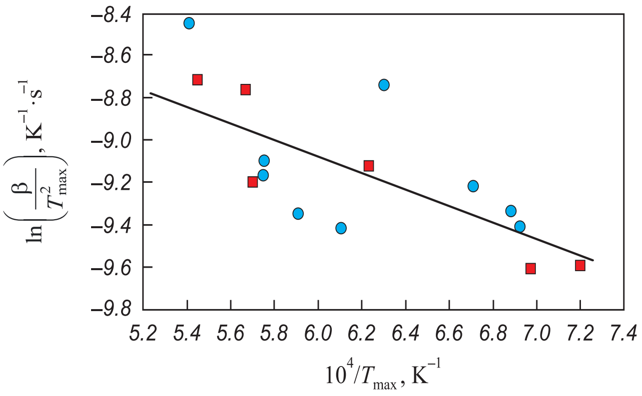

Fig. 8. The reaction activation energy estimated with Kissinger's equation
The activated mixtures (Ti, Zr, Hf, Nb, Ta) + 5C are diluted by adding 25 % (■) and 50 % (●) of the final product

Рис. 8. Результаты оценки энергии активации реакции по уравнению Киссинджера
Разбавление конечным продуктом активированных смесей (Ti, Zr, Hf, Nb, Ta) + 5C на 25 % (■) и 50 % (●)

process, the closer contacts between reactants and the introduction of more crystal lattice defects.

Conclusions

1. The mechanical activation of (Ti, Zr, Hf, Nb, Ta) + 5C mixtures for 120 min at 347 rpm produces composite particles and solid solutions of Ti, Zr, Hf, Nb and Ta, while individual tantalum particles remain in the mixture.

2. The ignition of the (Ti, Zr, Hf, Nb, Ta) + 5C activated mixture occurs in several stages, including inert heating, progressive heating to 420–450 °C and phase transformation at 750–770 °C. A thermal explosion occurs when the temperature raises abruptly.

3. Despite the high temperatures, the reaction produces complex carbides, and unreacted tantalum remains due to the short duration of the thermal explosion.

4. The activated mixtures and high entropy solid solution are unstable. When heated above 1300 °C, they release titanium and zirconium carbides. This process also causes a change in the composition of the (Ti, Zr, Hf, Nb, Ta)C_5 final product.

5. The effective activation energy estimated for the reaction in the (Ti, Zr, Hf, Nb, Ta) + 5C mixture (E_a = 34 kJ/mol) is 75–80 % lower than the values reported for the metal + carbon combustion reactions. This could be attributed to the mechanical activation of the mixture.

References / Список литературы

1. Akrami S., Edalati P., Fuji M., Edalati K. High-entropy ceramics: Review of principles, production and applications. *Materials Science and Engineering: R: Reports*. 2021;146:100644. https://doi.org/10.1016/j.mser.2021.100644
2. Ye B., Wen T., Huang K., Wang C.Z., Chu Y. First-principles study, fabrication, and characterization of $(Hf_{0.2}Zr_{0.2}Ta_{0.2}Nb_{0.2}Ti_{0.2})C$ high-entropy ceramic. *Journal of the American Ceramic Society*. 2019;102(7):4344–4352. https://doi.org/10.1111/jace.16295
3. Zhang Q., Zhang J., Li N., Chen W. Understanding the electronic structure, mechanical properties, and thermodynamic stability of (TiZrHfNbTa)C combined experiments and first-principles simulation. *Journal of Applied Physics*. 2019;126(2):025101. https://doi.org/10.1063/1.5094580
4. Kochetov N.A., Kovalev I.D. Synthesis and thermal stability of the multielement carbide (TaZrHfNbTi)C_5. *Inorganic Materials*. 2021:57(1):8–13. https://doi.org/10.1134/S0020168520120109
5. Kovalev D.Yu., Kochetov N.A., Chuev I.I. Fabrication of high-entropy carbide (TiZrHfTaNb)C by high-energy ball milling. *Ceramics International*. 2021;47(23):32626–32633. https://doi.org/10.1016/j.ceramint.2021.08.158
6. Sarker P., Harrington T.J., Gild J., Sarker P., Toher C., Rost C.M., Dippo O.F., McElfresh C., Kaufmann K., Marin E., Borowski L., Hopkins P.E., Luo J., Curtarolo S., Brenner D.W., Vecchio K.S. Phase stability and mechanical properties of novel high entropy transition metal carbides. *Acta Materialia*. 2019;166:271–280. https://doi.org/10.1016/j.actamat.2018.12.054
7. Sarker P., Harrington T.J., Toher C., Oses C., Samiee M., Maria J.P., Brenner D.W., Vecchio K.S., Curtarolo S. High-entropy high-hardness metal carbides discovered by entropy descriptors. *Nature Communications*. 2018;9:4980. https://doi.org/10.1038/s41467-018-07160-7
8. Jiang S., Shao L., Fan T., Duan J.M., Chen X.T., Tang B.Y. Mechanical behavior of high entropy carbide (HfTaZrTi)C and (HfTaZrNb)C under high pressure: Ab initio study. *International Journal of Quantum Chemistry*. 2020;121(5):1–11. https://doi.org/10.1002/qua.26509
9. Moskovskikh D.O., Vorotilo S., Sedegov A.S., Kuskov K.V., Bardasova K.V., Kiryukhantsev-Korneev Ph.V., Zhukovskyi M., Mukasyan A.S. High-entropy (HfTaTiNbZr)C and (HfTaTiNbMo)C carbides fabricated through reactive high-energy ball milling and spark plasma sintering. *Ceramics International*. 2020;46(11B):19008–19014. https://doi.org/10.1016/j.ceramint.2020.04.230
10. Wang F., Zhang X., Yan X., Lu Y., Nastasi M., Chen Y., Cui B. The effect of submicron grain size on thermal stability and mechanical properties of high-entropy carbide ceramics. *Journal of the American Ceramic Society*. 2020;103(8):4463–4472. https://doi.org/10.1111/jace.17103
11. Feng L., Fahrenholtz W.G., Hilmas G.E. Low-temperature sintering of single-phase, high-entropy carbide ceramics. *Journal of the American Ceramic Society*. 2019;102(12):7217–7224. https://doi.org/10.1111/jace.16672
12. Chen H., Xiang H., Dai F.Z., Liu J., Lei Y., Zhang J., Zhou Y. High porosity and low thermal conductivity high entropy $(Zr_{0.2}Hf_{0.2}Ti_{0.2}Nb_{0.2}Ta_{0.2})C$. *Journal of Materials Science & Technology*. 2019;35(8):1700–1705. https://doi.org/10.1016/j.jmst.2019.04.006
13. Ye B., Wen T., Liu D., Chu Y. Oxidation behavior of $(Hf_{0.2}Zr_{0.2}Ta_{0.2}Nb_{0.2}Ti_{0.2})C$ high-entropy ceramics at 1073–1473 K in air. *Corrosion Science*. 2019;153:327–332. https://doi.org/10.1016/j.corsci.2019.04.001
14. Ye B., Wen T., Chu Y. High-temperature oxidation behavior of $Hf_{0.2}Zr_{0.2}Ta_{0.2}Nb_{0.2}Ti_{0.2})C$ high-entropy ceramics in air. *Journal of the American Ceramic Society*. 2020;103(1):500–507. https://doi.org/10.1111/jace.16725
15. Wang H., Cao Y., Liu W., Wang Y. Oxidation behavior of $(Hf_{0.2}Ta_{0.2}Zr_{0.2}Ti_{0.2}Nb_{0.2})$C-xSiC ceramics at high temperature. *Ceramics International*. 2020;46(8A):11160–11168. https://doi.org/10.1016/j.ceramint.2020.01.137
16. Braic V., Vladescu A., Balaceanu M., Luculescu C.R., Braic M. Nanostructured multi-element (TiZrNbHfTa)N and (TiZrNbHfTa)C hard coatings. *Surface and Coatings Technology*. 2012;211:117–121. https://doi.org/10.1016/j.surfcoat.2011.09.033
17. Braic V., Balaceanu M., Braic M., Vladescu A., Panseri S., Russo A. Characterization of multiprincipal-element (TiZrNbHfTa)N and (TiZrNbHfTa)C coatings for biomedical applications. *Journal of the Mechanical Be-

havior of Biomedical Materials. 2012;10:197–205. https://doi.org/10.1016/j.jmbbm.2012.02.020

18. Merzhanov A.G., Borovinskaya I.P. Self-propagated high-temperature synthesis of refractory inorganic compounds. *Doklady Chemistry Proceedings of the Academy of Sciences of the USSR. Chemistry Section*. 1972;204(2):429–433.

19. Tallarita G., Licheri R., Garroni S., Orrù R., Cao G. Novel processing route for the fabrication of bulk high-entropy metal diborides. *Scripta Materialia*. 2019;158:100–104. https://doi.org/10.1016/j.scriptamat.2018.08.039

20. Vadchenko S.G., Boyarchenko O.D., Shkodich N.F., Rogachev A.S. Thermal explosion in various Ni–Al systems: Effect of mechanical activation. *International Journal of Self-Propagating High-Temperature Synthesis*. 2013;22(1):60–64. https://doi.org/10.3103/S1061386213010123

21. Okamoto H. Desk handbook: Phase diagrams for binary alloys. 2nd Ed. Edited by ASM International Materials Park. Ohio, USA. 2010. 855 p.

22. Lyakishev N.P. (Ed.) Dual metal system state diagrams: Reference book. In 3 volumes. Vol. 1. Moscow: Mashinostroenie, 1996. 992 p. (In Russ.).

Диаграммы состояния двойных металлических систем: Справочник. В 3 т. Т. 1. Под общ. ред. Н.П. Лякишева. М.: Машиностроение, 1996. 992 с.

23. Zhang Y., Liu H., Jin Z. Thermodynamic assessment of the Nb–Ti system. *Calphad*. 2001;25(2):305–317. https://doi.org/10.1016/S0364-5916(01)00051-7

24. Mukasyan A.S., Rogachev A.S. Discrete reaction waves: Gasless combustion of solid powder mixtures. *Progress in Energy and Combustion Science*. 2008;34(3):377–416. https://doi.org/10.1016/j.pecs.2007.09.002

25. Egorychev K.N., Kurbatkina V.V., Levashov E.A. Prospects for the use of mechanical activation of low-exothermal materials for synthesis of composite materials by SHS technology. *Izvestiya vuzov. Tsvetnaya metallurgiya*. 1996;(6):49–52. (In Russ.).

Егорычев К.Н., Курбаткина В.В., Левашов Е.А. Перспективы применения механического активирования низкоэкзотермических материалов для синтеза композиционных материалов СВС-технологией. *Известия вузов. Цветная металлургия*. 1996;(6):49–52.

26. Korchagin M.A. Thermal explosion in mechanically activated low-calorie compositions. *Fizika goreniya i vzryva*. 2015;51(5):77–86. (In Russ.). http://dx.doi.org/10.15372/FGV20150509

Корчагин М.А. Тепловой взрыв в механически активированных низкокалорийных составах. *Физика горения и взрыва*. 2015;51(5):77–86. http://dx.doi.org/10.15372/FGV20150509

Information about the Authors

Sergey G. Vadchenko – Cand. Sci. (Phys.-Math.), Leading Researcher, Microheterogenic Process Dynamics Laboratory, Merzhanov Institute of Structural Macrokinetics and Materials Science, Russian Academy of Sciences.
ORCID: 0000-0002-2360-2114
E-mail: vadchenko@ism.ac.ru

Aleksei S. Sedegov – Engineer, Structural Nanoceramics Research Center, National University of Science and Technology “MISIS”
ORCID: 0000-0002-4927-8930
E-mail: a.sedegov@misis.ru

Ivan D. Kovalev – Cand. Sci. (Phys.-Math.), Senior Researcher, *X*-Ray Structural Research Laboratory, Merzhanov Institute of Structural Macrokinetics and Materials Science, Russian Academy of Sciences.
ORCID: 0000-0003-4710-837X
E-mail: i2212@yandex.ru

Сведения об авторах

Сергей Георгиевич Вадченко – к.ф.-м.н., вед. науч. сотрудник лаборатории динамики микрогетерогенных процессов, Институт структурной макрокинетики и проблем материаловедения им. А.Г. Мержанова Российской академии наук (ИСМАН).
ORCID: 0000-0002-2360-2114
E-mail: vadchenko@ism.ac.ru

Алексей Сергеевич Седегов – инженер НИЦ «Конструкционные керамические наноматериалы», Национальный исследовательский технологический университет «МИСИС».
ORCID: 0000-0002-4927-8930
E-mail: a.sedegov@misis.ru

Иван Дмитриевич Ковалев – к.ф.-м.н., ст. науч. сотрудник лаборатории рентгеноструктурных исследований, ИСМАН.
ORCID: 0000-0003-4710-837X
E-mail: i2212@yandex.ru

Contribution of the Authors

S. G. Vadchenko – problem statement, tests, text authoring.

A. S. Sedegov – mixture and sample preparation, discussion.

I. D. Kovalev – XRD analysis, discussion.

Вклад авторов

С. Г. Вадченко – определение целей работы, проведение экспериментов, написание текста статьи.

А. С. Седегов – подготовка смесей и исходных образцов, участие в обсуждении результатов.

И. Д. Ковалев – проведение рентгенофазового анализа, участие в обсуждении результатов.

Received 22.06.2022
Revised 11.11.2022
Accepted 19.12.2022

Статья поступила 22.06.2022 г.
Доработана 11.11.2022 г.
Принята к публикации 19.12.2022 г.

Refractory, Ceramic and Composite Materials
Тугоплавкие, керамические и композиционные материалы

UDC 621.762

https://doi.org/10.17073/1997-308X-2023-3-22-29

Research article
Научная статья

Influence of thermomechanical treatment on the formation of the structure in dispersed-reinforced aluminum alloy-based metal composite materials

A. N. Nyafkin ✉, D. V. Kosolapov, E. I. Kurbatkina

All-Russian Scientific Research Institute of Aviation Materials of the National Research Center “Kurchatov Institute”
25A Budyonny Prosp., Moscow 105275, Russia

✉ andrey.viam@mail.ru

Abstract. The study explored various facets of the structure of dispersed-reinforced aluminum alloy-based metal composite material (MCM) under different modes of thermomechanical treatment. Replacing traditional structural materials with MCM provides manufacturers with an opportunity to achieve higher levels of engineering superiority. The ability to choose composition, modify primary component ratios, and employ a range of MCM manufacturing techniques allows for precise tuning of the material's strength, rigidity, temperature range, and other physical and mechanical properties. Two prevalent technologies for crafting dispersed-reinforced aluminum alloy-based MCM exist: liquid-phase and powder technologies. Liquid-phase methodology entails merging the reinforcing component into the binder alloy's melt, followed by crystallization. This process guarantees the dispersion and fixation of reinforcing particles within the binder volume. In contrast, powder technology involves simultaneous processing of primary component powders in high-energy mills, with subsequent amalgamation of the resultant composite granules via pressure molding. The chief aim of thermomechanical treatment lies in yielding blanks that closely mimic the final product's geometry and reshaping the deformable material's structure to heighten its strength properties. Powder technology was employed to fabricate monolithic composite material samples. Their structures were analyzed, accompanied by tests to ascertain density and strength parameters of the MCM at room temperature. Consequently, dispersed-reinforced aluminum alloy-based MCM possessing a uniform structure, density exceeding 99.0 % of the theoretical value, and elevated mechanical attributes: $\sigma_u = 300 \div 305$ MPa and $E = 87 \div 95$ GPa, were successfully produced.

Keywords: metal composite material (MCM), aluminum alloy, thermomechanical treatment, pressing, structure, strength properties

For citation: Nyafkin A.N., Kosolapov D.V., Kurbatkina E.I. Influence of thermomechanical treatment on the formation of the structure in dispersed-reinforced aluminum alloy-based metal composite materials. *Powder Metallurgy and Functional Coatings*. 2023;17(3):22–29. https://doi.org/10.17073/1997-308X-2023-3-22-29

Влияние деформационно-термической обработки на формирование структуры дисперсно-армированного металлического композиционного материала на основе алюминиевого сплава

А. Н. Няфкин ✉, Д. В. Косолапов, Е. И. Курбаткина

Всероссийский научно-исследовательский институт авиационных материалов
Национального исследовательского центра «Курчатовский институт»
Россия, 105275, г. Москва, пр-т Буденного, 25А

✉ andrey.viam@mail.ru

Аннотация. Исследованы аспекты формирования структуры дисперсно-армированного металлического композиционного материала (МКМ) на основе алюминиевого сплава в зависимости от различных режимов деформационно-термической обработки. Замена традиционных конструкционных материалов на МКМ позволит производителям перейти на качественно более высокий технический уровень. Подбор состава, изменение соотношения исходных компонентов и применение различных методов изготовления МКМ позволяют направленно регулировать прочность, жесткость, диапазон рабочих температур и другие физико-механические характеристики материала. Существуют две наиболее распространенные технологии получения дисперсно-армированных МКМ на основе алюминиевых сплавов – жидкофазная и порошковая. Первая предполагает размешивание армирующего компонента в расплаве матричного сплава с последующей кристаллизацией, которая обеспечивает распределение и фиксацию армирующих частиц в объеме матрицы, а вторая представляет собой совместную обработку порошков исходных компонентов в высокоэнергетических мельницах с последующим объединением полученных композиционных гранул методами обработки давлением. Основной целью деформационно-термической обработки является получение заготовок с формой, максимально приближенной к геометрии конечных изделий, а также изменение структуры деформируемого материала, приводящее к повышению уровня прочностных свойств. В работе с использованием порошковой технологии были изготовлены образцы монолитного композиционного материала, исследована их структура и проведены испытания с целью определения плотности и прочностных характеристик МКМ при комнатной температуре. В результате получены дисперсно-армированные МКМ на основе алюминиевого сплава с однородной структурой, плотностью более 99,0 % от теоретической и повышенными механическими свойствами: $\sigma_в$ = 300÷305 МПа и E = 87÷95 ГПа.

Ключевые слова: металлический композиционный материал (МКМ), алюминиевый сплав, деформационно-термическая обработка, прессование, структура, прочностные характеристики

Для цитирования: Няфкин А.Н., Косолапов Д.В., Курбаткина Е.И. Влияние деформационно-термической обработки на формирование структуры дисперсно-армированного металлического композиционного материала на основе алюминиевого сплава. *Известия вузов. Порошковая металлургия и функциональные покрытия*. 2023;17(3):22–29. https://doi.org/10.17073/1997-308X-2023-3-22-29

Introduction

Currently, the creation of promising products in aviation and rocket-space engineering demands materials with low density and enhanced strength properties for primary structures. Such materials, owing to their distinct properties, can also find utility in ultralight, high-load structures across various industries [1; 2].

Moreover, a critical concern for contemporary material developers revolves around devising energy-efficient production technologies that lead to reduced product costs, heightened material utilization coefficients in end products, and enhanced product competitiveness [3–5].

A prospective avenue for addressing the aforementioned challenges lies in the utilization of metal composite materials (MCM) based on dispersed-reinforced aluminum alloys, coupled with the refinement of techniques for manufacturing components from these materials to ensure the requisite levels of physical, mechanical, and operational parameters in the resultant products [5–10].

Typically, metal composite materials comprise a plastic metal alloy fortified with solid ceramic reinforcement materials in the form of particles characterized by varied sizes and shapes [11–13].

The production of MCM through powder technology entails the concurrent processing of primary component powders within high-energy mills, followed by the consolidation of the resultant composite granules through pressure molding. The fundamental goal of thermomechanical treatment is to yield blanks that closely approximate the final product's geometry, while also inducing structural modifications in the deformable material to enhance its strength properties. The thermomechanical treatment procedure hinges upon the inherent capacity of plastic materials to undergo irreversible shape changes when subjected to external forces, all without succumbing to destruction [14].

The structure of dispersed-reinforced MCM comprises a binder metal wherein finely dispersed particles of the reinforcing phase are uniformly distributed. The binder metal within the MCM imparts plasticity, while the ceramic phase enhances strength, rigidity, thermal resistance and wear resistance. The mechanism underpinning MCM reinforcement is preconditioned by the formation by the strengthening phase particles of barriers for dislocation movement, similar to the mechanism in alloys with dispersion hardening. Opting for aluminum alloys as a binder metal in MCM is favored due to their superiority over alternative alloys, encompassing excellent workability, performance, and cost-effectiveness [15; 16].

The objective of this study was to investigate the impact of thermomechanical treatment on the structure of MCM based on an aluminum alloy from the Al–Mg–Si system, reinforced with 20 vol. % SiC and produced via powder technology.

Research methodology

The primary material used for manufacturing dispersed-reinforced aluminum alloy-based MCM consisted of composite granules obtained through mechanical alloying in a laboratory planetary ball mill model PM 100 (SM Retsch, England).

AD31 aluminum alloy was employed as the binder, while the reinforcing phase consisted of 63C (F800) silicon carbide particles.

The composite granules were compressed within a blind die to produce blanks in the shape of cylindrical briquettes. Subsequently, these briquettes were heated to the hot deformation temperature and then pressed using a k03.032 hydraulic press (Russia).

The necessary pressing force for MCM through a cone die via direct pressing was determined using the following formula:

$$P = \sigma_{0.2}\left[\left(\frac{1}{2\sin\alpha}\right) + \left(\frac{2}{1+\cos\alpha}\right)\ln\frac{F}{f} + \frac{2L}{D} + \frac{2l}{d}\right]F,$$

where $\sigma_{0.2}$ is the yield strength of MCM at the pressing temperature, MPa; α is the angle of inclination of the die generatix, deg; F and f are the projection areas of the briquette and the pressed bar on the plane perpendicular to the direction of the male's die movement, respectively, mm^2; L is the height of the briquette, mm; l is the height of the die bearing, mm.

The structure of the pressed MCM samples was examined using an optical electron microscope Olympus BX51 (Olympus, Japan).

The density of the MCM samples was determined through hydrostatic weighing.

The porosity of the material was calculated using the following formula:

$$n = \left(1 - \frac{\rho_{\text{fact}}}{\rho_{\text{calc}}}\right)\cdot 100\ \%,$$

where ρ_{fact} and ρ_{calc} are the measured and calculated values of MCM density, respectively, g/cm^3.

The strength characteristics of the MCM were assessed through uniaxial tension conducted in accordance with GOST 1497-84 using a Zwick Roell testing machine (Zwick Roell Group, Germany).

Results of the study and their discussion

The morphology of the initial material, which consists of mechanically alloyed composite granules, is presented in Figure 1. The majority of these granules exhibit a spherical shape with a textured surface. The particle size distribution of the granules predominantly falls within the range of 600 to 1000 μm.

Cylindrical briquettes were manufactured from the composite granules using a blind die pressing technique on a hydraulic press, with the intention of subsequently undergoing hot direct pressing via a cone die.

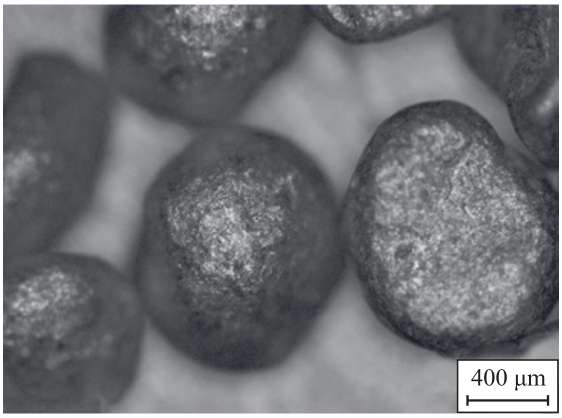

Fig. 1. Structure of mechanically alloyed aluminum alloy-based MCM granules

Рис. 1. Структура механически легированных гранул МКМ на основе алюминиевого сплава

The compaction of granules through blind die pressing unfolds in multiple stages. During the initial phase, the pressing tool induces mutual shifts among the granules, consequently reducing the available interstitial space. This, in turn, leads to the deceleration of their mobility due to mounting friction emerging at the points of contact between the granules. The ensuing stage is marked by the escalation of contact stresses and the commencement of deformation processes. Once the stress level matches the yield strength of the composite material, plastic deformation pervades the entirety of the briquette's volume. Consequently, an intensive alteration in the shape and condition of the granule contact surfaces transpires. This culminates in the formation of a compacted structure within the composite material, characterized by a porosity ranging from 5 to 10 %.

In [17–19], investigations were conducted into the impact of specific pressing pressures on the density of briquettes crafted from powdered materials. It was demonstrated that upon reaching a density threshold of 90–95 % of the theoretical density, the compaction process slows down, leading to no further density augmentation despite increased pressing force.

The graph illustrating the correlation between density and pressing force, as observed in the experiments carried out in the context of this study, is depicted in Figure 2. In this diagram, zone *1* corresponds to the initial phase of the blind die pressing process, while zone *2* pertains to the subsequent stage.

The deceleration of material compaction can be elucidated through the specific nature of deformation processing within the confined space of the blind die. This is attributed to both the restricted ability for pressed MCM volume redistribution within the confined dimensions of the blind die and the limited extent of deformation experienced by the material under the comprehensive compressive force.

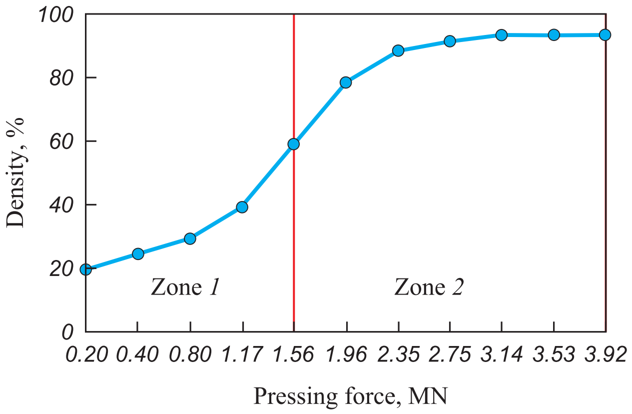

Fig. 2. Dependence of MCM density on the pressing force

Рис. 2. Зависимость плотности МКМ от усилия прессования

The distribution of accumulated deformation fields, acquired from modeling the pressing procedure within a blind die, is illustrated in Figure 3. Notably, the central region of the briquette displays the most pronounced structural refinement. Conversely, the upper and lower portions of the briquette, which were in contact with the male die and the bottom of the blind die, exhibit a comparatively lower level of accumulated deformation, ranging from 0.1 to 0.3. The emergence of frictional forces at the contact surface between the male die and the blind die's base curtails the motion of the compressed material within the confined space of the blind die. Consequently, this uneven distribution of deformation elaboration within the resulting briquette volume is engendered [20–22].

In the images depicting the structure of the MCM after being pressed in a blind die, the outlines of the initial granules are discernible (Figure 4). Simultaneously, the resultant structure captures alterations that transpired within the material during the deformation process. Notably, the periphery of the briquette exhibits higher levels of porosity when contrasted with the central region.

The presence of porosity within the pressed material exerts a detrimental influence the strength properties of the MCM, thereby limiting its suitability as a structural material for part fabrication. In order to achieve heightened performance, the enhancement and refinement of the material's structure can be achieved through subsequent thermomechanical treatment involving increased degrees of deformation.

Within this study, we undertook the process of hot direct pressing through a cone die and scrutinized the impact of the elongation ratio on the structure and properties of the resultant composite material.

Hot direct pressing denotes deformation of a briquette, wherein heated pressed material flows continuously into the deformation center. This process yields alterations not only in the material's shape but also in

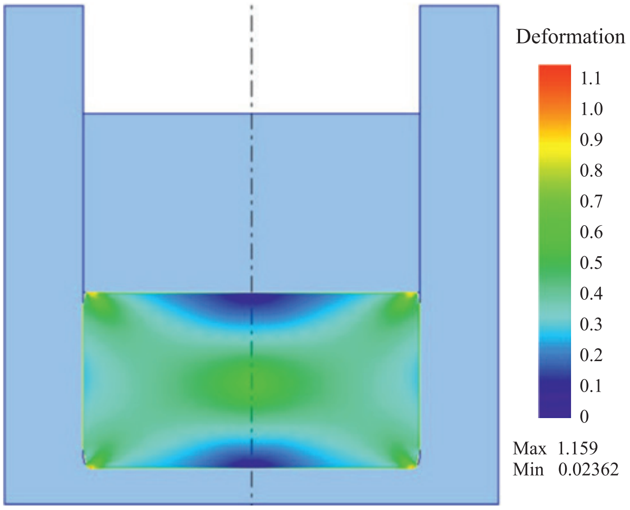

Fig. 3. Results of modeling the MCM sample pressing process in a blind die

Рис. 3. Результаты моделирования процесса прессования образца МКМ в глухой матрице

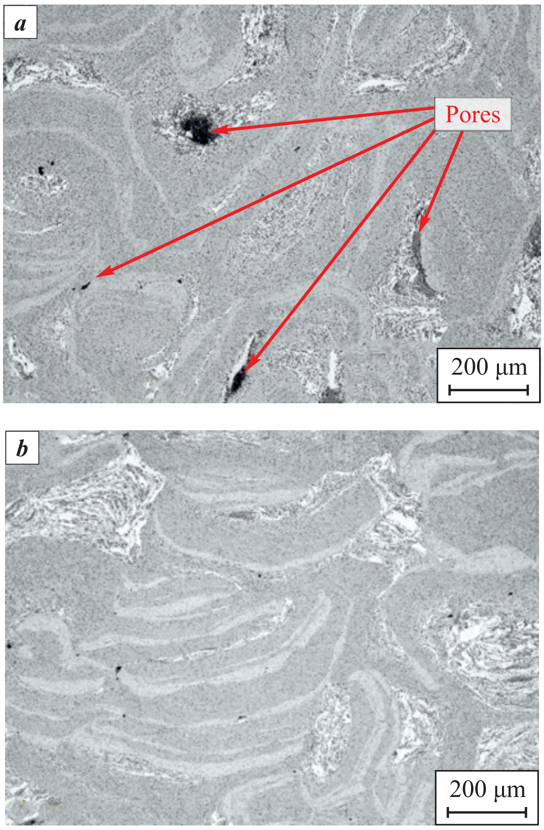

Fig. 4. Structure of the MCM sample pressed in a closed blind die
a and ***b*** – peripheral and central parts of the briquette, respectively

Рис. 4. Структура прессованного в закрытой обойме образца МКМ
a и ***b*** – периферийная и центральная части брикета соответственно

its inherent properties. The external forces exerted upon the MCM during direct pressing encompass the male die pressure, normal pressures on the container's side surfaces, the die, and the drawing cylinder, alongside friction forces arising on the contact surfaces between the MCM and the tools. This constellation of forces culminates in material restructuring, correlating with augmented density and heightened strength properties of MCM.

The process parameters that exert considerable influence on the resulting material's structure during pressing have been identified. These parameters comprise the deformation rate (characterizing the rate of movement of the press's male die), the material's outflow speed from the die, and the elongation ratio. The deformation rate, denoting the linear velocity of the press's working piece movement in the primary deformation direction, remains consistent and was set at 10 mm/s in this study. The material's outflow speed from the die and the elongation ratio share an interdependent relationship: the latter determines the extent of deformation within the pressed material, and its elevation leads to a proportional rise in the outflow speed.

It is acknowledged that the presence of a reinforcing element in the form of finely dispersed ceramic particles classifies disperse-reinforced MCM as intricate deformable materials, endowed with notable resistance to deformation. Consequently, to ensure the uniform flow of MCM during deformation and to diminish the requisite pressing force, a conical die shape was selected.

Throughout this study, direct hot pressing processes with elongation ratios (μ) ranging from 10 to 30 were investigated.

The findings revealed that the highest density (more than 99.0 % of the theoretical one) was attained for MCM samples with $\mu \geq 20$. Notably, surface indentations (score lines) emerged on their surfaces in proximity to the discarded area. This particular form of defect is attributed to the gradual thinning of the lubricant layer applied onto the tool during hot direct pressing, coupled with the escalation of contact friction forces within this region. Consequently, the peripheral layers of the pressed bar start to lag behind the central layers. This phenomenon can be mitigated through the utilization of multi-component lubricants or by applying an exceedingly hard coating to the tool's functional surface. Employing the Qform 3D software package for modeling the hot direct pressing process corroborates the outcomes obtained from the experimental work. Cumulative deformation within the peripheral layers of the bar surpasses that within the central region by a factor of 1.25 (Figure 5).

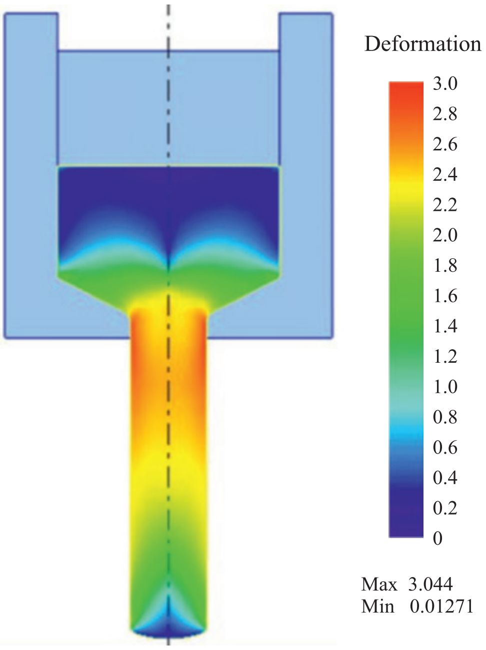

Fig. 5. Results of modeling the process of MCM direct pressing in a cone die

Рис. 5. Результаты моделирования процесса прямого прессования МКМ в конической матрице

The structure of the MCM in the pressing direction exhibits a banded pattern, linked to the material's stress distribution during deformation. Specifically, this is influenced by the presence of tensile stresses aligned along the deformation axis. The boundaries of the granules, which were initially set within the briquette's structure, undergo extension along the axis of compression, thereby shaping the structure depicted in Figure 6. Furthermore, for elongation ratio of $\mu \geq 10$, the structure of the pressed MCM appears non-uniform (see Figure 6, *a*), attributed to inadequate compressive stresses originating within the deformation center. In contrast, at $\mu \geq 20$ and ≥ 30 (Figure 6, *b*, *c*), the structure demonstrates higher uniformity.

Samples were manufactured from the resultant bars for the purpose of conducting tensile tests. The visual representation of these samples is presented in Figure 7.

The mechanical properties of the pressed dispersed-reinforced MCM samples were examined at a temperature of 20 °C. The tabulated data showcases the acquired outcomes for strength (σ_u), yield strength ($\sigma_{0.2}$) and elastic modulus (E).

MCM samples produced with an elongation ratio of ≥ 20, which exhibit a uniform structure, demonstrated superior strength characteristics compared to the samples with $\mu \geq 10$, marked by non-uniform structure. Meanwhile, elevating $\mu \geq 30$ did not result in a significant performance improvement, similar to the density findings detailed earlier.

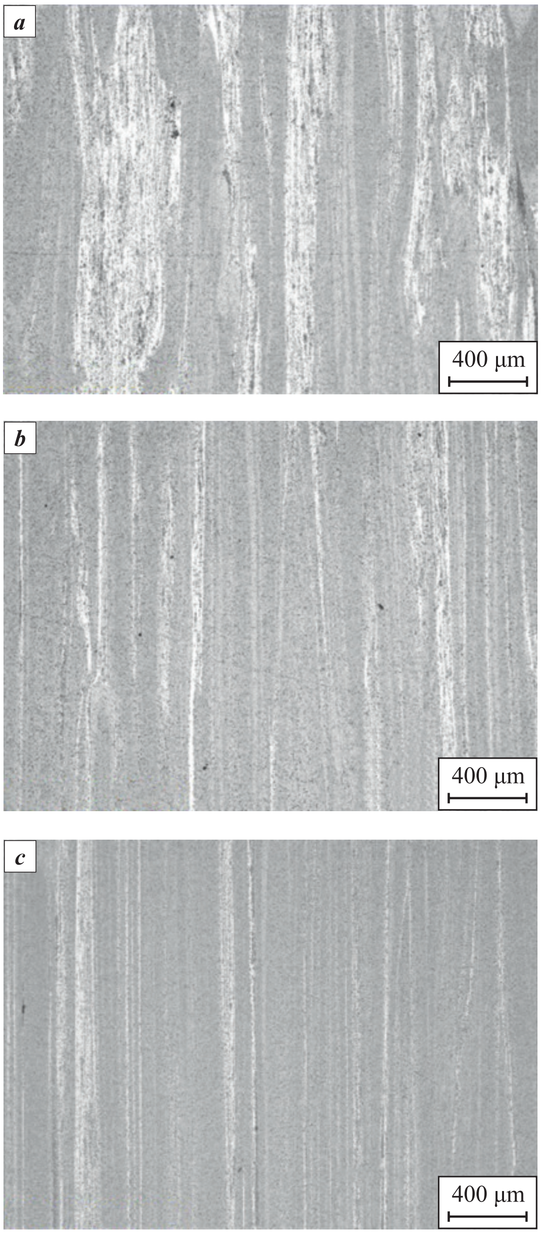

Fig. 6. Structure of MCM bars after direct pressing with elongation ratios of ≥10 (***a***), ≥20 (***b***) and ≥30 (***c***)

Рис. 6. Структура прутков МКМ после прямого прессования с коэффициентами вытяжки ≥10 (***a***), ≥20 (***b***) и ≥30 (***c***)

Values of mechanical parameters of dispersed-reinforced MCM samples in comparison with aluminum alloy of AD31 grade

Значения механических характеристик образцов дисперсно-армированного МКМ в сравнении с алюминиевым сплавом марки АД31

Sample	μ	σ_u, MPa	$\sigma_{0.2}$, MPa	*E*, GPa
MCM	≥10	290–300	235–240	87–93
	≥20	300–305	240–245	88–94
	≥30	300–305	240–245	87–95
AD31	–	240–250	200–205	71–73

Fig. 7. Samples of dispersed-reinforced MCM for tensile testing

Рис. 7. Образцы из дисперсно-армированного МКМ для испытаний на растяжение

Conclusions

1. Thermomechanical treatment of dispersed-reinforced aluminum alloy-based MCM through blind die pressing enables the production of material with porosity ranging from 5 to 10 %.

2. Once the density reaches a threshold of 90–95 % of the theoretical value, is compaction of dispersed-reinforced MCM decelerates, and further augmentation of the pressing force does not lead to increased density.

3. Subsequent thermomechanical treatment, characterized by intensified material deformation, enhances the structure and attributes of the aluminum alloy-based MCM obtained.

4. Hot direct pressing with the elongation ratio greater than 20 yields dispersed-reinforced aluminum alloy-based MCM featuring a uniform structure, density surpassing 99.0 % of the theoretical value and heightened mechanical properties: $\sigma_u = 300 \div 305$ MPa and $E = 87 \div 95$ HPa.

References / Список литературы

1. Kablov E.N. Composites: Today and tomorrow. *Metally Eurazii*. 2015;1:36–39. (In Russ.).

   Каблов Е.Н. Композиты: сегодня и завтра. *Металлы Евразии*. 2015;1:36–39.

2. Kablov E.N. Innovative developments of the Federal State Unitary Enterprise “VIAM” of the State Scientific Center of the Russian Federation for the implementation of the “Strategic directions for the development of materials and technologies for their processing for the period up to 2030”. *Aviationnye materialy i technologii*. 2015;1(34): 3–33. (In Russ.). https://doi.org/10.18577/2071-9140-2015-0-1-3-33

Каблов Е.Н. Инновационные разработки ФГУП «ВИАМ» ГНЦ РФ по реализации «Стратегических направлений развития материалов и технологий их переработки на период до 2030 года». *Авиационные материалы и технологии*. 2015;1(34):3–33.
https://doi.org/10.18577/2071-9140-2015-0-1-3-33

3. Fakhir Aziz Rasul Rozhbiany, Shawnim Rashied Jalal Reinforcement and processing on the machinability and mechanical properties of aluminum matrix composites. *Journal of Materials Research and Technology*. 2019;8(5):4766–4777.
https://doi.org/10.1016/j.jmrt.2019.08.023

4. Alaneme K.K., Bodunrin M.O. Corrosion behavior of alumina reinforced aluminium (6063) metal matrix composites. *Journal of Minerals and Materials Characterization and Engineering*. 2011;10(12):1153–1165.
https://dx.doi.org/10.4236/jmmce.2011.1012088

5. Sheng-Han Li and Chuen-Guang Chao. Effects of carbon fiber/Al interface on mechanical properties of carbon-fiber-reinforced aluminum-matrix composites. *Metallurgical and Materials Transactions A*. 2004; 35(7):2153–2160.
https://doi.org/10.1007/s11661-004-0163-z

6. Singh J., Chauhan A. Characterization of hybrid aluminum matrix composites for advanced applications – A review. *Journal of Materials Research and Technology*. 2015;3(2).
https://doi.org/10.1016/j.jmrt.2015.05.004

7. Antipov V.V. Prospects for development of aluminum, magnesium and titanium alloys for aerospace engeneering. *Aviatsionnye materialy i technologii*. 2017;S:186–194. (InRuss.).
https://dx.doi.org/10.18577/2071-9140-2017-0-S-186-194

Антипов В.В. Перспективы развития алюминиевых, магниевых и титановых сплавов для изделий авиационно-космической техники. *Авиационные материалы и технологии*. 2017;S:186–194.
http://dx.doi.org/10.18577/2071-9140-2017-0-S-186-194

8. Grashchenkov D.V. Strategy of development of non-metallic materials, metal composite materials and heat-shielding. *Aviatsionnye materialy i technologii*. 2017;S: 264–271. (In Russ.).
https://dx.doi.org/10.18577/2071-9140-2017-0-S-264-271

Гращенков Д.В. Стратегия развития неметаллических материалов, металлических композиционных материалов и теплозащиты. *Авиационные материалы и технологии*. 2017;S:264–271.
https://dx.doi.org/10.18577/2071-9140-2017-0-S-264-271

9. Kablov E.N., Grashchenkov D.V., Shchetanov B.V., Shavnev A.A., et al. AlSiC-based metal matrix composites for power electronic devices. *Composites: Mechanics, Computations, Applications*. 2013; 4:(1):65–74.
https://dx.doi.org/10.1615/CompMechComputApplIntJ.v4.i1.40

10. Stoyakina E.A., Kurbatkina E.I., Simonov V.N., Kosolapov D.V., Gololobov A.V. Russ. Mechanical properties of aluminum-matrix composite materials reinforced with SiC particles, depending on the matrix alloy (review). *Trudy VIAM*. 2018;2:62–73. (In Russ.).
https://doi.org/10.18577/2307-6046-2018-0-2-8-8

Стоякина Е.А., Курбаткина Е.И., Симонов В.Н., Косолапов Д.В., Гололобов А.В. Механические свойства алюмоматричных композиционных материалов, упрочненных частицами SiC, в зависимости от матричного сплава. *Труды ВИАМ*. 2018;2:62–73.
https://doi.org/10.18577/2307-6046-2018-0-2-8-8

11. Nyafkin A.N., Loshinin Yu.V., Kurbatkina E.I., Kosolapov D.V. Investigation of the influence of silicon carbide fractional composition on thermal conductivity of composite material based on aluminum alloy. *Trudy VIAM*. 2019;(11):53–59. (In Russ.).
https://doi.org/10.18577/2307-6046-2019-0-11-53-59

Няфкин А.Н., Лощинин Ю.В., Курбаткина Е.И., Косолапов Д.В. Исследование влияния фракционного состава карбида кремния на теплопроводность композиционного материала на основе алюминиевого сплава. *Труды ВИАМ*. 2019;(11):53–59.
https://doi.org/10.18577/2307-6046-2019-0-11-53-59

12. El Moumen A., Kanit T., Imad A., El Minor H. Effect of reinforcement shape on physical properties and representative volume element of particles-reinforced composites: Statistical and numerical approaches. *Mechanics of Materials*. 2015;(83):1–16.
https://doi.org/10.1016/j.mechmat.2014.12.008

13. Yuan W., Zhang J., Zhang C., Chen Z. Processing of ultrahigh strength SiCp/Al–Zn–Mg–Cu composites. *Journal of Materials Processing Technology*. 2009;209(7):3251–3255.
https://doi.org/10.1016/j.jmatprotec.2008.07.030

14. Kosolapov D.V., Shavnev A.A., Kurbatkina E.I., Nyafkin A.N., Gololobov A.V. Study of structure and properties of dispersion hardened MCM based on aluminum alloy of Al–Mg–Si system. *Trudy VIAM*. 2020;(1):58–67. (In Russ.).
https://doi.org/10.18577/2307-6046-2020-0-1-58-67

Косолапов Д.В., Шавнев А.А., Курбаткина Е.И., Няфкин А.Н., Гололобов А.В. Исследование структуры и свойств дисперсно-упрочненного МКМ на основе алюминиевого сплава системы Al–Mg–Si. *Труды ВИАМ*. 2020;(1):58–67.
https://doi.org/10.18577/2307-6046-2020-0-1-58-67

15. Miller W.S., Humphreys F.J. Strengthening mechanisms in particulate metal matrix composites. *Scripta Metallurgica et Materialia*. 1991;25(1):33–38.
https://doi.org/10.1016/0956-716X(91)90349-6

16. Abdoli H., Salahi E., Farnoush H., Pourazrang K. Evolutions during synthesis of Al–AlN-nanostructured composite powder by mechanical alloying. *Journal of Alloys and Compounds*. 2008;461(1–2):166–172.
https://doi.org/10.1016/j.jallcom.2007.07.054

17. Berezovsky V.V., Shavnev A.A., Lomov S.B., Kurganova Yu.A. Receiving and the analysis of structure of the disperce strengthened composite materials of Al-SiC system with the different maintenance of the reinforcing phase. *Aviatsionnye materialy i technologii*. 2014;S(6): 17–23. (In Russ.).
https://doi.org/10.18577/2071–9140–2014–0–s6–17–23

Березовский В.В., Шавнев А.А., Ломов С.Б., Курганова Ю.А. Получение и анализ структуры дисперсноупрочненных композиционных материалов системы Al–SiC с различным содержанием армирую-

щей фазы. *Авиационные материалы и технологии*. 2014;S(6):17–23.
http://dx.doi.org/10.18577/2071-9140-2014-0-s6-17-23

18. Ranjit Bauri, Mirle Surappa. Processing and properties of Al–Li–SiCp composites. *Science and Technology of Advanced Materials*. 2007;8(6):494–502.
https://doi.org/10.1016/j.stam.2007.07.004

19. Ogie N.A., Oyejide O.J., Akusu O.M., Udumebraye J.E. Effect of compaction on thermal conductivity of aluminium powder. *International Journal of Emerging Engineering Research and Technology*. 2018;6(2):1–5.

20. Kumar V.R., Mahesh N.S., Anwar M.I. Numerical analysis of powder compaction to obtain high relative density in ‘601AB’ aluminum powder. *SasTech Journal*. 2012;11(1):79–84.

21. Radu Muresan. Research into the warm compaction of metal powders. *Materials Research Proceedings*. 2018;8: 152–156. http://dx.doi.org/10.21741/9781945291999-17

22. Nyafkin A.N., Shavnev A.A., Kurbatkina E.I., Kosolapov D.V. Studying the effect of silicon carbide particle size on the thermal coefficient linear expansion of the composite material based on aluminum alloy. *Trudy VIAM*. 2020;(2):41–49. (In Russ.).
https://dx.doi.org/10.18577/2307-6046-2020-0-2-41-49

Няфкин А.Н., Шавнев А.А., Курбаткина Е.И., Косолапов Д.В. Исследование влияния размера частиц карбида кремния на температурный коэффициент линейного расширения композиционного материала на основе алюминиевого сплава. *Труды ВИАМ*. 2020;(2):41–49.
https://dx.doi.org/10.18577/2307-6046-2020-0-2-41-49

Information about the Authors

Andrey N. Nyafkin – Head of the Section of Laboratory No. 626, All-Russian Scientific Research Institute of Aviation Materials of the National Research Center “Kurchatov Institute” – VIAM (NRC “Kurchatov Institute” – VIAM).
E-mail: andrey.viam@mail.ru

Dmitry V. Kosolapov – Deputy Head of Laboratory No. 626, NRC “Kurchatov Institute” – VIAM.
E-mail: d.kosolapov87@gmail.com

Elena I. Kurbatkina – Cand. Sci. (Eng.), Head of Laboratory No. 626, NRC “Kurchatov Institute” – VIAM.
ORCID: 0000-0001-8458-2332
E-mail: elena.kurbatkina@mail.ru

Сведения об авторах

Андрей Николаевич Няфкин – начальник участка лаборатории № 626, Всероссийский научно-исследовательский институт авиационных материалов Национального исследовательского центра «Курчатовский институт» (НИЦ «Курчатовский институт» – ВИАМ).
E-mail: andrey.viam@mail.ru

Дмитрий Викторович Косолапов – заместитель начальника лаборатории № 626, НИЦ «Курчатовский институт» – ВИАМ.
E-mail: d.kosolapov87@gmail.com

Елена Игоревна Курбаткина – к.т.н., начальник лаборатории № 626, НИЦ «Курчатовский институт» – ВИАМ.
ORCID: 0000-0001-8458-2332
E-mail: elena.kurbatkina@mail.ru

Contribution of the Authors

A. N. Nyafkin – conceptualized the main ideas, defined the study’s objectives, formulated the research questions, devised experimental protocols, determined modes of thermomechanical treatment, and authored the paper’s content.
D. V. Kosolapov – prepared mixtures, conducted thermomechanical treatments, analyzed experimental outcomes, assessed sample properties, performed calculations, and contributed to data interpretation.
E. I. Kurbatkina – provided scientific supervision, reviewed and revised the manuscript, refined conclusions, and ensured textual accuracy.

Вклад авторов

А. Н. Няфкин – формирование основной концепции, постановка цели и задачи исследования, подготовка экспериментов, подбор режимов деформационно-термической обработки, написание текста статьи.
Д. В. Косолапов – приготовление смеси и проведение деформационно-термической обработки, анализ полученных результатов экспериментов и исследований свойств образцов, выполнение расчетов.
Е. И. Курбаткина – научное руководство, корректировка текста, корректировка выводов.

Received 07.04.2022
Revised 05.06.2023
Accepted 01.07.2023

Статья поступила 07.04.2022 г.
Доработана 05.06.2023 г.
Принята к публикации 01.07.2023 г.

Refractory, Ceramic and Composite Materials
Тугоплавкие, керамические и композиционные материалы

UDC 542.943:546.831

https://doi.org/10.17073/1997-308X-2023-3-30-37

Research article
Научная статья

High-temperature oxidation of ZrB_2–SiC–La_2O_3 ceramic material produced via spark plasma sintering

V. B. Kulmetyeva, V. E. Chuvashov, K. N. Lebedeva, S. E. Porozova✉, M. N. Kachenyuk

Perm National Research Polytechnic University
29 Komsomolsky Prosp., Perm 614000, Russia

✉ sw.porozova@yandex.ru

Abstract. The study investigated the influence of La_2O_3 addition on the oxidation properties of composite ceramics with a composition of 80 vol. % ZrB_2 and 20 vol. % SiC. The source materials utilized in this study included zirconium diboride (DPTP Vega LLC., Russia), grade 63C silicon carbide (Volzhsky Abrasive Works JSC, Russia), and lanthanum hydroxide concentrate (Solikamsk Magnesium Plant JSC, Russia), with the following elemental content (wt. %): La – 54.2, Nd – 4.3, Pr – 2.8, and trace amounts of other elements (<0.1). The La_2O_3 content in the charge varied between 0, 2 and 5 vol. %. The powders were mixed in a planetary mill with ethyl alcohol as the medium for 2 h, using a grinding media to powder ratio of 3:1. Consolidation of the powders was achieved through spark plasma sintering at 1700 °C, applying a pressing pressure of 30 MPa. The heating rate was 50 °C/min, and the isothermal holding time was 5 min. Oxidation was carried out in air at 1200 °C and the total oxidation time was 20 h. Oxidation experiments were conducted in air at 1200 °C, with a total oxidation time of 20 h. It was observed that the most significant weight gain occurred within the first 2–4 h of testing. Specimens containing 5 vol. % La_2O_3 exhibited the smallest weight gain after 20 h of exposure. Regardless of the presence of La_2O_3, silicon carbide was found to be the first material to undergo oxidation. In specimens without La_2O_3 addition, the oxidized layer mainly consisted of silicon monoxide and dioxide. In contrast, specimens with La_2O_3 exhibited a predominantly oxidized layer composed of $ZrSiO_4$ and ZrO_2. The study revealed that the introduction of La_2O_3 intensified the formation of zircon, which subsequently slowed down the oxidation processes in the material.

Keywords: oxidation, spark plasma sintering, zirconium diboride, silicon carbide, lanthanum oxide, oxidized layer, energy dispersive analysis, elemental composition

For citation: Kulmetyeva V.B., Chuvashov V.E., Lebedeva K.N., Porozova S.E., Kachenyuk M.N. High-temperature oxidation of ZrB_2–SiC–La_2O_3 ceramic material produced via spark plasma sintering. *Powder Metallurgy and Functional Coatings*. 2023;17(3): 30–37. https://doi.org/10.17073/1997-308X-2023-3-30-37

Особенности высокотемпературного окисления керамического материала ZrB_2–SiC–La_2O_3, полученного искровым плазменным спеканием

В. Б. Кульметьева, В. Э. Чувашов, К. Н. Лебедева, С. Е. Порозова✉, М. Н. Каченюк

Пермский национальный исследовательский политехнический университет
Россия, 614000, г. Пермь, Комсомольский пр-т, 29

✉ sw.porozova@yandex.ru

Аннотация. Исследовано влияние добавки La_2O_3 на окисление керамики состава, об. %: 80ZrB_2–20SiC. В качестве исходных материалов использовали диборид циркония (ООО ДПТП «Вега», Россия), карбид кремния марки 63С (ОАО «Волжский абразивный завод», Россия) и концентрат гидроксида лантана (ОАО «Соликамский магниевый завод», Россия), содержание элементов в котором составляло, мас. %: La – 54,2, Nd – 4,3, Pr – 2,8, остальные – менее 0,1. Содержание La_2O_3 в шихте варьировалось: 0, 2 и 5 об. %. Смешивание порошков проводили с использованием планетарной мельницы в течение 2 ч в этиловом спирте, соотношение мелющих тел и порошка составляло 3:1. Консолидацию порошков осуществляли методом искрового плазменного спекания при температуре 1700 °C и давлении прессования 30 МПа со скоростью нагрева 50 °C/мин и изотермической выдержкой 5 мин. Окисление проводили на воздухе при температуре 1200 °C, общее время окисления составило 20 ч. Наиболее интенсивное увеличение массы отмечено в течение первых 2–4 ч испытаний. По истечении 20 ч наименьшее увеличение массы наблюдалось у образцов с добавкой 5 об. % La_2O_3. Установлено, что вне зависимости от наличия La_2O_3 карбид кремния первым подвергается окислению. В образцах без добавки La_2O_3 окисленный слой состоит преимущественно из моно- и диоксида кремния, тогда как в образцах с La_2O_3 большую часть окисленного слоя составляют $ZrSiO_4$ и ZrO_2. Таким образом, установлено, что введение La_2O_3 интенсифицирует процесс формирования циркона, что способствует замедлению процессов окисления.

Ключевые слова: окисление, искровое плазменное спекание, диборид циркония, карбид кремния, оксид лантана, окисленный слой, энергодисперсионный анализ, элементный состав

Для цитирования: Кульметьева В.Б., Чувашов В.Э., Лебедева К.Н., Порозова С.Е., Каченюк М.Н. Особенности высокотемпературного окисления керамического материала ZrB_2–SiC–La_2O_3, полученного искровым плазменным спеканием. *Известия вузов. Порошковая металлургия и функциональные покрытия*. 2023;17(3):30–37.
https://doi.org/10.17073/1997-308X-2023-3-30-37

Introduction

To date, the primary concern lies in the development of materials capable of enduring extended periods in oxidizing environments at high temperatures [1–3]. In this regard, a noteworthy focus is on ultra-high-temperature ceramics (UHTC), which consist of a ceramic matrix and a protective structure that shields the surface from oxidation [1; 4; 5]. In order to produce such materials a deliberate selection of additive phases is conducted to facilitate the formation of surface structures that can withstand prolonged exposure to oxidizing environments at high temperatures. One prevalent example of UHTCs is composite materials based on zirconium or hafnium borides, which exhibit high thermal conductivity and thermal shock resistance [6].

Sintering zirconium and hafnium boride powders requires temperatures exceeding 1950 °C due to their strong covalent bonds and low self-diffusion coefficient [7; 8]. The sintering process is typically activated by incorporating sintering additives such as SiC, Si_3N_4, La_2O_3, LaB_6 [9; 10], tantalum, titanium, zirconium, molybdenum silicides, etc. The optimum composition is considered to be the volumetric ratio of 80 % ZrB_2 to 20 % SiC [11; 12]. At high temperatures, the oxidation of these ceramics leads to the formation of a protective multi-layer coating on the surface, consisting of ZrO_2–SiO_2 and borosilicate glass. This coating effectively seals cracks and pores on the UHTC surface, creating a gas-tight film that prevents oxygen diffusion into the material [13; 14].

Spark plasma sintering (SPS) is a relatively recent technique that enables the reduction of sintering temperature and time for certain materials when performed under vacuum or an argon atmosphere [15]. Despite some existing studies in this area, the phase composition, structure, and oxidation properties of boride-based composite materials produced through this process have not been adequately investigated [15–17].

The objective of this study was to examine the impact of La_2O_3 addition on the oxidation properties of composite ceramics with the following volumetric composition: $80ZrB_2$–20SiC.

Materials and Methods of Research

The source materials utilized in this study included:
– zirconium diboride (DPTP Vega LLC., Russia);
– lanthanum hydroxide concentrate (Solikamsk Magnesium Plant JSC, Russia), with the following elemental content (wt. %): La – 54,2, Nd – 4,3, Pr – 2,8 and trace amounts of other elements (<0.1);
– grade 63C silicon carbide (Volzhsky Abrasive Works JSC, Russia).

The particle size distribution of the powders was determined using laser light diffraction with the Analysette 22 NanoTec plant (Fritsch GmbH, Germany). The ZrB_2 powder exhibited a predominant particle size range of 0.5 to 12 μm, with 97 % of particles measuring less than 11.1 μm, and an average particle size of 4.52 μm. The SiC powder demonstrated a bimodal particle size distribution, with an average particle size of 3.47 μm. The $La(OH)_3$ powder exhibited a wide particle size distribution, with an average particle size of 9.76 μm.

In order to convert lanthanum hydroxide into oxide, the material was subjected to annealing at 600 °C for a duration of 1 h in an air atmosphere. The initial powders were mixed using a SAND planetary mill in ethyl alcohol. The grinding process lasted for 2 h at a speed of 160 rpm, a grinding media to powder ratio of 3:1. The mixtures contained lanthanum oxide in two different volumetric percentages: 0, 2 and 5.

The specimens were consolidated using spark plasma sintering (SPS) on the Dr. Synter SPS-1050b equipment

(SPS Syntex, Japan) at a temperature of 1700 °C. Heating was achieved by applying a pulsed direct current at a rate of 50 °C per min. The temperature was monitored using an optical pyrometer placed on the outer side of the graphite matrix. The material was loaded into the system just before the heating process began, while maintaining a constant load at a pressure of 30 MPa. The applied load was removed after the completion of the heating phase. To prevent any undesirable reactions between the sintered powder, matrix, and punches, graphite paper was employed. Additionally, graphite felt was wrapped around the mold to minimize heat losses. The specimens were subjected to an isothermal holding time of 5 min.

The apparent density and open porosity of sintered specimens were analyzed following the guidelines outlined in GOST 2409-2014.

For the oxidation study, the specimens were exposed to air in an electric furnace equipped with silicon carbide heaters. The crucibles containing the specimens were placed in the furnace, preheated to 1200 °C. After a specific duration, the specimens were removed, weighed to record their weight, and then returned to the furnace. The total duration of high-temperature oxidation was 20 h.

The phase composition of the specimens was examined using Raman spectroscopy on a multifunction spectrometer SENTERRA (Bruker, Germany), with a laser wavelength of 532 nm. The acquired data were processed using the OPUS 6.5 software.

Microscopic analysis of the specimens was conducted using an analytical auto emission scanning electron microscope VEGA3 (TESCAN, Czech Republic). In order to determine the elemental composition, an Inca X-Act detector (Oxford Instruments Analytical, Great Britain) was employed for energy-dispersive analysis of the elemental composition of the materials.

Results and Discussion

The investigations were conducted on the materials containing 0, 2 and 5 vol. % of La_2O_3. No significant changes in the apparent density and open porosity of the specimens were observed after the SPS process. The open porosity values ranged from 3.5 to 5.5 % across all variations.

The specimens were subjected to oxidation in an air environment for a duration of 20 h. The time intervals for recording the specific weight gain of the specimens increased as the weight gain decreased. The results are presented in Figure 1. The most substantial weight gain occurred within the initial 2–4 h of testing.

Among the specimens, those with 5 vol. %. of La_2O_3 exhibited the lowest weight gain after the 20-hour exposure. It is worth noting that up to 9 h of exposure, the differences in specific weight gain were minimal. Only with further increases in oxidation time did the impact of La_2O_3 on the material's oxidation resistance become more pronounced.

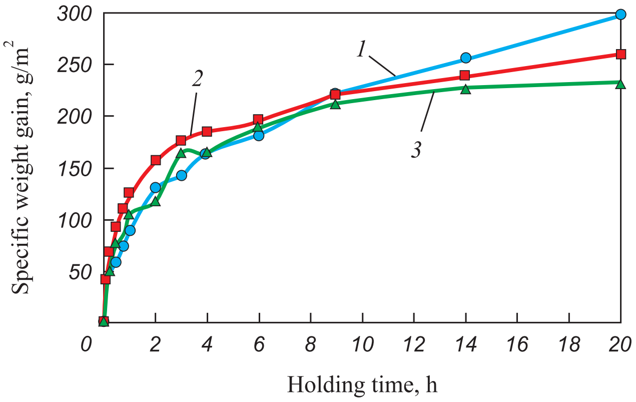

Fig. 1. Specific weight gain of ZrB_2–20 vol. % SiC ceramic specimens with different content of La_2O_3 after oxidation for 20 h at 1200 °C
La_2O_3, vol. %: ***1*** – 0, ***2*** – 2 and ***3*** – 5

Рис. 1. Удельный привес образцов керамики ZrB_2–20 об. % SiC с различным содержанием La_2O_3 после окисления в течение 20 ч при *t* = 1200 °C
La_2O_3, об. %: ***1*** – 0, ***2*** – 2 и ***3*** – 5

It has been established that the resistance of ZrB_2 composite materials to high-temperature oxidation is primarily influenced by the composition of the protective layer formed on the material's surface [18]. The fractures in the specimens were examined using scanning electron microscopy (SEM) along with energy dispersive analysis. SEM images and maps displaying the distribution of silicon, zirconium, and boron within the specimens were obtained (Figure 2: spectrum *1* represents the surface layer of the specimen; spectrum *2* corresponds to an internal structure displaying significant visual dissimilarity; spectrum *3* pertains to a deeper layer of the material).

In the specimen without the addition of La_2O_3, a continuous protective layer composed of silicon-containing phases is formed on its surface (spectrum *1* in Fig. 2). When La_2O_3 is introduced, the silicon content on the specimen surface is also higher (spectrum *1*) compared to the subsequent layers (spectra 2 and *3*). However, the thickness of these layers is significantly reduced. Figure 3 presents a histogram depicting the calculated thickness of the oxidized layers, determined through analysis of the material's microstructure (as shown in Figure 2).

Table 1 displays the outcomes of the energy dispersive analysis, providing the elemental composition of the specimens following a 20-hour oxidation process. The first layer exhibits identical composition across all three cases. Notably, boron is not detected in the spectra, which is consistent with the challenges in accurately capturing elements from the second period of the periodic table using spectral methods [19].

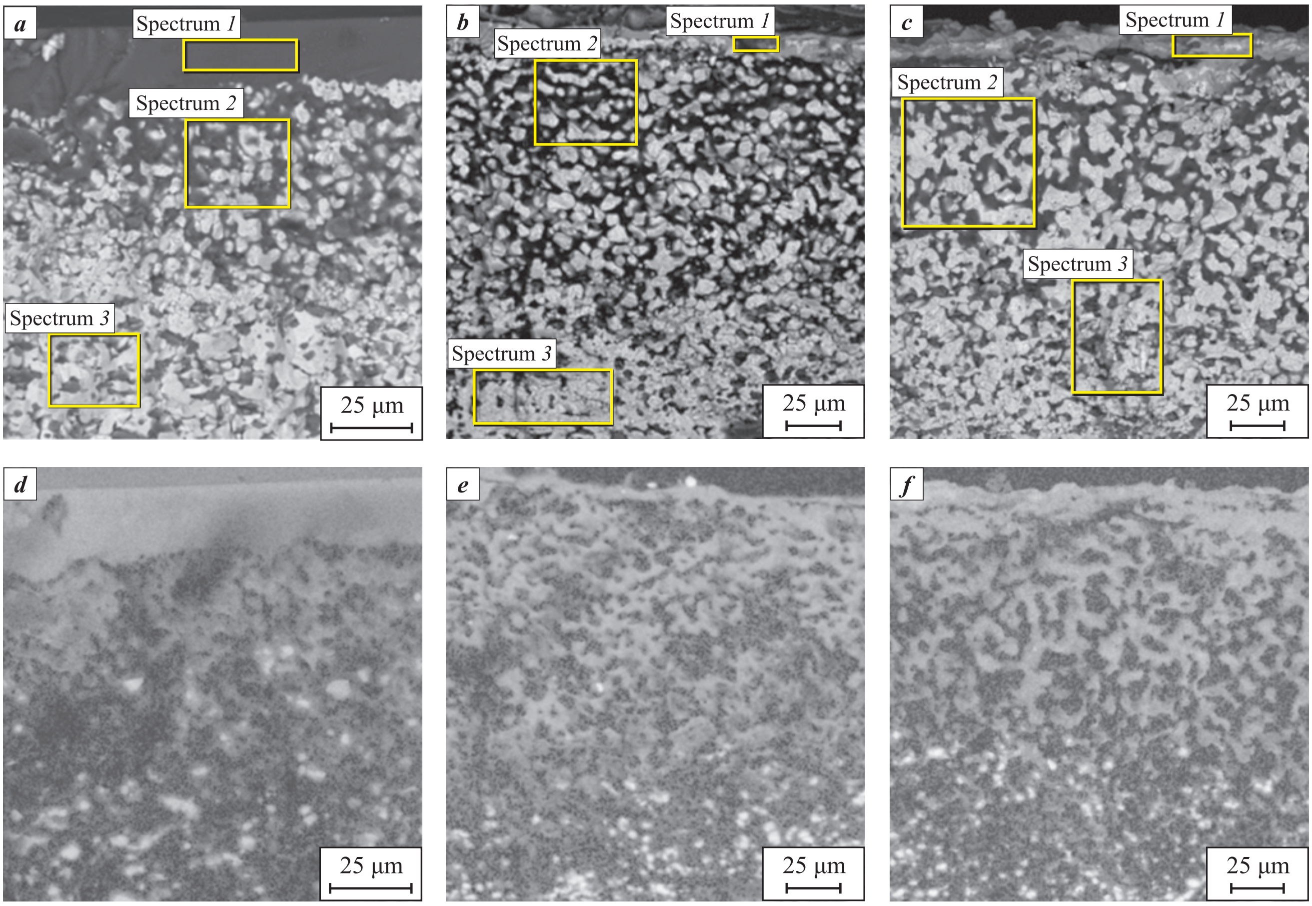

Fig. 2. SEM-images of fractures (***a***–***c***) and silicon distribution maps (***d***–***f***) after oxidation for 20 h of ZrB_2–20 vol. % SiC specimens
Addition of La_2O_3, vol. %: 0 (***a***, ***d***), 2 (***b***, ***e***) and 5 (***c***, ***f***)
White and light gray colors on distribution maps – silicon-containing phases

Рис. 2. СЭМ-изображения изломов (***a***–***c***) и карты распределения кремния (***d***–***f***) после окисления в течение 20 ч образцов состава ZrB_2–20 об. % SiC
Добавка La_2O_3, об. %: 0 (***a***, ***d***), 2 (***b***, ***e***) и 5 (***c***, ***f***)
Белый и светло-серый цвета на картах распределения – кремнийсодержащие фазы

Table 1. **Outcomes of the energy dispersive analysis of the elemental composition of the specimens after oxidation for 20 h**

Таблица 1. **Результаты энергодисперсионного анализа элементного состава образцов после окисления в течение 20 ч**

Imaging place (see Figure 2)	Elemental composition (wt. %) with the addition of La_2O_3, vol. %		
	0	2	5
Spectrum *1* Upper layer	O – 40.43 Si – 54.45 Zr – 2.90	O – 33.36 Si – 12.12 Zr – 54.52	O – 41.41 Si – 12.06 Zr – 46.53
Spectrum *2* Oxidized intermediate layer	O – 38.25 Si – 11.33 Zr – 47.81	O – 46.39 Si – 5.80 Zr – 36.77 B – 9.79 La – 0.55	O – 45.47 Si – 6.10 Zr – 46.96
Spectrum *3* Oxidized layer	O – 8.34 Si – 8.43 Zr – 48.42 B – 34.50	O – 24.96 Si – 3.45 Zr – 57.90 B – 13.13	O – 33.16 Si – 5.28 Zr – 53.60 B – 7.58

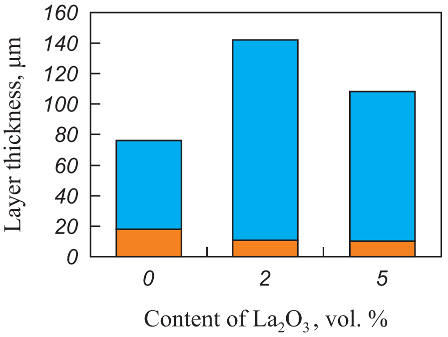

Fig. 3. Dependence of the thickness of oxidized layers on the surface of specimens of the ZrB$_2$–20 vol. % SiC composition without additives and with addition of 2 and 5 vol. % La$_2$O$_3$ after oxidation for 20 h
🟧 – spectrum *1*, 🟦 – spectrum *2* (see Fig. 2)
The third layer is not shown because it was only partially in the imaging area

Рис. 3. Зависимость толщины окисленных слоев на поверхности образцов состава ZrB$_2$–20 об. % SiC без добавки и с введением 2 и 5 об. % La$_2$O$_3$ после окисления в течение 20 ч
🟧 – спектр *1*, 🟦 – спектр *2* (см. рис. 2)
Третий слой не приведен, так как в зону съемки он попал лишь частично

Table 2 presents the results of calculating the atomic composition of the layers, with values rounded to the first decimal place after considering the atomic weights of the elements (and then multiplied by 10).

The assumed chemical composition is derived from the known composition of the initial specimens and the determined element ratios within the layers. The primary stoichiometric phases that are likely to be present are listed in Table 2. It should be noted that the formation of silicon monoxide as a crystalline compound has been previously documented in multiple instances [20–22].

The possibility of non-stoichiometric compound formation, such as borosilicate and borate glasses, should also be taken into consideration [23].

Raman spectroscopy confirmed the presence of zircon (ZrSiO$_4$) and monoclinic zirconium dioxide (ZrO$_2$) as the main phases of the oxidized material (Figure 4) [24]. The imaging was conducted from the surface of the specimens, thereby removing the first layer. One of the obtained spectra is presented, with the others being identical. The only distinction lies in the intensity ratio of the peaks corresponding to the main phases. The absence of silicon oxide lines in the specimen without lanthanum addition can be explained by the fact that well-oxidized phases in the second layer hinder the detection of amorphous or concealed-crystalline silicon oxide phases.

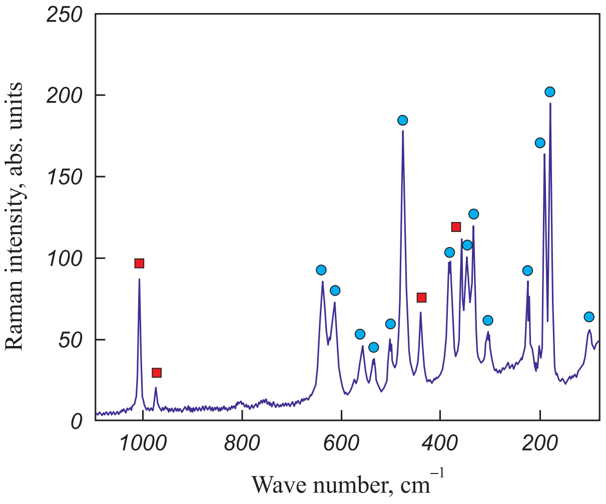

Fig. 4. Fragment of the Raman spectrum of the upper oxidized layer on the surface of a specimen with addition of 5 vol. % La$_2$O$_3$ after oxidation for 20 h
Designations of crystalline phases:
🟥 – zircon; ● – monoclinic zirconium dioxide

Рис. 4. Фрагмент КР-спектра верхнего окисленного слоя на поверхности образца состава с добавкой 5 об. % La$_2$O$_3$ после окисления в течение 20 ч
Обозначения кристаллических фаз:
🟥 – циркон; ● – моноклинный диоксид циркония

Table 2. **Ratio of elements in the layers after oxidation**

Таблица 2. **Соотношение элементов в слоях после окисления**

Imaging place (see Figure 2)	Ratio of elements and the most probable chemical composition with the La$_2$O$_3$ content, vol. %		
	0	2	5
Spectrum *1* Upper layer	**Zr$_{0,3}$Si$_{19}$O$_{25}$** SiO$_2$ and SiO	**Zr$_6$Si$_4$O$_{21}$** ZrSiO$_4$ and ZrO$_2$ Insignificant oxygen excess	**Zr$_5$Si$_4$O$_{26}$** ZrSiO$_4$ and ZrO$_2$ Oxygen excess
Spectrum *2* Oxidized intermediate layer	**Zr$_5$Si$_4$O$_{24}$** ZrSiO$_4$ and ZrO$_2$ Oxygen excess	**Zr$_4$Si$_2$O$_{29}$B$_9$** ZrB$_2$, ZrSiO$_4$ Oxygen excess	**Zr$_5$Si$_2$O$_{28}$** ZrSiO$_4$ and ZrO$_2$ Oxygen excess
Spectrum *3* Oxidized layer	**Zr$_5$Si$_3$O$_5$B$_{32}$** ZrB$_2$, SiO$_2$ or SiO Significant boron excess	**Zr$_6$SiO$_{16}$B$_{12}$** ZrB$_2$, SiO$_2$ Oxygen excess	**Zr$_6$Si$_2$O$_{21}$B$_7$** ZrB$_2$, ZrSiO$_4$ Oxygen excess

There is a noticeable disparity in the distribution of zirconium on the surface of specimens with and without La_2O_3 (Figure 5, *a–c*). In the case without La_2O_3, ZrO_2, despite its relatively low overall content (as seen in Table 1), is distributed relatively (Figure 5, *a*). Presumably, it is integrated within the primary silicon-containing phases. However, the addition of lanthanum oxide results in the growth of zirconium-bearing phase grains and the emergence of agglomerates and large pores between these phases. In this scenario, the formation of silicon oxides is unlikely.

Figure 5, *d* illustrates a fragment of the boron distribution map in the upper layer of the specimen containing 5 vol. % La_2O_3, corresponding to the fragment of the zirconium distribution map in Figure 5, *c*. Since boron could not be detected during the determination of the mass content of elements (as indicated in Table 1), it can be inferred that boron is present in the form of silicate glasses (refer to Figure 2, *f*) that fill the gaps between zircon and zirconium dioxide grains [25].

Consequently, on the surface of specimens without La_2O_3 additives, phases comprising silicon oxides with traces of boron and zirconium oxides are formed. In the presence of La_2O_3 additives, the main phases observed are zirconium dioxide and zircon, along with an excess of oxygen. However, neither case effectively acts as a significant barrier against the deep penetration of oxygen into the material. The presence of lanthanum oxide appears to enhance the formation of zircon, a phase that exhibits greater resistance to thermal shock than monoclinic zirconium dioxide and contributes to the deceleration of the oxidation process.

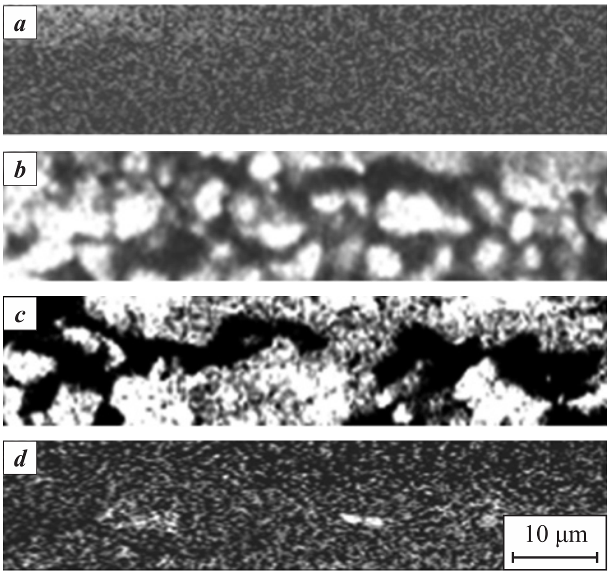

Fig. 5. Fragments of distribution maps of zirconium (***a–c***) and boron (***d***)

Рис. 5. Фрагменты карт распределения циркония (***a–c***) и бора (***d***)

Conclusion

The aim of the study was to investigate the impact of La_2O_3 addition on the oxidation properties of composite ceramics with a composition of 80 vol. % ZrB_2 and 20 vol. % SiC, consolidated through spark plasma sintering. The materials were examined in three variations: without La_2O_3, with 2 vol. % La_2O_3 and 5 vol. % La_2O_3. In all cases, SiC acted as a sacrificial material, being the first to undergo oxidation. Specimens without La_2O_3 addition exhibited a surface layer consisting mainly of SiO_2 and SiO. On the other hand, specimens with La_2O_3 addition showcased surface layers composed primarily of $ZrSiO_4$ and ZrO_2.

Consequently, the introduction of La_2O_3 intensified the formation of zircon and decelerated the oxidation processes. However, it did not serve as a complete barrier to the deep penetration of oxygen into the material.

References / Список литературы

1. Grigor'ev O.N., Frolov G.A., Evdokimenko Ju.I,. Kisel' V.M., Panasjuk A.D., Melah L.M., Kotenko V.A., Koroteev A.V.Ultra-high temperature ceramics for aerospace technology. *Aviacionno-kosmicheskaja tehnika i tehnologija*. 2012;8(95):119–128. (In Russ.).

   Григорьев О.Н., Фролов Г.А., Евдокименко Ю.И., Кисель В.М., Панасюк А.Д., Мелах Л.М., Котенко В.А., Коротеев А.В. Ультравысокотемпературная керамика для авиационно-космической техники. *Авиационно-космическая техника и технология*. 2012;8(95):119–128.

2. Naruckaja A.S., Istomin N.D. Oxidative behavior of high-temperature ceramics based on zirconium diboride. Prospects for the Development of Fundamental Sciences. In: *Proceedings of the XVIII International Conference of Students, Postgraduates and Young Scientists (Tomsk, 27–30.04.2021). Vol. 2. Khimija* (Eds. I.A. Kurzina, G.A. Voronova. Tomsk: Tomskii politehnicheskii universitet, 2021. P. 164–166. (In Russ.).

   Наруцкая А.С., Истомин Н.Д. Окислительное поведение высокотемпературных керамик на основе диборида циркония. Перспективы развития фундаментальных наук. В сб.: *Труды XVIII Международной конференции студентов, аспирантов и молодых ученых (Томск, 27–30 апреля 2021 г.). Т. 2. Химия*. Под ред. И.А. Курзиной, Г.А. Вороновой. Томск: Изд-во Томского политехнического университета, 2021. С. 164–166.

3. Iatsyuk I.V., Potanin A.Yu., Rupasov S.I., Levashov E.A. Kinetics and high-temperature oxidation mechanism of ceramic materials in ZrB_2–SiC–$MoSi_2$ system. *Russian Journal of Non-Ferrous Metals*. 2018;59(1):76–81. https://doi.org/10.3103/S1067821218010157

   Яцюк И.В., Потанин А.Ю. Рупасов С.И., Левашов Е.А. Кинетика и механизм высокотемпературного окисления керамических материалов в системе ZrB_2–SiC–$MoSi_2$. *Известия вузов. Цветная металлургия*. 2017;(6): 63–69. https://doi.org/10.17073/0021-3438-2017-6-63-69

4. Zhitnyuk S.V. Oxygen-free ceramic materials for the space technics (review). *Trudy VIAM*. 2018;(8):81–88. (In Russ.). https://doi.org/10.18577/2307-6046-2018-0-8-81-88

Житнюк С.В. Бескислородные керамические материалы для аэрокосмической техники (обзор). *Труды ВИАМ*. 2018;(8):81–88. https://doi.org/10.18577/2307-6046-2018-0-8-81-88

5. Poilov V.Z., Pryamilova E.N. Thermodynamics of oxidation of zirconium and hafnium borides. *Russian Journal of Inorganic Chemistry*. 2016;61(1):55–58. https://doi.org/10.1134/S0036023616010198

Пойлов В.З., Прямилова Е.Н. Термодинамика окисления боридов циркония и гафния. *Журнал неорганической химии*. 2016;61(1):59–62. https://doi.org/10.7868/S0044457X16010190

6. Li W., Cheng T., Li D., Fang D. Numerical simulation for thermal shock resistance of ultra high temperature ceramics considering the effects of initial stress field. *Advances in Materials Science and Engineering*. 2011;1–7:757543. https://doi.org/10.1155/2011/757543

7. Rangaray L., Surecha S.J, Divakar C., Jayaram V. Low-temperature processing of ZrB$_2$–ZrC composites by reactive hot pressing. *Metallurgical and Materials Transactions A*. 2008;39(7):1496–1505. https://doi.org/10.1007/s11661-008-9500-y

8. Gasch M.J., Ellerby D.T., Johnson S.M. Ultra high temperature ceramic composites. In: *Handbook of Ceramic Composites*. Boston: Springer, 2005. P. 197–224. https://doi.org/10.1007/0-387-23986-3_9

9. Gozalez-Julian J., Cedillos-Barraza O., Döringet S. Enhanced oxidation resistance of ZrB$_2$/SiC composite through in situ reaction of gadolinium oxide in patterned surface cavities. *Journal of the European Ceramic Society*. 2014;34(16):4157–4166. https://doi.org/10.1016/j.jeurceramsoc.2014.07.015

10. Paul A., Jayaseelan D.D., Venugopal S., Zapata-Solvas E., Binner J., Vaidhyanathan B., Heaton A., Brown P., Lee W.E. UHTC composites for hypersonic applications. *American Ceramic Society Bulletin*. 2012; 91(1);22–29.

11. Chamberlain A., Fahrenholtz W., Hilmas G., Ellerby D. Oxidation of ZrB$_2$–SiC ceramics under atmospheric and reentry conditions. *Refractory Applications Transactions*. 2005;1(2):1–8.

12. Bellosi A., Monteverde F. Fabrication and properties of zirconium diboride-based ceramics for UHT applications. In: *Proc. 4th European Workshop. «Hot Structures and Thermal Protection Systems for Space Vehicles»* (Palermo, Italy 26–29 November 2002). Paris: European Space Agency, 2003. P. 65–71.

13. Justin J.F., Jankowiak A. Ultra high temperature ceramics: densification, properties and thermal stability. *AerospaceLab Journal*. 2011;3:1–11.

14. Bellosi A., Guicciardi S., Medri V., Monteverde F., Scitti D., Silvestroni L. Processing and properties of ultra-refractory composites based on Zr- and Hf-borides: state of the art and perspectives. In: *Boron rich solids: Sensors, ultra high temperature ceramics, thermoelectrics, armor*. 2011, P. 147–160. https://doi.org/10.1007/978-90-481-9818-4

15. Sonber J. K., Suri A. K. Synthesis and consolidation of zirconium diboride: review. *Advanced in applied ceramics. Structural, Functional and Bioceramics*. 2011;110(6):321–334. https://doi.org/10.1179/1743676111Y.0000000008

16. Sciti D., Silvestroni L., Bellosi A. Fabrication and properties of HfB$_2$–MoSi$_2$ composites produced by hot pressing and spark plasma sintering. *Journal of Materials Science*. 2006;21(6):1460–1466. https://doi.org/10.1557/jmr.2006.0180

17. Perevislov S.N., Nesmelov D.D., Tomkovich M.V. SiC and Si$_3$N$_4$-based materials obtained by spark plasma sintering. *Fizika tverdogo tela. Vestnik Nizhegorodskogo universiteta imeni N.I. Lobachevskogo*. 2013;2(2):107–114. (In Russ.).

Перевислов С.Н., Несмелов Д.Д., Томкович М.В. Получение материалов на основе SiCi и Si$_3$N$_4$ методом высокотемпературного плазменного спекания. *Физика твердого тела. Вестник Нижегородского университета им. Н.И. Лобачевского*. 2013;2(2):107–114.

18. Hurbert D.M., Jiang D., Dudina D.V., Mukherjee A.K. The synthesis and consolidation of hard materials by spark plasma sintering. *International Journal of Refractory Metals and Hard Materials*. 2009;27(2):367–375. https://doi.org/10.1016/j.ijrmhm.2008.09.011

19. Hiller V.V. X-ray spectral microanalysis of boron content in the core of fiber blanks. problems of theoretical and experimental chemistry. In: *Abstracts of the XXIV Russian Youth Scientific Conference Dedicated to the 170th Anniversary of the Discovery of the Chemical Element Ruthenium* (Ekaterinburg, 23–25.04.2014). Yekaterinburg: Izdatel'stvo UrFU, 2014. P. 80–81. (In Russ.).

Хиллер В.В. Рентгеноспектральный микроанализ содержания бора в сердцевине заготовок оптоволокна. Проблемы теоретической и экспериментальной химии. В сб.: *Тезисы докладов XXIV Российской молодежной научной конференции, посвященной 170-летию открытия химического элемента рутений* (Екатеринбург, 23–25 апреля 2014 г.). Екатеринбург: Изд-во УрФУ, 2014. С. 80–81.

20. Gribov B.G., Zinov'ev K.V., Kalashnik O.N., Gerasimenko N.N., Smirnov D.I., Sukhanov V.N. Structure and phase composition of silicon monoxide. *Semiconductors*. 2012;46(13):1576–1579. https://doi.org/10.1134/S106378261213009X

Грибов Б.Г., Зиновьев К.В., Калашник О.Н., Герасименко Н.Н., Смирнов Д.И., Суханов В.Н. Структура и фазовый состав монооксида кремния. *Известия вузов. Электроника*. 2011;4(90);3–8.

21. Al Kaabi Khalid, Prasad Dasari L.V.K., Kroll P. Silicon monoxide at 1 atm and elevated pressures: Crystalline or Amorphous? *Journal of the American Chemical Society*. 2014;136(9):3410–3423. https://doi.org/10.1021/ja409692c

22. Gribov B.G., Zinov'ev K.V., Kalashnik O.N., Gerasimenko N.N., Smirnov D.I., Sukhanov V.N. Growth of nanocrystalline silicon from a matrix of amorphous silicon monoxide. *Semiconductors*. 2013;47(13):1684–1686. https://doi.org/10.1134/S1063782613130071

Грибов Б.Г., Зиновьев К.В., Калашник О.Н., Герасименко Н.Н., Смирнов Д.И., Суханов В.Н. Выращивание нанокристаллического кремния из матрицы аморфного монооксида кремния. *Известия вузов. Электроника*. 2012;96(4):13–18.

23. Ehrt D. Structure, properties and applications of borate glasses. *Glass Technology: European Journal of Glass Science and Technology. Part A*. 2000;41(6):182–185.

24. Orlov R.Yu., Vigasina M.F., Uspenskaya M.E. Raman spectra of minerals (reference book). Moscow: GEOS, 2007. 142 p. (In Russ.).

Орлов Р.Ю., Вигасина М.Ф., Успенская М.Е. Спектры комбинационного рассеяния минералов: Справочник. М.: ГЕОС, 2007. 142 с.

25. Ban'kovskaya I.B., Kolovertnov D.V. Effect of the thermal treatment mode on the composition and structure of ZrB_2–SiC system composites. *Glass Physics and Chemistry*. 2013;39(5);579–588. https://doi.org/10.1134/S1087659613050027

Баньковская И.Б., Коловертнов Д.В. Влияние режима термообработки на состав и структуру композитов системы ZrB_2–SiC. *Физика и химия стекла*. 2013;39(5):816–828.

Information about the Authors

Valentina B. Kulmetyeva – Cand. Sci. (Eng.), Associate Professor, Department of Mechanics of Composite Materials and Structures, Perm National Research Polytechnic University (PNRPU).
ORCID: 0000-0002-5214-0932
E-mail: kulmetevavb@pstu.ru

Vyacheslav E. Chuvashov – PhD student, Department of Mechanics of Composite Materials and Structures, PNRPU.
ORCID: 0009-0000-0171-2024
E-mail: slavachuvashov@yandex.ru

Kseniya N. Lebedeva – Master's Student, Department of Mechanics of Composite Materials and Structures, PNRPU.
ORCID: 0009-0003-6134-2952
E-mail: lebedkseni@mail.ru

Svetlana E. Porozova – Dr. Sci. (Eng.), Professor, Department of Mechanics of Composite Materials and Structures, PNRPU.
ORCID: 0000-0001-5835-9727
E-mail: sw.porozova@yandex.ru

Maksim N. Kachenyuk – Dr. Sci. (Eng.), Associate Professor, Department of Mechanics of Composite Materials and Structures, PNRPU.
ORCID: 0000-0001-7476-9734
E-mail: maxxkach@yandex.ru

Сведения об авторах

Валентина Борисовна Кульметьева – к.т.н., доцент кафедры механики композиционных материалов и конструкций (МКМК), Пермский национальный исследовательский политехнический университет (ПНИПУ).
ORCID: 0000-0002-5214-0932
E-mail: kulmetevavb@pstu.ru

Вячеслав Эдуардович Чувашов – аспирант кафедры МКМК, ПНИПУ.
ORCID: 0009-0000-0171-2024
E-mail: slavachuvashov@yandex.ru

Ксения Николаевна Лебедева – магистрант кафедры МКМК, ПНИПУ.
ORCID: 0009-0003-6134-2952
E-mail: lebedkseni@mail.ru

Светлана Евгеньевна Порозова – д.т.н., профессор кафедры МКМК, ПНИПУ.
ORCID: 0000-0001-5835-9727
E-mail: sw.porozova@yandex.ru

Максим Николаевич Каченюк – д.т.н., доцент кафедры МКМК, ПНИПУ
ORCID: 0000-0001-7476-9734
E-mail: maxxkach@yandex.ru

Contribution of the Authors

V. B. Kulmetyeva – conceptualization, goal setting, research objectives formulation, and thermal cycling of specimens.

V. E. Chuvashov – preparation of charge for spark plasma sintering, conducting high-temperature oxidation, data analysis, experimental results interpretation, of research result processing.

K. N. Lebedeva – analysis of experimental results, research results processing, article writing.

S. E. Porozova – scientific supervision, research results processing, text preparation and editing.
M. N. Kachenyuk – conducting spark plasma sintering.

Вклад авторов

В. Б. Кульметьева – постановка цели и задач исследования, формирование основной концепции, проведение термоциклирования образцов.
В. Э. Чувашов – подготовка шихты для проведения искрового плазменного спекания, подготовка и проведение высокотемпературного окисления, проведение расчетов, анализ полученных результатов экспериментов, обработка результатов исследований.
К. Н. Лебедева – анализ полученных результатов экспериментов, обработка результатов исследований, подготовка текста статьи.
С. Е. Порозова – научное руководство, обработка результатов исследований, подготовка и корректировка текста статьи.
М. Н. Каченюк – проведение искрового плазменного спекания.

Received 22.06.2022
Revised 11.11.2022
Accepted 19.12.2022

Статья поступила 22.06.2022 г.
Доработана 11.11.2022 г.
Принята к публикации 19.12.2022 г.

Porous Materials and Biomaterials
Пористые материалы и биоматериалы

UDC 621.452.322:678.073

https://doi.org/10.17073/1997-308X-2023-3-38-46

Research article
Научная статья

Calculating the penetration depth of reaction in chemical gas-phase deposition of boron nitride within porous bodies

A. N. Timofeev[1], A. S. Razina[1] ✉, P. A. Timofeev[1], A. G. Bodyan[2]

[1] **JSC "Kompozit"**
4 Pionerskaya Str., Korolyov, Moscow region 141070, Russia
[2] **Leonov University of Technology**
42 Gagarina Str., Korolyov, Moscow region 141070, Russia

✉ as.razina@gmail.com

Abstract. The thermodynamic calculations conducted using the TERRA software package for the B–Cl–N–H system revealed that the inclusion of hydrogen into the B–Cl system significantly diminishes the thermodynamic stability of BCl_3 with the possibility of boron formation in the condensed phase. On the other hand, the introduction of ammonia, which includes hydrogen, results in the synthesis of boron nitride across a broad temperature spectrum. The analysis of kinetic relationships uncovered three distinct regions in the boron nitride deposition process: K – kinetic region (up to 1400 K), D – diffusion region (above 1800 K) and T – transition region. The activation energy for the kinetic region was calculated as $E_a = 134$ kJ/mol. Within the temperature range of 1023–1123 K, linear dependences were observed. The computation of the penetration depth for the boron nitride deposition process assumed a gas mixture of boron trichloride, ammonia, and argon ($BCl_3 + NH_3 + 30Ar$). The results indicated that boron trichloride governs the extent of penetration. The depths of penetration for the chemical vapor infiltration boron nitride (CVI-BN) process, conducted at 0.1 kPa within the temperature range of 1100–1400 K, were determined for pore diameters of 1, 10, 30, 100, 200 and 300 μm. When porosimetry data for a specific preform is available, the acquired penetration depth relationships for the CVI-BN process under specific parameters and process temperatures facilitate the estimation of essential parameters for interphase formation using pyrolytic boron nitride.

Keywords: pyrolytic boron nitride (PBN), interphase coating, thermodynamic calculation, chemical vapor infiltration boron nitride (CVI-BN)

For citation: Timofeev A.N. , Razina A.S., Timofeev P.A., Bodyan A.G. Calculating the penetration depth of reaction in chemical gas-phase deposition of boron nitride within porous bodies. *Powder Metallurgy and Functional Coatings*. 2023;17(3):38–46. https://doi.org/10.17073/1997-308X-2023-3-38-46

Расчет глубины проникновения реакции при химическом газофазном осаждении нитрида бора в пористых телах

А. Н. Тимофеев[1], А. С. Разина[1] ✉, П. А. Тимофеев[1], А. Г. Бодян[2]

[1] **АО «Композит»**
Россия, 141070, Московская обл., г. Королев, ул. Пионерская, 4
[2] **Технологический университет им. А.А. Леонова (МГОТУ)**
Россия, 141070, Московская обл. г. Королев, ул. Гагарина, 42

✉ as.razina@gmail.com

Аннотация. Проведенные с помощью программного комплекса «TERRA» термодинамические расчеты системы B–Cl–N–H показали, что введение водорода в систему B–Cl резко снижает термодинамическую устойчивость BCl_3 с возможностью образования бора в конденсированной фазе, а добавка аммика, который содержит водород, приводит к образованию нитрида бора в широком интервале температур. Анализ кинетических зависимостей показывает наличие трех областей процесса осаждения нитрида бора: К – кинетическая область (от 1400 К и ниже), Д – диффузионная область (от 1800 К и выше) и П – переходная область. Для кинетической области определена энергия активации процесса E_a = 134 кДж/моль. В диапазоне температур 1023–1123 К получены линейные зависимости. Для расчетов глубины проникновения процесса осаждения нитрида бора в пористое тело было принято, что газовая смесь состоит из трихлорида бора, аммиака и аргона ($BCl_3 + NH_3 + 30Ar$). Результаты расчетов показали, что реагентом, лимитирующим глубину проникновения, является трихлорид бора. Были определены глубины проникновения процесса химического осаждения нитрида бора из газовой фазы (CVI-BN – *chemical vapor infiltration boron nitride*) при давлении 0,1 кПа в температурном интервале 1100–1400 К при диаметрах пор 1, 10, 30, 100, 200 и 300 мкм. При наличии результатов порометрии конкретной преформы полученные зависимости глубины проникновения процесса CVI-BN в пористое тело от температуры при определенных условиях позволяют оценить необходимые параметры процессов формирования интерфазы из пиролитического нитрида бора.

Ключевые слова: пиролитический нитрид бора (ПНБ), интерфазное покрытие, термодинамический расчет, химическое осаждение нитрида бора из газовой фазы

Для цитирования: Тимофеев А.Н., Разина А.С., Тимофеев П.А., Бодян А.Г. Расчет глубины проникновения реакции при химическом газофазном осаждении нитрида бора в пористых телах. *Известия вузов. Порошковая металлургия и функциональные покрытия*. 2023;17(3):38–46. https://doi.org/10.17073/1997-308X-2023-3-38-46

Introduction

Interest in pyrolytic boron nitride (PBN), which boasts a range of exceptional properties (high dielectric properties, chemical resistance in aggressive gases, liquids, and metal melts, heat resistance, low microwave energy absorption coefficient), remains unabated to this day [1–5]. Due amalgamation of these favorable attributes and their endurance at elevated temperatures and in deep vacuum conditions, this material has found extensive utility in electronics, electrical engineering, nuclear power engineering, the semiconductor industry, high-temperature technology, and the fabrication of containers and protective screens for synthesizing ultra-pure compounds.

At the turn of the century, with the advancement of silicon carbide fibers and materials derived from them, PBN began to serve as an interphase between fibers and matrices, imparting robust mechanical properties to SiC_f/SiC_m composite material [6–10]. The evolution of ceramic fibers encompassing diverse compositions (Si_3N_4, AlN, BN, etc.) and the composites founded upon them will further solidify the demand for PBN, functioning both as an interphase and matrix.

Simultaneously, it's imperative to acknowledge that the parameters for establishing the interphase on fibers or the matrix of composite materials via the chemical vapor infiltration (CVI) technique within a porous structure are fundamentally influenced by the preform's porous structure (pore size, tortuosity, etc.). In contemporary contexts, diverse reinforcement schemes and techniques for fabricating fiber preforms are employed in structures [11–13], each delineating a unique porous structure. This accentuates the necessity to tailor CVI process parameters according to the specifics of each structure.

This paper presents an analysis of the admissible parameter regions for the boron nitride deposition process via the CVI method, taking into account varied pore sizes and thicknesses of porous bodies.

Thermodynamic analysis of the B–Cl–N–H system

In order to determine the acceptable parameters ranges for the chemical deposition of boron nitride from the gas phase (temperature (T), pressure (P), and the ratio of initial reagents in the gas mixture), the TERRA software package (Russia, Moscow, Bauman Moscow State Technical University), was employed for thermodynamic analysis of the B–Cl–N–H system.

In the initial stage, equilibrium compositions of the B–Cl, N–H, B–Cl–N, and B–Cl–H systems were scrutinized to approximate the initial temperatures of boron trichloride and ammonia disproportionation. The impact of hydrogen and nitrogen on this process under varying pressures within the system was also evaluated. The analysis, illustrated in Figure 1, *a*, indicates that at $P = 10$ kPa, BCl_3 remains stable up to $T = 1800$ K. Beyond this threshold, the process of disproportionation into boron dichloride and monochloride is initiated. In the N–H system, where ammonia is a key component, its decomposition into nitrogen and hydrogen is nearly complete at $T = 600$ K and $P = 10$ kPa (Figure 1, *b*).

The introduction of nitrogen into the B–Cl system does not lead to the formation of boron nitride and does not significantly impact the thermodynamic stability of boron trichloride (Figure 1, *c*). However, the inclusion of hydrogen in the B–Cl system markedly diminishes the thermodynamic stability of BCl_3 (Figure 1, *d*). This situation introduces the potential for boron to form in the condensed phase, with its proportion increasing alongside higher hydrogen content in the mixture. The analysis also indicates that decreasing pressure within the system decreases the thermodynamic stability of boron trichloride and ammonia.

The introduction of ammonia, which contains hydrogen, into the B–Cl system reduces the thermodynamic stability of boron chlorides and leads to the formation of boron nitride across a wide temperature range.

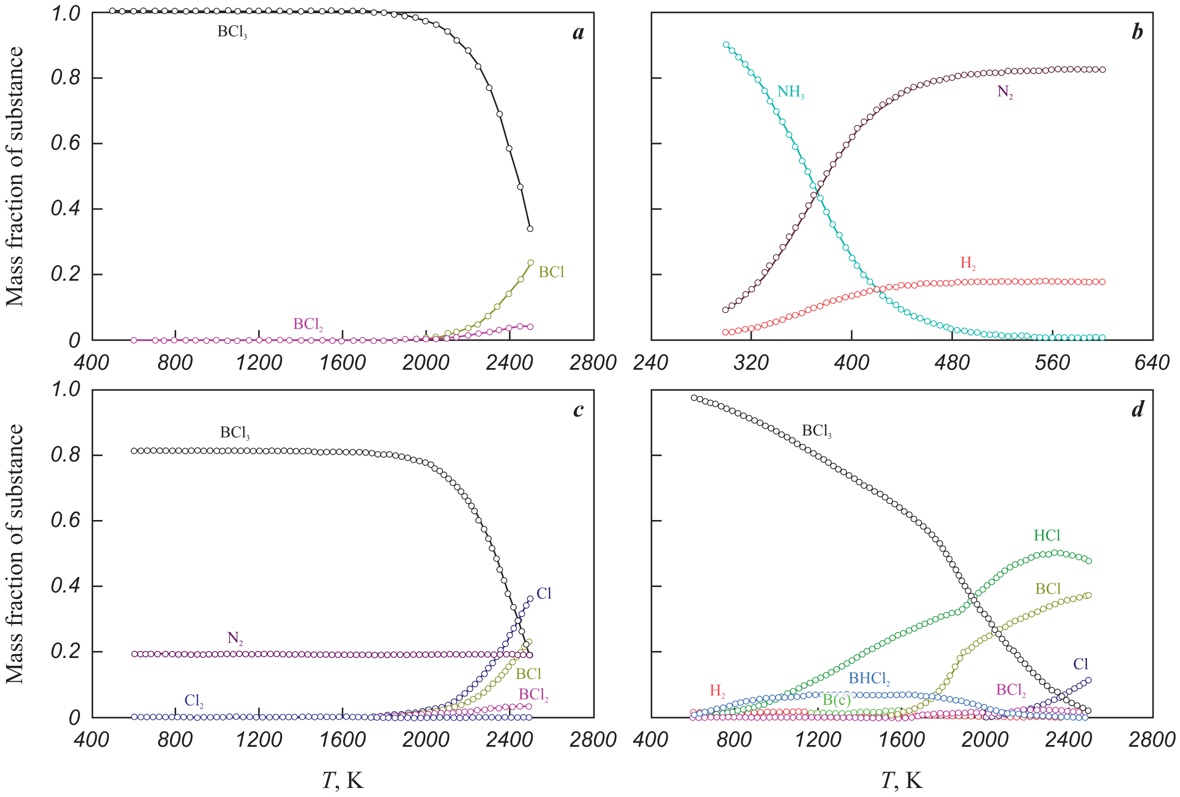

Fig. 1. Equilibrium composition of systems at 10 kPa pressure
a – B–Cl system formed by the BCl_3 gas mixture; ***b*** – B–N formed by NH_3;
c – B–Cl–N formed by $BCl_3 + N_2$; ***d*** – B–Cl–H formed by $BCl_3 + H_2$

Рис. 1. Равновесный состав систем при давлении 10 кПа
a – система B–Cl, образованная газовой смесью BCl_3; ***b*** – B–N, образованная NH_3;
c – B–Cl–N, образованная $BCl_3 + N_2$; ***d*** – B–Cl–H, образованная $BCl_3 + H_2$

Figure 2 illustrates the analysis results, showcasing the relationship between the yield of condensed boron nitride in the B–Cl–N–H system and temperature at a pressure of 10 kPa, while varying the initial reagent ratios. The findings reveal (Figure 2, *a*) that when $BCl_3:NH_3:H_2 = 1:1:0$, the thermodynamic stability of boron trichloride is sustained nearly until 2200 K, but this doesn't yield the maximum output of boron nitride. The introduction of hydrogen into the $BCl_3 + NH_3$ gas mixture promotes an escalation in the extent of boron trichloride decomposition, subsequently enhancing the theoretical yield of boron nitride (Figure 2, *b*, *c*). However, elevating hydrogen concentration beyond the ratio of 1:5 ($BCl_3:NH_3:H_2 = 1:1:5$) does not yield further increases in boron nitride yield, as near-complete decomposition of boron trichloride is already achieved.

It's noteworthy that augmenting the hydrogen content within the system could be accomplished by increasing the amount of ammonia in the mixture. For instance, with the $BCl_3:NH_3 = 1:3$ (Figure 2, *d*), the theoretical yield of condensed-phase boron nitride becomes nearly equivalent to the situation where hydrogen is introduced into the system with a $BCl_3:NH_3:H_2 = 1:1:5$ (as shown in Figure 2, *b*).

Consequently, the thermodynamic analysis of the equilibrium composition within the B–Cl–N–H system, generated from the gas phase through the utilization of initial reagents BCl_3, NH_3 and H_2, facilitated the assessment of the admissible parameter range for the chemical deposition process of boron nitride. The acquired outcomes provided the foundation for constructing the experimental matrix for PBN) production.

Experimental procedure

The following reagents were employed to investigate the kinetic patterns of the PBN deposition process:

BCl_3 – grade A boron trichloride (TU1-00-07526811-23-92);

– NH_3 – ammonia (GOST 6221-90);

– Ar – high-purity argon (GOST 10157-79).

In order to explore the kinetic trends of PBN coating formation on impermeable substrates, we utilized samples crafted from C-3 grade graphite, manufactured by JSC "Karbotek" (Moscow, Russia), featuring pyrolytic carbon coating. For porous substrates, we employed preform (skeleton) samples generated through the hydrajet method from Keralan silicon carbide ceramic

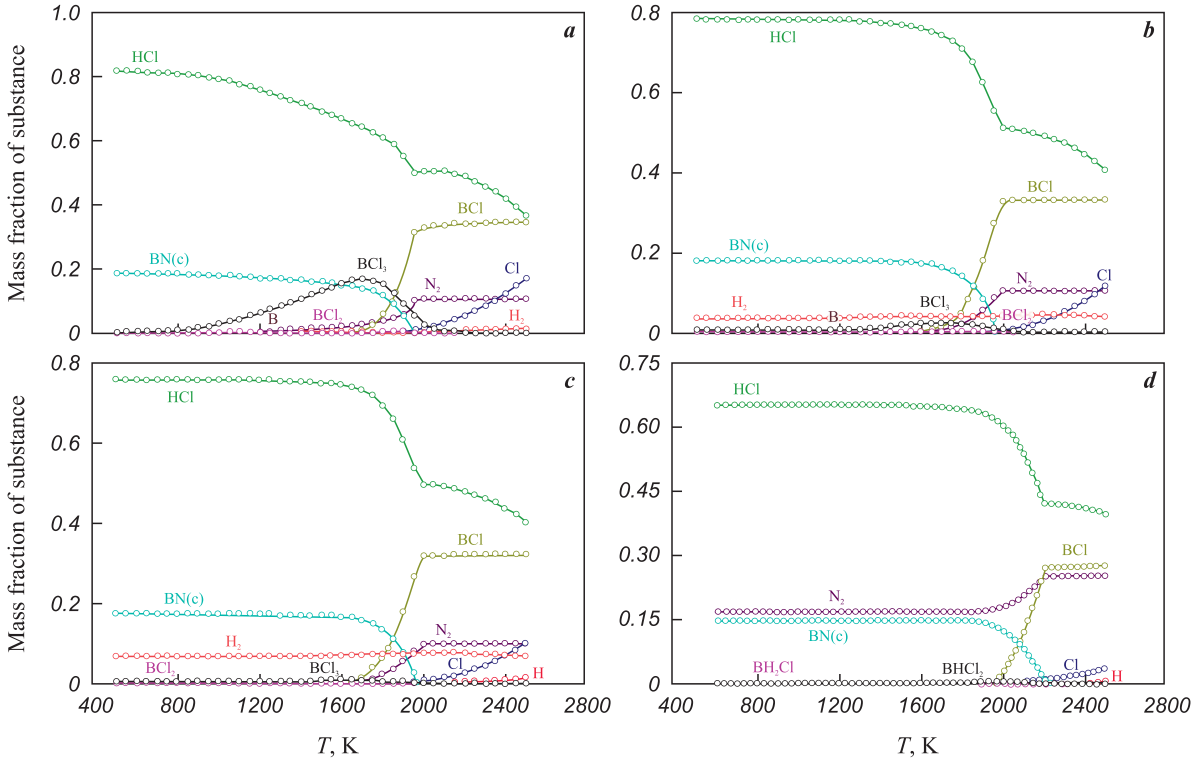

Fig. 2. Equilibrium composition in the B–Cl–N–H system at 10 kPa pressure, formed by gas mixtures $BCl_3 + NH_3$ (***a***), $BCl_3 + NH_3 + 5H_2$ (***b***), $BCl_3 + NH_3 + 10H_2$ (***c***) and $BCl_3 + 3NH_3$ (***d***)

Рис. 2. Равновесный состав в системе B–Cl–N–H при давлении 10 кПа, образованной газовыми смесями $BCl_3 + NH_3$ (***a***), $BCl_3 + NH_3 + 5H_2$ (***b***), $BCl_3 + NH_3 + 10H_2$ (***c***) и $BCl_3 + 3NH_3$ (***d***)

filament (TU 20.60.13-952-56897835-2022), produced by JSC "Kompozit" [14].

The porosity of the preform was evaluated using reference porosimetry via the reference contact porometer Porotech 3.2 at the Leonov University of Technology (Korolyov, Moscow Region, Russia).

Deposition of pyrolytic boron nitride was conducted using the BN 2.0 plant (Leonov University of Technology). The presence of the interphase BN coating and its thickness on framework fibers were assessed via scanning electron microscopy (SEM) utilizing a JSM-6610 LV device (JEOL, Japan).

The phase composition of PNB was ascertained using an *X*-ray diffractometer EMRYREAn (PANalytical, the Netherlands).

Results and discussion

The chosen parameters for the chemical vapor deposition (CVD) process were based on thermodynamic analysis:

$P = 0.1$ kPa for the temperature range of 1023–1123 K at a ratio of reagents of $BCl_3{:}NH_3 = 1{:}1$;

$P = 0.2$ kPa for $T = 2023{\div}2123$ K at $BCl_3{:}NH_3 = 1{:}3$.

In both cases, argon was employed as the carrier gas for boron trichloride.

Since the commencement temperatures for the decomposition of ammonia and boron trichloride are notably disparate (as seen in Figure 1, *a*, *b*), it is prudent to separately introduce them into the reaction zone to prevent premature interaction. This was accomplished in the BN 2.0 plant through a coaxial tube.

Figure 3 depicts the dependency of the boron nitride coating deposition rate constant on temperature, as obtained from [3] (where hydrogen was employed as the carrier gas), alongside the results derived by the authors of this paper. Thermodynamic analysis revealed that within the low-temperature range (1000–1200 K), the theoretical yield of condensed-phase boron nitride in the is relatively consistent for a $BCl_3{:}NH_3$ mixture ratio of 1:1, both with and without hydrogen. Meanwhile, within the high-temperature range, the introduction of hydrogen into the mixture or an increase in ammonia content amplifies the theoretical yield of condensed-phase boron nitride. Similar conclusions were reached in experimental studies conducted by [15–19].

The analysis of kinetic dependences acquired from [3] uncovers the existence of three process regions in boron nitride deposition:

K – kinetic region (1400 K and below);

D – diffusion region (1800 K and above);

T – transient region.

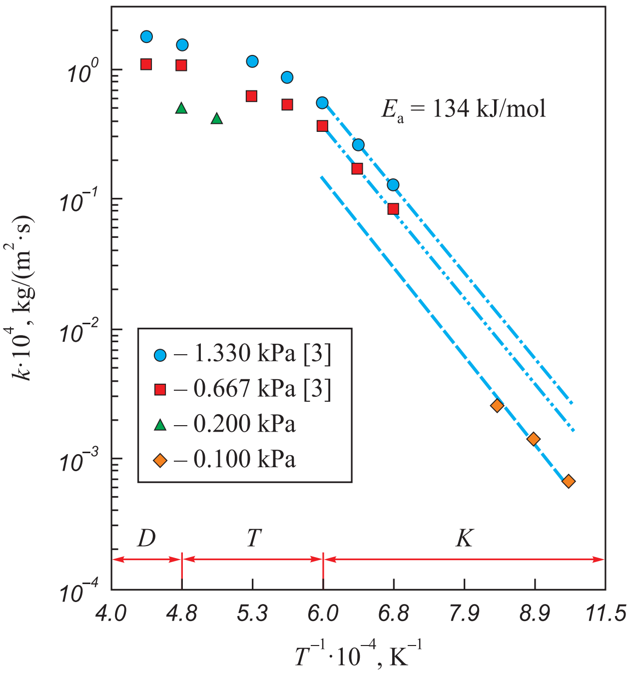

Fig. 3. Dependence of the deposition rate constant of a pyrolytic boron nitride coating on temperature

Рис. 3. Зависимость константы скорости осаждения покрытия из пиролитического нитрида бора от температуры

In the kinetic region, the activation energy of the process was determined to be $E_a = 134$ kJ/mol. In the temperature range of 1023–1123 K, linear dependences were also observed. Their similarity to the dependencies obtained in [3] suggests a comparable activation energy, despite the variations in process pressure. This could be attributed to the fact that within the considered pressure range of 0.1÷0.2 kPa, the deposition rate's correlation with pressure and, consequently, reagent concentration in the kinetic region is not pronounced. As a result, the process rate is dictated by the reaction rate, whose mechanism remains consistent between the conditions outlined by the authors in [3] and our study.

In the future, as we refine the results, adjustments might be made to the analysis of the activation energy. In that case, for the kinetic region, the boron nitride deposition rate constant (k, kg/(m^2·s)) at a pressure of 0.1 kPa, using a reaction mixture of $BCl_3 + NH_3$ in a 1:1 ratio, can be expressed as follows:

$$k = 0.24\exp\left(-\frac{134{,}000}{RT}\right), \tag{1}$$

where R is the universal gas constant, J/(mol·K); T is the temperature of the PBN deposition process, K.

It is worth noting that the density of PBN obtained within the temperature range of $T = 1023 \div 1123$ K is approximately $1.4 \cdot 10^3$ kg/m^3, while for the temperature range of 2023–2123 K, it is on the order of $2.0 \cdot 10^3$ kg/m^3. Drawing from the findings of [3], we can hypothesize that the dependence expressed by equation (1) remains valid up to at least 1400 K, with possible deviations linked to changes in PBN density.

Determining the kinetic region stands as a pivotal stride, enabling the progression to the modeling of the PBN deposition process on the surface of a porous preform's pores. The central objective in investigating the kinetics of PBN deposition within a porous preform is to ascertain the depth of the coating formation reaction's penetration on the pore surface. This, in turn, facilitates estimating the maximal thickness of the preform – a volume within which PBN will precipitate onto the pore surface. To achieve this estimation, the computational-theoretical model outlined in [20] can be effectively utilized. It can be expressed as follows, taking the form of a first-order reaction equation:

$$L_{\max} \approx \left[\frac{\lambda d\sqrt{\dfrac{RT}{3M}\left[1-\exp\left(-\dfrac{d}{\lambda}\right)\right]}}{4X^3k}\right]^{1/2}, \tag{2}$$

where $L_{\max}$ is the depth of the reaction's penetration into the porous preform, m; λ is the free path length of a gas molecule, m; d is the pore diameter, m; M is the mass of a gas molecule, kg; k is the rate constant of the heterogeneous reaction on the surface, kg/(m^2·s); X is the tortuosity coefficient, kg/m^3.

For a gas phase composed of a mixture of molecules from various substances 1, 2, 3 ..., the path length is equal to [19]

$$\lambda_1 = KT\left[\pi\left(N_1\sigma_1^2\sqrt{2} + N_2\sigma_2^2\sqrt{1+\frac{M_1}{M_2}} + \right.\right.$$
$$\left.\left. + N_3\sigma_3^2\sqrt{1+\frac{M_1}{M_2}} + \ldots\right)\rho\right]^{-1}, \tag{3}$$

where N is the mole fraction; K is the Boltzmann constant, J/K; σ is the molecule diameter, m; P is the pressure within the system, Pa; ρ is the density of the gas phase, g/cm^3.

For the analysis, it was considered that the gas mixture comprises $BCl_3 + NH_3 + 30Ar$ composition, wherein boron trichloride and ammonia are determined via thermodynamic analysis, and argon is employed as a diluent gas. In order to mitigate random errors arising from using molecule diameter (σ) values from disparate sources, a standardized calculation procedure was implemented employing the formula

$$\sigma = 1.329 \cdot 10^{-8}\left(\frac{M}{\rho}\right)^{1/3}, \tag{4}$$

where ρ is the density of the condensed phase, kg/m^3 ($\rho_{BCl_3} = 1.345 \cdot 10^3$ kg/m^3 [21]).

As a result, the following values were obtained: $\sigma_{BCl_3} = 5.89 \cdot 10^{-10}$ m; $\sigma_{NH_3} = 3.88 \cdot 10^{-10}$ m; $\sigma_{Ar} = 4.15 \cdot 10^{-10}$ m and $\lambda_{BCl_3} = 9.05 \cdot 10^{-6}\, T/P$ m; $\lambda_{NH_3} = 21.5 \cdot 10^{-6}\, T/P$ m.

The tortuosity coefficient for woven and needle-punched frameworks with a density of (0.4–0.5)·10^3 kg/m^3 was approximated to be 1.3 [22].

The analysis revealed that the limiting reagent dictating the extent of penetration of the PBN deposition reaction into the porous body L_{max} is boron trichloride. Figure 4 depicts the calculated relationships of the depth of PBN deposition penetration onto pores of varying diameters within the temperature range of 1100–1400 K, at a pressure of 0.1 kPa.

The pore diameter in preforms of ceramic matrix composite materials is contingent on the reinforcement schemes and potential subsequent process stages aimed at obtaining porous blanks. Thus, within the pore space of 3D and 4D structural reinforcing frameworks, distinct types of porosity emerge: inter-strand (inter-rod) and inter-filament. In the former scenario, the dimension of inter-strand (inter-rod) pores is determined by the diameter of the strand (rod). For instance, in a 4D framework crafted from rods of 0.7 mm diameter, the inter-rod pore diameter measures 135.45 μm [22].

In preforms showcasing a 2.5D structure anchored on UT-900P carbon fabric interwoven with Ural-NSh24 carbon thread, three categories of pores have been discerned [22]:

1) pores in the range of up to 0.8 μm in diameter originated from fiber imperfections and resin coke and pyrocarbon porosity;

2) the set of pores sized between 0.8÷3.6 μm primarily arises from inter-filament pores;

3) the assortment of pores encompasses both inter-strand pores ($d = 3.6$ to 36.0 μm) and interlayer pores ($d > 36.0$ μm).

In a similar preform, albeit fashioned from Ural-TM/4 carbon fabric coupled with Ural-NSh24 carbon thread, the prevalent pores possess radii of 0.1÷1.0 μm (coke pores and inter-filament pores), and 1–10 μm (inter-filament (inter-strand) pores). Pores with a radius less than 0.1 μm or exceeding 10 μm are less abundant in the material. Discrepancies in the porous structure's characteristics are ascribed to the distinct properties of Ural-TM/4 and UT-900P fabrics. Furthermore, the filament diameter, strand diameter, and framework density exert an impact on the pore size.

In [14], three primary observable pore sizes that contribute to the overall porous structure were identified for the nonwoven framework crafted from Siqulox silicon carbide fibers (JSC "GNIIChTEOS", RF): 15, 40 and 250 μm. Similar findings were also obtained for frameworks relying on Keralan carbide-silicon fibers (JSC "Komposit", RF) [14].

Utilizing the outcomes of these computations, the PBN deposition mode at $T = 1100÷1400$ K and $P = 0.1$ kPa into the nonwoven framework founded on Keralan carbide-silicon fibers was subjected to testing. Figure 5 illustrates the microstructure of the acquired sample, showcasing the silicon carbide framework with a PBN interphase coating.

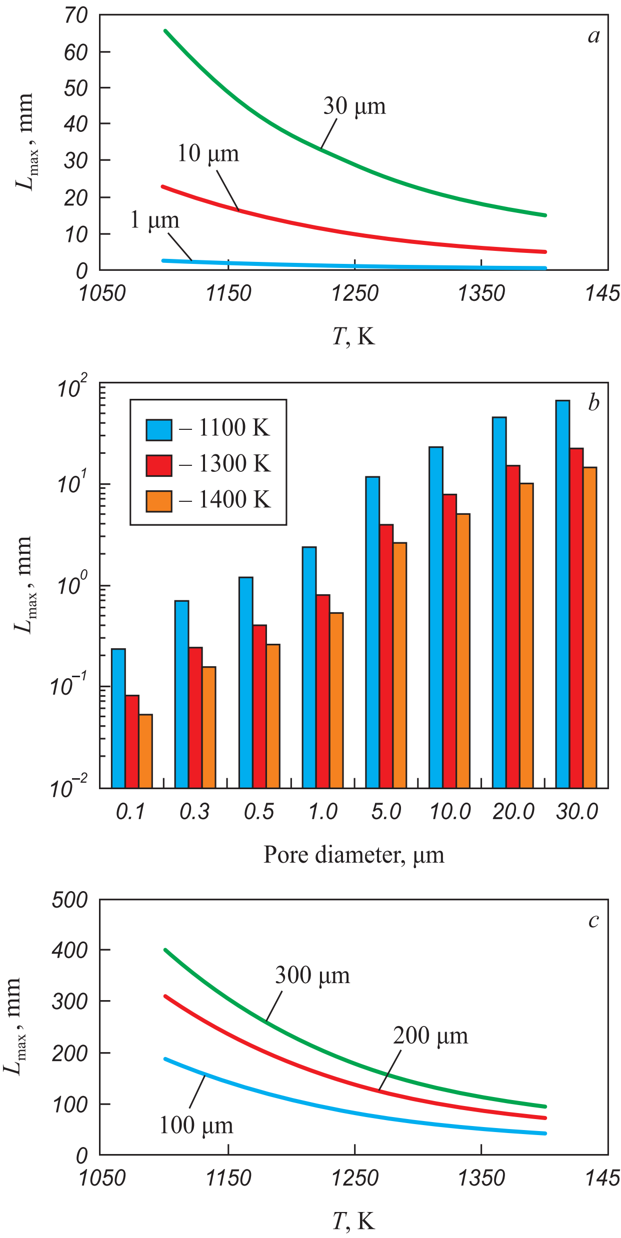

Fig. 4. Penetration depth of the CVI-BN reaction at $P = 0.1$ kPa into a porous body at $T = 1100–1400$ K (***a***), 1100, 1300 and 1400 K (***b***) and 1100–1400 K (***c***)
The numbers next to the curves are the pore diameter

Рис. 4. Глубина проникновения реакции CVI-BN при $P = 0{,}1$ кПа в пористое тело при $T = 1100÷1400$ K (***a***), 1100, 1300 и 1400 K (***b***) и 1100–1400 K (***c***)
Цифры у кривых – диаметр пор

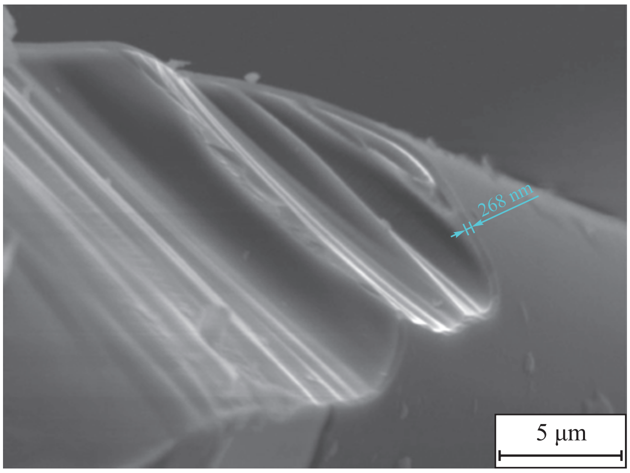

Fig. 5. Formation of a pyrolytic boron nitride interphase coating with a thickness of ≈250 nm on Keralan silicon carbide fiber

Рис. 5. Внешний вид интерфазного покрытия пиролитического нитрида бора толщиной ≈250 нм на карбидокремниевом волокне Кералан

The findings from determining the phase composition of the fiber sample reveal the existence of a hexagonal modification (*P6mc*) on the surface of PBN carbide-silicon fibers. This hexagonal modification possesses a low shear strength within its fundamental plane, which is crucial for facilitating the functionality of the interphase coating [8].

Conclusion

Hence, the outcomes of porosimetry conducted on specific preforms and the established relationships depicting the penetration depth of the CVI-BN process under specific conditions within the porous structure provide us with the means to estimate the essential parameters for crafting interphases using PBN and creating composites with a matrix composed of PBN.

References / Список литературы

1. Avarbe R.G., Shpak V.S. Refractory compounds – deposition from the gas phase. In: *Khimicheskoe gazofaznoe osazhdenie tugoplavkikh neorganicheskikh materialov*. Leningrad: GIPkH, 1976. Vol. 78. P. 97–103. URL: https://search.rsl.ru/ru/record/01006955797 (Accessed: 10.04.2023). (In Russ.).

Аварбэ Р.Г., Шпак В.С. Тугоплавкие соединения – осаждение из газовой фазы. В сб.: *Химическое газофазное осаждение тугоплавких неорганических материалов*. Л.: ГИПХ, 1976. Т. 78. С. 97–103. URL: https://search.rsl.ru/ru/record/01006955797 (Дата обращения: 10.04.2023).

2. Donetskiy K.I., Raskutin A.E., Hilov P.A., Lykianenko Yu.V., Belinis P.G., Korotigin A.A. Branding and woven textile preformes for the manufacturing fiber reinforced plastics (review). *Trudy VIAM*. 2015;(9):80–85. (In Russ.). http://dx.doi.org/10.18577/2307-6046-2015-0-9-10-10

Донецкий К.И., Раскутин А.Е., Хилов П.А., Лукьяненко Ю.В., Белинис П.Г., Коротыгин А.А. Объемные текстильные преформы, используемые при изготовлении полимерных композиционных материалов (обзор). *Труды ВИАМ*. 2015;(9):80–85. http://dx.doi.org/10.18577/2307-6046-2015-0-9-10-10

3. Morachevskii A.G., Sladkov I.B. Physical and chemical properties of molecular inorganic compounds (Experimental data and calculation methods). Saint Petersburg: Khimiya, 1987. 312 p. (In Russ.).

Мораческий А.Г., Сладков И.Б. Физико-химические свойства молекулярных неорганических соединений (Экспериментальные данные и методы расчета). СПб: Химия, 1987. 312 с.

4. Belova S.V. Porous permeable materials. Moscow: Metallurgiya, 1987. 335 p. (In Russ.).

Белова С.В. Пористые проницаемые материалы. М.: Металлургия, 1987. 335 с.

5. Lubina J. Handbook of composite materials. Moscow: Mashinosroenie, 1988. 448 p. (In Russ.).

Любина Дж. Справочник по композиционным материалам. М.: Машиностроение, 1988. 448 с.

6. Bulanov I.M., Vorobey V.V. Technology of rocket and aerospace structures from composite materials. Moscow: Izdatelstvo MGTU im. N.E. Baumana, 1998. 513 p. (In Russ.).

Буланов И.М., Воробей В.В. Технология ракетных и аэрокосмических конструкций из композиционных материалов. М.: Изд-во МГТУ им. Н. Э. Баумана, 1998. 513 с.

7. Eliseev Yu.S., Krymov V.V., Kolesnikov S.A., Vasiliev Yu.N. Non-metallic composite materials in structural elements and production of aircraft gas turbine engines: Proc. allowance for universities. Moscow: Izdatelstvo MGTU im. N.E. Baumana, 2007. 368 p. (In Russ.).

Елисеев Ю.С., Крымов В.В., Колесников С.А., Васильев Ю.Н. Неметаллические композиционные материалы в элементах конструкций и производстве авиационных газотурбинных двигателей: Учеб. пособие для вузов. М.: Изд-во МГТУ им. Н.Э. Баумана, 2007. 368 с.

8. Evans A.G., Marshall D.B. Overview no. 85 The mechanical behavior of ceramic matrix composites. *Acta Metallurgica*. 1989;37(10):2575–2583. https://doi.org/10.1016/0001-6160(89)90291-5

9. Toshitsugu M., Hiroyuki N., Toshio H. Density and deposition rate of chemical-vapour-deposited boron nitride. *Journal of Materials Science*. 1988;23(2):509–514. https://doi.org/10.1007/BF01174677

10. Moore A.W. Characterization of pyrolytic boron nitride for semiconductor materials processing. *Journal of Crystal Growth*. 1990;106(1):6–15. https://doi.org/10.1016/0022-0248(90)90281-O

11. Rozenberg A.S., Sinenko Yu.A., Chukanov N.V. Regularities of pyrolytic boron nitride coating formation on a graphite matrix. *Journal of Materials Science*.

1993;28(20):5528–5533.
https://doi.org/10.1007/BF00367825

12. Kerans R.J., Hay R.S., Parthasarathy T.A., Cinibulk M.K. Interface design for oxidation-resistant ceramic composites. *Journal of the American Ceramic Society*. 2002;85(11):2599–2632.
http://dx.doi.org/10.1111/j.1151-2916.2002.tb00505.x

13. Razina A.S., Timofeev A.N., Kolomiytsev I.A., Timofeev P.A., Bodyan A.G. Some technological foundations for the formation of a composite material SiC_f/SiC_m with an interphase of boron nitride. *Voprosy oboronnoi tekhniki. Kompozicionnye i nemetallicheskie materialy v mashinostroenii*. 2021;201(2):50–56. (In Russ).

Разина А.С., Тимофеев А.Н., Коломийцев И.А., Тимофеев П.А., Бодян А.Г. Некоторые технологические основы формирования композиционного материала SiC_f/SiC_m с интерфазой из нитрида бора. *Вопросы оборонной техники. Композиционные и неметаллические материалы в машиностроении*. 2021;201(2):50–56.

14. Suzuki M., Tanaka Y., Inoue Y., Miyamoto N., Sato M., Goda K. Uniformization of boron nitride coating thickness by continuous chemical vapor deposition process for interphase of SiC/SiC composites. *Journal of the Ceramic Society of Japan*. 2003;111(12):865–871.
https://doi.org/10.2109/jcersj.111.865

15. Udayakumara A., Sri Ganesh A., Raja S., Balasubramanian M. Effect of intermediate heat treatment on mechanical properties of SiC_f/SiC composites with BN interphase prepared by ICVI. *Journal of the European Ceramic Society.* 2011;31(6):1145–1153.
https://doi.org/10.1016/j.jeurceramsoc.2010.12.018

16. Fuhai L., Maozhoong Y., Liping R., Yicchend G., Zhe Zh., Ke P. Effects of *h*-BN/SiC ratios on oxidation mechanism and kinetics of C/C–BN–SiC composites. *Journal of the Europen Ceramic Society*. 2022;42(1):52–70.
http://dx.doi.org/10.1016/j.jeurceramsoc.2021.09.029

17. Krenkel W. (ed.). Ceramic matrix compositeis: Fiber reinforced ceramics and their applications. 2008. 440 p. https://doi.org/10.1002/9783527622412

18. Bogomolov P.I., Kozlov I.A., Birulya M.A. A review of modern technologies of manufacturing of three-dimensional preforms for advanced composite materials. *Tekhniko-tekhnologicheskie problemy servisa*. 2017;1(39): 22–27. (In Russ.).

Богомолов П.И., Козлов И.А., Бируля М.А. Обзор современных технологий изготовления объемно-армирующих преформ для перспективных композиционных материалов. *Технико-технологические проблемы сервиса*. 2017;1(39):22–27.

19. Timofeev A.N. Calculation and theoretical estimation of penetration depth of chemical gas-phase deposition of pyrolytic matrices in porous bodies. *Izvestiya vuzov. Poroshkovaya metallurgiya i funkcional'nye pokrytiya*. 2012;(3):40–45. (In Russ.).

Тимофеев А.Н. Расчетно-теоретическая оценка глубин проникновения реакций по осаждению пиролитических матриц в пористых каркасах. *Известия вузов. Порошковая металлургия и функциональные покрытия*. 2012;(3):40–45.

20. Bretschneider S. Properties of gases and liquids. Moscow, Leningrad: Khimiya, 1966. 535 p. (In Russ.).

Бретшнайдер С. Свойства газов и жидкостей. М., Л.: Химия, 1966. 535 с.

21. Dashman S. Scientific foundations of vacuum technology. Moscow: Mir, 1964. 715 p. (In Russ.).

Дэшман С. Научные основы вакуумной техники. М.: Мир, 1964. 715 с.

22. Timofeev I.A. Development of technological bases for the formation of an oxidation-resistant matrix of a composite material by chemical deposition from the gas phase Si–C–N–H: Dis. Cand. Sci. (Eng.). Moscow: MSTU im. N.E. Baumana, 2010. (In Russ.).

Тимофеев И.А. Разработка технологических основ формирования окислительно-стойкой матрицы композиционного материала методом химического осаждения из газовой фазы Si–C–N–H: Дис. к.т.н. М.: МГТУ им. Н.Э. Баумана, 2010.

Information about the Authors

Anatoliy N. Timofeev – Dr. Sci. (Eng.), Deputy General Director for Research, JSC "Kompozit".
ORCID: 0000-0003-3862-5295
E-mail: a_timofeev@mail.ru

Anna S. Razina – Group Leader, JSC "Kompozit".
ORCID: 0000-0003-1205-4121
E-mail: as.razina@gmail.com

Pavel A. Timofeev – Cand. Sci. (Eng.), Head of Department, JSC "Kompozit".
ORCID: 0000-0001-7448-8086
E-mail: pa.timofeev@gmail.com

Aleksandr G. Bodyan – Junior Researcher, Department of Engineering and Technology, Leonov University of Technology.
ORCID: 0000-0001-5203-9300
E-mail: sany193@gmail.com

Сведения об авторах

Анатолий Николаевич Тимофеев – д.т.н., зам. ген. директора по научной работе, АО «Композит».
ORCID: 0000-0003-3862-5295
E-mail: a_timofeev@mail.ru

Анна Сергеевна Разина – начальник группы АО «Композит».
ORCID: 0000-0003-1205-4121
E-mail: as.razina@gmail.com

Павел Анатольевич Тимофеев – к.т.н., начальник отдела АО «Композит».
ORCID: 0000-0001-7448-8086
E-mail: pa.timofeev@gmail.com

Александр Григорьевич Бодян – мл. науч. сотрудник кафедры техники и технологии, Технологический университет им. А.А. Леонова (МГОТУ).
ORCID: 0000-0001-5203-9300
E-mail: sany193@gmail.com

Contribution of the Authors

A. N. Timofeev – problem statement, development of the article's concept, critical literature analysis, text preparation, compilation of study conclusions.

A. S. Razina – statistical data processing, calculations implementation, tabular and graphical result presentation, results description.

P. A. Timofeev – thermodynamic calculations, text editing, conclusions correction.

A. G. Bodyan – experiment preparation, experiment execution, statistical data collection.

Вклад авторов

А. Н. Тимофеев – постановка задачи, разработка концепции статьи, критический анализ литературы, подготовка текста, формирование выводов исследования.

А. С. Разина – обработка статистических данных, осуществление расчетов, табличное и графическое представления результатов, описание результатов.

П. А. Тимофеев – проведение термодинамических расчетов, корректировка текста статьи, корректировка выводов.

А. Г. Бодян – подготовка эксперимента, проведение эксперимента, сбор статистических данных.

Received 05.05.2022
Revised 19.04.2023
Accepted 21.04.2023

Статья поступила 05.05.2022 г.
Доработана 19.04.2023 г.
Принята к публикации 21.04.2023 г.

Materials and coatings fabricated using the additive manufacturing technologies
Материалы и покрытия, получаемые методами аддитивных технологий

UDC 621.7; 669

https://doi.org/10.17073/1997-308X-2023-3-47-54

Research article
Научная статья

Trajectories of titanium powder particles of diffferent size in a plasma flow

R. A. Okulov[1, 2] ✉, **S. M. Akhmetshin**[1], **B. R. Gelchinsky**[1], **A. A. Rempel**[1]

[1] **Institute of Metallurgy of the Ural Branch of the Russian Academy of Sciences**
101 Amundsena Str., Yekaterinburg 620016, Russia
[2] **Ural Federal University named after the First President of Russia B.N. Yeltsin**
19 Mira Str., Yekaterinburg 620002, Russia

✉ okulov.roman@gmail.com

Abstract. The study focused on analyzing the trajectories of powder particles within a plasma flow, a process utilized for applying functional coatings and producing powders. An overview of contemporary scientific research dedicated to modeling these processes is presented. The primary objective of this study was to ascertain how the particle size of the powder, used as a raw material, influences the path of particles within a vertically directed plasma flow. We examined three sizes of titanium powder: 1 μm, 50 μm and 100 μm. These sizes were chosen based on production practices for the considered processes and the particle size distribution of the powder material used in full-scale experiments, employing specialized CAMSIZER-XT equipment. Our study reveals the significant impact of powder particle size on various parameters, including the opening angle, length, and width of the illuminated section of the plasma torch, as well as the distance traveled by particles entrained by the plasma flow from the plasma head. To investigate these effects, we conducted computer simulations, followed by validation through full-scale experiments for each case. Specifically, we employed the MAK-10 laboratory plasma facility at the Institute of Metallurgy, Ural Branch, Russian Academy of Sciences, which is designed for powder production and functional coatings. In order to ensure the reliability of our measurements, we performed statistical data processing of the full-scale experiment results using scatter plots and determination of their average values. The comparative analysis of results from both natural and computer experiments demonstrated a satisfactory level of convergence. This comparative analysis of three particle sizes of powder enabled us to formulate practical recommendations for enhancing equipment and process technology in the context of the considered procedures. Furthermore, our article introduces a computer model capable of predicting the dimensions of the reactor (the chamber for receiving powder materials), the optimal shape of components within the plasma facility, and the positioning of the substrate on which functional coatings are applied. This model can be applied to address similar problems within the scope of this study, facilitating the control of coating application processes and powder production.

Keywords: gravity force, particle trajectory, plasma method, powder production, coating application

Acknowledgements: This research received support from the Russian Science Foundation, project No. 21-43-00015.

For citation: Okulov R.A., Akhmetshin S.M., Gelchinsky B.R., Rempel A.A. Trajectories of titanium powder particles of diffferent size in a plasma flow. *Powder Metallurgy and Functional Coatings*. 2023;17(3):47–54. https://doi.org/10.17073/1997-308X-2023-3-47-54

Траектория движения частиц титанового порошка различной фракции в плазменном потоке

Р. А. Окулов[1, 2] ✉, **С. М. Ахметшин**[1], **Б. Р. Гельчинский**[1], **А. А. Ремпель**[1]

[1] **Институт металлургии Уральского отделения РАН**
Россия, 620016, г. Екатеринбург, ул. Амундсена, 101
[2] **Уральский федеральный университет имени первого Президента России Б.Н. Ельцина**
Россия, 620002, г. Екатеринбург, ул. Мира, 19

✉ okulov.roman@gmail.com

Аннотация. Исследованы траектории движения частиц порошка в плазменном потоке, который используется для процессов нанесения функциональных покрытий и получения порошков. Выполнен обзор современных научных исследований, посвященных моделированию рассматриваемых процессов. Цель работы заключалась в определении влияния размера частиц порошка, используемого в качестве сырья, на траекторию движения частиц в плазменном потоке, направленном вертикально вверх. Исследовали три фракции титанового порошка: 1, 50 и 100 мкм, выбранные исходя из производственной практики ведения рассмотренных процессов и результатов гранулометрического состава порошкового материала, использованного в натурном эксперименте, при помощи специализированного оборудования CAMSIZER-XT. В работе продемонстрированно, каким образом размер частиц порошка влияет на угол раскрытия, длину и ширину светящейся фракции плазменного факела, а также удаленность увлеченных плазменным потоком частиц от плазменной головки. Исследование выполнено с помощью компьютерного эксперимента с последующей верификацией путем проведения натурного эксперимента для каждого из рассматриваемых случаев. При этом использовалась лабораторная плазменная установка МАК-10 (ИМЕТ УрО РАН), применяемая для получения порошков и нанесения функциональных покрытий. С целью надежного получения итогов измерений была проведена статистическая обработка результатов натурного эксперимента методом точечных диаграмм размахов и определения их средних значений. Результаты сравнительного анализа итогов натурного и компьютерного экспериментов показали удовлетворительную сходимость. Сравнительный анализ применения трех фракций порошка позволил разработать практические рекомендации по совершенствованию оборудования и технологии ведения рассматриваемых процессов. В статье описана компьютерная модель, позволяющая прогнозировать размеры реактора (камеры приема порошкового материала), рациональную форму составных частей плазменной установки и положение подложки, на которую наносится функциональное покрытие. Представленную модель можно использовать для решения задач, подобных поставленной в рамках данного исследования, с целью управления процессами нанесения покрытий и получения порошка.

Ключевые слова: сила тяжести, траектория движения частиц, плазменный метод, получение порошков, нанесение покрытий

Благодарности: Работа выполнена при поддержке Российского научного фонда, проект № 21-43-00015.

Для цитирования: Окулов Р.А., Ахметшин С.М., Гельчинский Б.Р., Ремпель А.А. Траектория движения частиц титанового порошка различной фракции в плазменном потоке. *Известия вузов. Порошковая металлургия и функциональные покрытия*. 2023;17(3):47–54. https://doi.org/10.17073/1997-308X-2023-3-47-54

Introduction

Plasma sputtering presents an efficient method for acquiring functional coatings [1; 2]. By precisely managing plasma parameters and deposition conditions, it becomes feasible to achieve top-quality coatings [3]. Extensive research exists concerning the examination of how deposition process parameters impact the characteristics of the resultant functional coatings [4–6]. Additionally, plasma spraying serves as a technique for generating powders that find application in additive technologies [7–10].

The finite element method serves as a convenient and precise tool for predicting and elucidating the influence of various factors on both powder production and coating application processes. Computer simulations are in high demand, especially for the investigation of functional coatings composed of high-entropy alloys like GdTbDyHoSc and GdTbDyHoY [11]. studies related to coating deposition [12–14], software packages such as ANSYS, SolidWorks, and JmarPro were employed. For simulating the powder production processes using the plasma method, researchers utilized ANSYS [15], FLOW-3D [16] and COMSOL [17].

The trajectories of particles within a plasma flow significantly affects the characteristics of coatings and the properties of the resulting powders. Conversely, it is also influenced by the particle size of the raw powder material. Additionally, among the contributing factors, the shape of the internal channel, which is defined by the components of the plasma head and the operational features of the facility, plays a pivotal role. While there are publications that discuss the impact of factors like nozzle shape [18], operating modes [19], powder material introduction methods [20], interelectrode inserts [21] and gas swirler shapes [22], insufficient attention has been given to exploring the effect of powder particle size on particle motion trajectories within the plasma flow.

The primary objective of this study was to investigate how three particle sizes (1, 50 and 100 μm) of titanium powder, used as raw material, influence the trajectories of particles within a vertically directed plasma flow.

Experimental

A computer model of the plasma facility was developed to predict plasma flow parameters, employing the finite element method. The SolidWorks Flow Simulation software package (version 2016) served as a valuable tool for computational fluid dynamics (CFD). Subsequently, the results of the computer experiment underwent verification. In the numerical solution process, the Euler and Navier-Stokes equations were employed. In order to accurately represent surface, subsurface, and intermediate processes occurring within the flow, a finite element grid size of 0.24 mm was chosen. This grid size ensured that a minimum of 8 elements were positioned within the narrowest section of the three-dimensional computer model of the plasmatron, specifically, the plasma-forming gas inlet channel of the swirler with a diameter of 2 mm [23].

In order to carry out a computer experiment, a three-dimensional model was created based on the MAK-10 laboratory facility, which is located at the premises of IMET, Ural Branch, Russian Academy of Sciences. The design and parameters of this facility are depicted in Figure 1.

The initial data for the computer experiment are as follows:

- plasma forming gas flow rate: 20 l/min;
- gas type: argon;
- gas pressure in the supplying system: 2 atm;
- diameter of the central hole of swirlers: 24 mm;
- plasma-forming gas is supplied in a tangential pattern through 6 channels, each with a diameter of 2 mm;
- the chosen raw material is titanium powder VT1-0, selected from the library of standard materials within the software package (State Standard GOST 19807-91) with the following composition (wt. %, not exceeding): N – 0.04, C – 0.07, H – 0.01, Fe – 0.25, Ni – 0.04, Si – 0.1, O – 0.2).

The environmental conditions are set as follows:

- gas type: air;
- absolute gas pressure at the outlet of the anode unit is 98,100 Pa, equivalent to the altitude of Yekaterinburg;
- temperature corresponds to room temperature, at 293 K.

The study focused on particle motion trajectories within the plasma flow for particle sizes of 1, 50 and 100 μm. The mass flow rate for each fraction was set at 1 g/s.

An indirect-acting plasmatron was employed with the following specifications:

- voltage: 26 V;
- current: 250 A;
- spraying direction: vertically, directed upwards;
- reactor length: 2.8 m;
- diameters of respective segments: 250 and 500 mm.

Results and discussion

In Figure 2 the trajectories of 100 particles for each of the three fractions are depicted. It's important to note that the particle sizes in the figure do not correspond to scale and have been chosen arbitrarily for illustration purposes. We assumed that the temperature at which titanium powder begins to glow and produce bright sparks is above 1573 K. This determination was based on reference data regarding the colors of heated titanium (bright red – 900 °C, yellow – 1200 °C, white – 1300 °C) [24]. Through computer simulation, several key findings were obtained, including the dimensions of the torch containing the luminous powder fraction with temperatures exceeding 1573 K, as well as the maximum distance covered by powder particles within the flow.

The obtained data is presented below:

Powder particle size, μm	1	50	100
Length of luminous fraction, mm	570	500	320
Width of luminous fraction, mm	45	55	60
Distance of particles to plasmatron edge, m	2.8	1.8	1.6

As observed, there is a negative correlation between particle size and the length of the luminous fraction, as well as the distance particles are carried by the flow away from the plasma torch's end. Conversely, the width and opening angle of the plasma flow torch increase with larger particle sizes. This phenomenon can be attributed to the influence of gravity acting upon powder particles entrained by the plasma flow. Notably, smaller powder

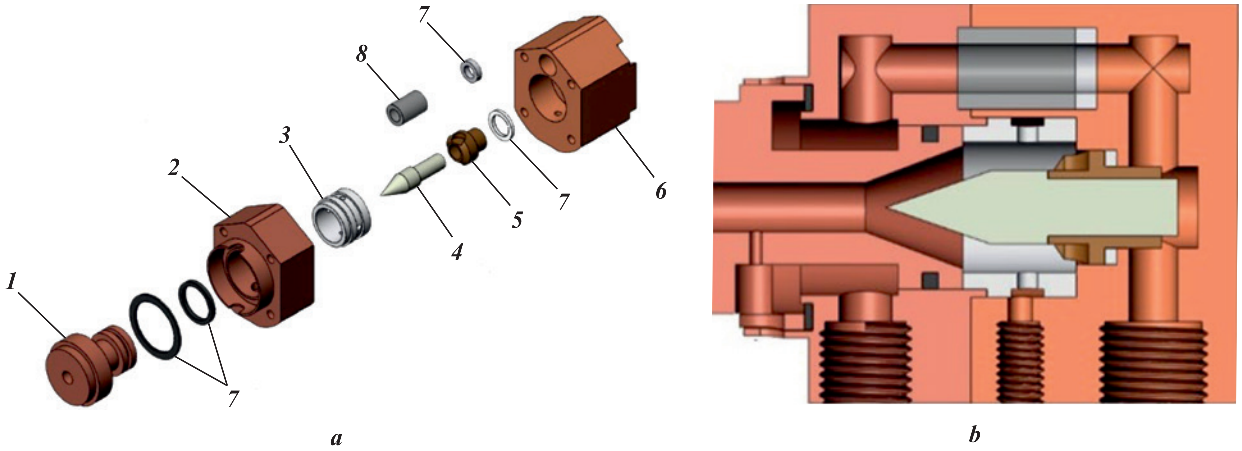

Fig. 1. The design of the plasma head of the installation in a disassembled state (***a***) and in cross section along the axis (***b***)
1 – anode, ***2*** – anode case, ***3*** – swirler, ***4*** – cathode, ***5*** – cathode sleeve, ***6*** – cathode case, ***7*** – sealing rings, ***8*** – sleeve

Рис. 1. Конструкция плазменной головки установки в разобранном состоянии (***a***) и в поперечном сечении вдоль оси (***b***)
1 – анод, ***2*** – корпус анода, ***3*** – завихритель, ***4*** – катод, ***5*** – втулка катода, ***6*** – корпус катода, ***7*** – уплотнительные кольца, ***8*** – втулка

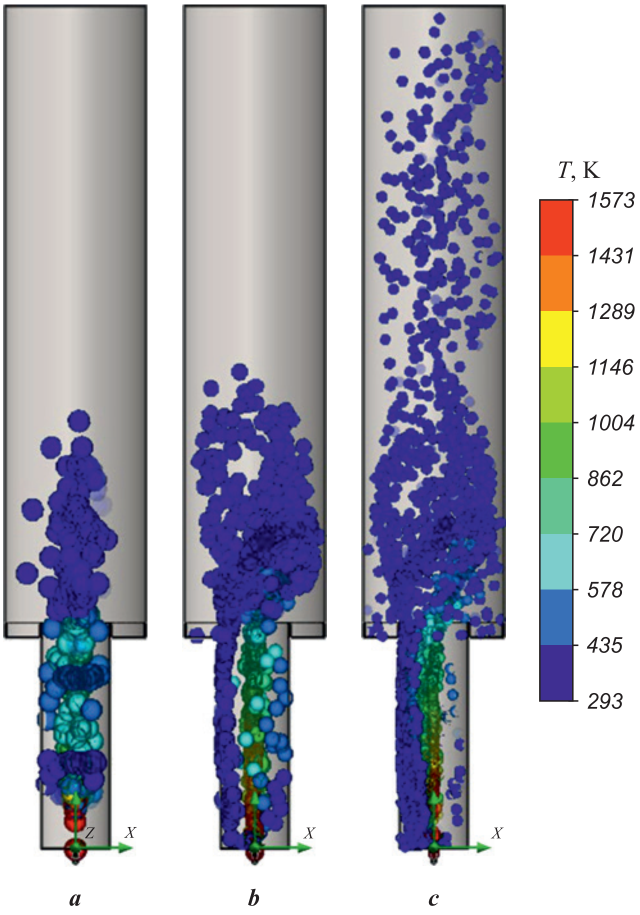

Fig. 2. Trajectories of particles with sizes of 100 (***a***), 50 (***b***), and 1 (***c***) µm

Рис. 2. Картины траекторий частиц размерами 100 (***a***), 50 (***b***) и 1 (***c***) мкм

particles tend to follow longer flight paths within the flow, resulting in greater distances from the plasma head.

In order to validate the outcomes of the computer experiment, two full-scale experiments were conducted. The first experiment aimed to compare the width and length of the torch containing luminous particles of PTM-1 titanium powder, which was sprayed using a laboratory facility (TU 14-22-57-92). In terms of chemical composition, PTM-1 corresponds closely to the titanium powder VT1-0 employed in the computer experiment (wt. %, not exceeding: N – 0.08, C – 0.05, H – 0.35, Fe + Ni – 0.4, Si – 0.1, Ca – 0.05, Cl – 0.004). The second full-scale experiment was designed to determine the temperature of the plasma flow during the plasma torch's idle mode (without powder particle spraying). This measurement aimed to assess the correspondence of this value to the one determined through the computer experiment.

Each of the full-scale experiments was conducted in five separate runs to ensure robust and reliable measurement results. In order to enhance the accuracy and credibility of the measurements, we applied statistical processing using scatter plots and the calculation of their average values [25–27].

In the first full-scale experiment, a granulometric analysis of PTM-1 titanium powder was conducted using CAMSIZER-XT (Germany). The data obtained revealed that 90 % of the powder had a size of less than 91 µm, while 50 % had a size of less than 50 µm. Furthermore, 98.1 % of the powder material exhibited a sphericity coefficient exceeding 0.9 (the ratio of the smallest particle size or diameter to the largest), and 90.9 % of the studied powder displayed sphericity coefficients exceeding 0.9. The particle size range of PTM-1 titanium powder fell within the range of 1–97 µm. Figure 3 presents a visual representation of the data from both full-scale and computer experiments.

In the first full-scale experiment, the initial conditions were as follows:

- plasma-forming gas flow rate: 20 l/min;
- gas type: argon; purity 99.993 % (complying with State Standard 10157-2016);
- gas pressure in the supplying system: 2 atm;

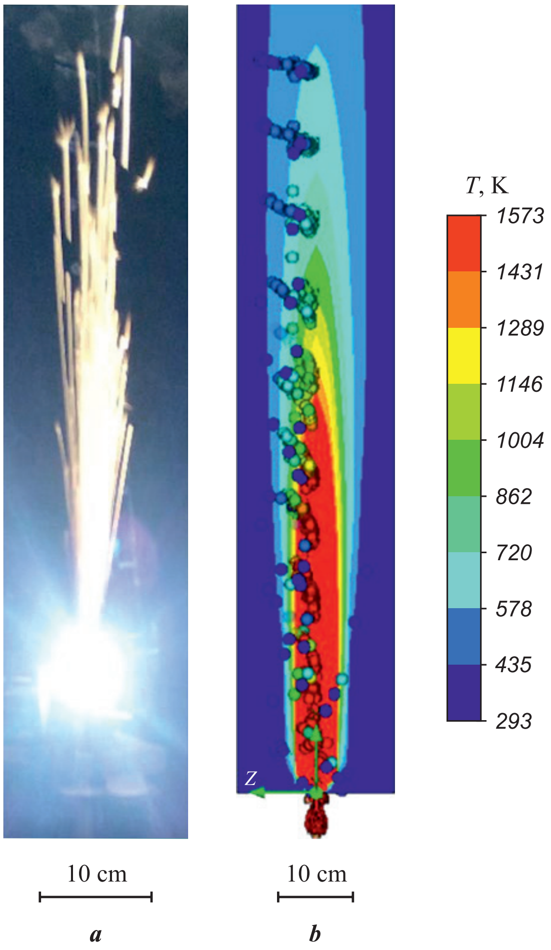

Fig. 3. Data from full-scale (***a***) and computer (***b***) experiments on the length and width of the luminous fraction

Рис. 3. Данные натурного (***a***) и компьютерного (***b***) экспериментов длины и ширины светящейся фракции

Comparison of the results of full-scale and computer experiments

Результаты сравнения натурного и компьютерного экспериментов

Material	Computer experiment, mm	Field experiment, mm	Deviation, %
Copper M1	141	135	4.4
Steel 10	82	85	3.5
Lanthanized tungsten	19	20	5.0

- diameter of the central hole of the swirlers: 24 mm;
- plasma-forming gas was introduced in a tangential pattern through 6 channels, each with a 2 mm diameter.

The environmental conditions were set as follows:

- gas type: air;
- absolute gas pressure at the outlet of the anode unit: 98,100 Pa, equivalent to the altitude of Yekaterinburg;
- temperature was maintained at room temperature – 293 K.

The study focused on analyzing the motion trajectories of particles within the plasma flow, encompassing particle sizes ranging from 1 to 97 µm. The mass flow rate for each fraction was set at 1 g/s. An indirect-acting plasmatron was employed, with the following specifications:

- voltage: 26 V;
- current: 250 A;
- spraying direction: vertical, directed upwards;
- reactor length: 2.8 m;
- diameters of respective segments: 250 and 500 mm.

During the experiment, measurements were taken for the length and width of the luminous fraction of titanium powder, which amounted to 600 mm and 65 mm, respectively. As a result, the deviation from the results of the computer experiment did not exceed 7.7 %.

In the second full-scale experiment, conducted during the idle mode of the plasmatron (without the use of powder), the temperature of the plasma flow on its axis was studied. To achieve this, a method involving the placement of rods with known melting temperatures within the plasma flow was employed. Specifically, 3 rods with a 3 mm diameter, composed of copper M1 (compliant with State Standard GOST 859-2014), steel 10 (in accordance with State Standard GOST 1050-2013) and lanthanized tungsten (as per Specifications TU 48-19-27-88) were selected. These materials were chosen for their varying melting points. The rods were fixed in a manner where one end was securely clamped, and the other end was left free to be exposed to the plasma flow. The head of the plasmatron was mounted on a manipulator, which enabled its uniform movement along the axis toward the rod at a speed of 10 mm per minute. The distance between the free end of the rod and the end plane of the anode of the plasmatron's head unit was meticulously recorded throughout the experiment. The initial distance between the free end of the rod and the plasma torch's head was assumed to be 0.5 m. When the melting process commenced on the rod's surface, the distance from the rod to the plasma torch was recorded.

In order to determine the temperature of the rod's surface at the point of melting onset, an optical pyrometer (EOP-66, Type No. 240, compliant with GOST 5.278) was employed. This pyrometer is specifically designed for accurately estimating the brightness temperatures of heated objects through their thermal radiation, covering a range from 900 to 10,000 °C. The measurement error does not exceed 5 °C.

In the second full-scale experiment, the initial conditions were as follows:

- plasma-forming gas flow rate: 20 l/min;
- gas type: argon; purity 99.993 % (complying with State Standard 10157-2016);
- gas pressure in the supplying system: 2 atm;
- diameter of the central hole of the swirlers: 24 mm;
- plasma-forming gas was introduced in a tangential pattern through 6 channels, each with a 2 mm diameter.

The environmental conditions for this experiment were as follows:

- gas type: air;
- absolute gas pressure at the outlet of the anode unit: 98,100 Pa, equivalent to the altitude of Yekaterinburg;
- temperature was maintained at room temperature – 293 K.

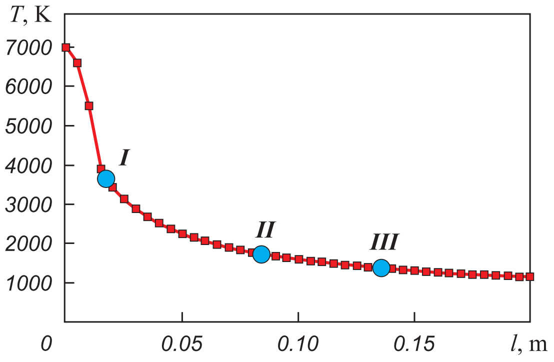

Fig. 4. Temperature distribution along the plasma flow axis (*l*) according to full-scale experiment
I – lanthanated tungsten, ***II*** – steel 10, ***III*** – copper M1

Рис. 4. Распределение температуры вдоль оси плазменного потока (*l*), по данным натурного эксперимента
I – лантанированный вольфрам, ***II*** – сталь 10, ***III*** – медь M1

For this experiment, an indirect-acting plasmatron with the following specifications: was utilized:

- voltage: 26 V;
- current: 250 A;
- spraying direction: vertical, directed upwards;
- reactor length: 2.8 m;
- diameters of respective segments: 250 and 500 mm.

The data derived from the second full-scale experiment indicated that the onset of melting for each of the rods occurred at temperatures closely aligned with the reference data for each rod material, with a slight deviation of no more than 22 K. A comprehensive account of this experiment can be found in [28] and the results are visually presented in Figure 4 and detailed in the accompanying Table.

Thus, the comparative analysis of the computer and field experiments demonstrated a satisfactory level of agreement, with the discrepancy not exceeding 5 %.

Conclusions

A comparative analysis of the motion trajectories of titanium powder particles of varying sizes in a vertically directed plasma flow has been successfully conducted. The study revealed that the size of powder particles significantly influences various parameters, including the dimensions of the luminous fraction, the opening angle of the plasma torch, and the distance of particles carried by the plasma flow from the plasma head. These findings are of great significance for processes involving coating and powder production.

Furthermore, the development of a computer model describing a laboratory plasma facility for applying functional coatings and producing powder materials represents a valuable contribution. This model can be employed to predict outcomes in powder production processes. Additionally, it enables the determination of optimal reactor (powder receiving chamber) dimensions and shapes, with the dual goal of reducing internal volume and mitigating issues such as molten particles adhering to chamber surfaces. This optimization is essential for minimizing the material consumption of process equipment, reducing facility dimensions, and cutting operational costs, especially when inert gases are used to fill the receiving chamber. A well-designed chamber shape not only lowers the unit cost of produced powder but also prevents contamination of internal reactor surfaces.

In the context of vertically upward plasma flow, the influence of gravity leads to a natural separation of sprayed powder into different fractions. Finer particles exhibit a larger scatter radius, while coarser ones are concentrated closer to the plasma jet's axis. This phenomenon can be harnessed for the selective collection of powdered material. As part of the chamber's design improvement, the proposal to introduce additional internal walls for particle deposition based on size is an innovative approach.

Overall, the use of gravity's effect in vertically directed spray patterns serves as an additional tool for segregating the produced powder material.

These study results hold particular utility in the application of functional coatings, aiding in the optimal positioning of the substrate on which they are applied. The computer model offers the capability to predict plasma flow torch characteristics, such as the opening angle and width, in relation to the distance from the plasmatron. This information is invaluable for estimating the coating area, determining the number of required passes of the plasma torch for surface coverage and considering particle temperatures. Moreover, it assists in defining the optimal substrate-to-plasma head distance and inclination.

The choice of directing the atomization process vertically upwards, taking advantage of the natural tendency of heat to rise due to the pressure difference in heated gases, offers several advantages over directing the plasma flow vertically downwards. In this configuration, the heat flow from the plasma is directed toward the substrate positioned above the plasma source. This setup minimizes the risk of overheating and potential damage to the plasma equipment's components, reducing the likelihood of plasma source failure. Additionally, when the plasma flow is directed upwards, the substrate receives more effective heating.

These recommendations have practical significance for both consumers and developers of technological equipment used in coating processes and powder production. By employing a computer model, it becomes feasible to anticipate process outcomes and make adjustments by manipulating influencing factors.

Furthermore, the results of the computer experiment were validated through a full-scale experiment and the comparative analysis of their findings demonstrated a satisfactory level of agreement.

References / Список литературы

1. Zhang X., Cocks A., Okajima Y., Takeno K., Torigoe T. An image-based model for the sintering of air plasma sprayed thermal barrier coatings. *Acta Materialia*. 2021;206:116649. https://doi.org/10.1016/j.actamat.2021.116649
2. Miao Y., Zhu H., Gao P., Li L. The effects of spraying power on microstructure, magnetic and dielectric properties of plasma sprayed cobalt ferrite coatings. *Journal of Materials Research and Technology*. 2020;9(6):14237–14243. https://doi.org/10.1016/j.jmrt.2020.10.006
3. Kim Y., Kim J.H., Han J.-W., Choi J. Multiscale mechanics of yttria film formation during plasma spray coating. *Applied Surface Science*. 2022;572:151416. https://doi.org/10.1016/j.apsusc.2021.151416

4. Ma Y.-d., Wang X.-y., Wang X.-l., Yang Y., Cui Y.-h., Sun W.-w. In-situ TiC-Ti5Si3-SiC composite coatings prepared by plasma spraying. *Surface & Coatings Technology*. 2020;404:126484.
https://doi.org/10.1016/j.surfcoat.2020.126484

5. Umanskii A.P., Terentiev A.E., Brazhevsky V.P. Wear resistance of plasma-sprayed coatings in intensive abrasive wear conditions. *Powder Metallurgy and Metal Ceramics*. 2020;58:559–566.
https://doi.org/10.1007/s11106-020-00110-3

6. Wang J., Lu Z., Huang Y., Zhou L., Xing Z., Wang H., Li Z. The mechanism for the enhanced mechanical and piezoelectricity properties of La_2O_3 doped $BaTiO_3$ ceramic coatings prepared by plasma spray. *Journal of Alloys and Compounds*. 2022;897:162944.
https://doi.org/10.1016/j.jallcom.2021.162944

7. Shi Y., Lu W., Sun W., Zhang S., Yang B., Wang J. Impact of gas pressure on particle feature in Fe-based amorphous alloy powders via gas atomization: Simulation and experiment. *Journal of Materials Science & Technology*. 2022;105:203–213.
https://doi.org/10.1016/j.jmst.2021.06.075

8. Sunpreet S., Seeram R., Rupinder S. Material issues in additive manufacturing: A review. *Journal of Manufacturing Processes*. 2017;25:185–200.
https://doi.org/10.1016/j.jmapro.2016.11.006

9. Oh J.-H., Kim M., Hong S.-H., Lee Y. H., Kim T.-H., Choi S. Facile synthesis of cubic boron nitride nanoparticles from amorphous boron by triple thermal plasma jets at atmospheric pressure. *Advanced Powder Technology*. 2022;33(2):103400.
https://doi.org/10.1016/j.apt.2021.103400

10. Sista K.S., Moon A.P., Sinha G.R., Pirjade B.M., Dwarapudi S. Spherical metal powders through RF plasma spherodization. *Powder Technology*. 2022;400:117225.
https://doi.org/10.1016/j.powtec.2022.117225

11. Gelchinski B.R., Balyakin I.A., Yuryev A.A., Rempel A.A. High-entropy alloys: properties and prospects of application as protective coatings. *Russian Chemical Reviews*. 2022;91(6):RCR5023. https://doi.org/10.1070/RCR5023

Гельчинский Б.Р., Балякин И.А., Юрьев А.А., Ремпель А.А. Высокоэнтропийные сплавы: исследование свойств и перспективы применения в качестве защитных покрытий. *Успехи химии*. 2022;91(6):1–33.

12. Li Q., Zhang N., Gao Y., Qing Y., Zhu Y., Yang K., Zhu J., Wang H., Ma Z., Gao L., Liu Y., He J. Effect of the core-shell structure powders on the microstructure and thermal conduction property of YSZ/Cu composite coatings. *Surface and Coatings Technology*. 2021;424:127658.
https://doi.org/10.1016/j.surfcoat.2021.127658

13. Golewski P., Sadowski T. Technological and strength aspects of layers made of different powders laminated on a polymer matrix composite substrate. *Molecules*. 2022; 27(4):1168. https://doi.org/10.3390/molecules27041168

14. Dong X.-Y., Luo X.-T., Zhang S.-L., Li C.-J. A novel strategy for depositing dense self-fluxing alloy coatings with sufficiently bonded splats by one-step atmospheric plasma spraying. *Journal of Thermal Spray Technology*. 2020;29:173–184.
https://doi.org/10.1007/s11666-019-00943-4

15. Yin Z., Yu D., Zhang Q., Yang S., Yang T. Experimental and numerical analysis of a reverse-polarity plasma torch for plasma atomization. *Plasma Chem Plasma Process*. 2021;41:1471–1495.
https://doi.org/10.1007/s11090-021-10181-8

16. Cui Y., Zhao Y., Numata H., Yamanaka K., Bian H., Aoyagi K., Chiba A. Effects of process parameters and cooling gas on powder formation during the plasma rotating electrode process. *Powder Technology*. 2021;393:301–311.
https://doi.org/10.1016/j.powtec.2021.07.062

17. Alshunaifi I.A., Elaissi S., Ghiloufi I., Alterary S.S., Alharbi A.A. Modelling of a non-transferred plasma torch used for nano-silica powders production. *Applied Sciences*. 2021;11:9842. https://doi.org/10.3390/app11219842

18. Khaji M., Peerenboom K., Mullen J., Degrez G. 2D numerical modeling for plasma-assisted CO_2 pooling in supersonic nozzles: importance of a proper nozzle contour design. *Journal of Physics D: Applied Physics*. 2021;54(16):165202.
https://doi.org/10.1088/1361-6463/abd355

19. Ermakov S.B. Regulation of powder particles shape and size at plasma spraying. *Vektor nauki TGU*. 2021;1:7–15. (In Russ.). https://doi.org/10.18323/2073-5073-2021-1-7-15

Ермаков С.Б. Регулирование формы и размеров частиц порошков при плазменном распылении. *Вектор науки ТГУ*. 2021;1:7–15.
https://doi.org/10.18323/2073-5073-2021-1-7-15

20. Tailor S., Mohanty R.M., Soni P.R. A review on plasma sprayed Al–SiC composite coatings. *Journal of Materials Science & Surface Engineering*. 2013;1(1):15–22.
https://doi.org/10.jmsse/2348-8956/1-1.5

21. Keidar M., Beilis I., Boxman R.L., Goldsmith S. 2D expansion of the low-density interelectrode vacuum arc plasma jet in an axial magnetic field. *Journal of Physics D: Applied Physics*. 1996;29:1973.
https://doi.org/10.1088/0022-3727/29/7/034

22. Piralishvili Sh.A., Polyaev V.M., Sergeev M.N. Swirl effect. Experiment, theory, technical solutions. Moscow: UNPTs “Energomash”, 2000. 412 p. (In Russ.).

Пиралишвили Ш.А., Поляев В.М., Сергеев М.Н. Вихревой эффект. Эксперимент, теория, технические решения. М.: УНПЦ «Энергомаш», 2000. 412 с.

23. Okulov R.A., Krashaninin V.A., Popov E.V. Plasma jet stream simulation for formation coating and powder manufacturing processes. *Journal of Physics: Conference Series*. 2021;1954(1):012033.
https://doi.org/10.1088/1742-6596/1954/1/012033

24. Wolf W., Herman B., La Rocca E., Syute G., Turner R., Hufnagel R. Handbook of infrared technology. Moscow: Mir, 1995. 606 p. (In Russ.).

Волф У., Герман Б., Ла Рокка Э., Сьюте Г., Тернер Р., Хуфнагел Р. Справочник по инфракрасной технике. М.: Мир, 1995. 606 с.

25. Solonin I.S. Mathematical statistics in engineering technology. Moscow: Mashinostroenie, 1972. 215 p. (In Russ.).

Солонин И.С. Математическая статистика в технологии машиностроения. М.: Машиностроение, 1972. 215 с.

26. Kravchenko N.S., Revinskaya O.G. Methods for processing the results of measurements and estimating errors in the educational laboratory workshop: a tutorial. Tomsk: Izdatel'stvo Tomskogo politekhnicheskogo universiteta, 2011. 88 p. (In Russ.).

Кравченко Н.С., Ревинская О.Г. Методы обработки результатов измерений и оценки погрешностей в учебном лабораторном практикуме: Учебное пособие. Томск: Изд-во Томского политехнического университета, 2011. 88 с.

27. Okulov R.A., Popov E.V., Gelchinsky B.R., Rempel A.A. Development of the computer model of the plasma installation. *Journal of Physics: Conference Series*. 2021;2064(1):012044. https://doi.org/10.1088/1742-6596/2064/1/012044

28. Okulov R.A., Sarsadskikh K.I., Ilinykh S.A., Zakharov M.N. Effect of the plasma-forming gas consumption on processes of plasma spray coating and metal powder production. *Journal of Physics: Conference Series*. 2019;1281:012058. https://doi.org/10.1088/1742-6596/1281/1/012058

Information about the Authors

Roman A. Okulov – Cand. Sci. (Eng.), Assistant Professor of the Department "Engineering graphics", Ural Federal University named after the first President of Russia B.N. Yeltsin (UrFU); Senior Researcher of Laboratory of Powder and Composite Materials, Institute of Metallurgy of the Ural Branch of the Russian Academy of Sciences (IMET UB RAS).
ORCID: 0000-0003-4488-9190
E-mail: okulov.roman@gmail.com

Suleiman M. Akhmetshin – Engineer of Scientific-research, Laboratory of Powder and Composite Materials, IMET UB RAS.
ORCID: 0009-0000-0814-6790
E-mail: k009893@yandex.ru

Boris R. Gelchinsky – Dr. Sci. (Phys.-Math.), Head of the Department of Materials Science, IMET UB RAS.
ORCID: 0000-0001-5964-5477
E-mail: brg47@list.ru

Andrey A. Rempel – Dr. Sci. (Phys.-Math.), Academician of the Russian Academy of Sciences, Director of IMET UB RAS.
ORCID: 0000-0002-0543-9982
E-mail: rempel.imet@mail.ru

Сведения об авторах

Роман Александрович Окулов – к.т.н., доцент кафедры «Инженерная графика», Уральский федеральный университет имени первого Президента России Б.Н. Ельцина (УрФУ); ст. науч. сотрудник лаборатории порошковых и композиционных материалов, Институт металлургии Уральского отделения РАН (ИМЕТ УрО РАН).
ORCID: 0000-0003-4488-9190
E-mail: okulov.roman@gmail.com

Сулейман Муллаянович Ахметшин – инженер лаборатории порошковых и композиционных материалов, ИМЕТ УрО РАН.
ORCID: 0009-0000-0814-6790
E-mail: k009893@yandex.ru

Борис Рафаилович Гельчинский – д.ф.-м.н., руководитель отдела материаловедения, ИМЕТ УрО РАН.
ORCID: 0000-0001-5964-5477
E-mail: brg47@list.ru

Андрей Андреевич Ремпель – д.ф.-м.н., академик РАН, директор ИМЕТ УрО РАН.
ORCID: 0000-0002-0543-9982
E-mail: rempel.imet@mail.ru

Contribution of the Authors

R. A. Okulov – Conceptualization, goal and objective definition, manuscript writing, calculations, formulation of conclusions.

S. M. Akhmetshin – Experimental preparation, full-scale experiment conduct, manuscript writing.
B. R. Gelchinsky – Resource provision, manuscript writing, experimental results analysis.
A. A. Pempel – Academic supervision, experimental results analysis, manuscript revision, conclusions revision.

Вклад авторов

Р. А. Окулов – формирование основной концепции, постановка цели и задачи исследования, подготовка текста, осуществление расчетов, формулировка выводов.
С. М. Ахметшин – подготовка эксперимента, проведение натурного эксперимента, подготовка текста статьи.
Б. Р. Гельчинский – обеспечение ресурсами, подготовка текста, анализ результатов исследований.
А. А. Ремпель – научное руководство, анализ результатов исследований, корректировка текста, корректировка выводов.

Received 22.11.2022
Revised 08.06.2023
Accepted 09.06.2023

Статья поступила 22.11.2022 г.
Доработана 08.06.2023 г.
Принята к публикации 09.06.2023 г.

Nanostructured Materials and Functional Coatings
Наноструктурированные материалы и функциональные покрытия

UDC 621.45.038.7

https://doi.org/10.17073/1997-308X-2023-3-55-66

Research article
Научная статья

Effect of HG40 and HS123 hard alloy tool substrates on the properties of hardening coating

V. S. Sergevnin ✉, I. V. Blinkov, D. S. Belov, A. P. Demirov, A. V. Chernogor,
T. A. Lobova, A. I. Laptev

National University of Science and Technology "MISIS"
4 bld. 1 Leninskiy Prosp., Moscow 119049, Russia

✉ v.s.sergevnin@gmail.com

Abstract. This article examines the impact of surface and near-surface layer properties of a hard alloy on the physico-mechanical and tribological properties of Mo–Ti–Ni–Si–Al–N CAPVD-coatings deposited on HG40 and HS123 cutting tools. In both cases, the coatings had similar composition, multilayer architecture, and nanograin structure, with crystallite sizes ranging from 6 to 10 nm. However, there were significant differences in the hardness, elasticity modulus, and relative work of plastic deformation between the coatings. Specifically, on HG40 substrates, the hardness, elasticity modulus, and relative work of plastic deformation were equal to 27.6 GPa, 647 GPa and 38.2 %, respectively, while on HS123 substrates, they were 34.2 GPa, 481 GPa and 46.2 %, respectively. Furthermore, coatings formed on HS123 hard alloy demonstrated superior wear resistance and stronger adhesion. This can be attributed to the presence of higher compressive macrostresses within the coating. The maximum value of this property, approximately 5.2 GPa, was achieved when deposed to HS123 hard alloy, whereas the coating applied to HG40 reached a maximum value of approximately 3.2 GPa. Additionally, a more extensive diffusion zone between the substrate and coating components, along with associated structural phase heterogeneity, was observed at the coating-substrate interface when applied to HS123 substrate.

Keywords: coatings, arc-PVD, macrostresses, hardness, substrate–coating boundary

Acknowledgements: This work was supported by the Russian Science Foundation, project No. 19-19-00555, https://rscf.ru/project/19-19-00555/.

For citation: Sergevnin V.S., Blinkov I.V., Belov D.S., Demirov A.P., Chernogor A.V., Lobova T.A., Laptev A.I. Effect of HG40 and HS123 hard alloy tool substrates on the properties of hardening coating. *Powder Metallurgy and Functional Coatings*. 2023;17(3): 55–66. https://doi.org/10.17073/1997-308X-2023-3-55-66

Влияние твердосплавной инструментальной основы ВК10 и Т14К8 на свойства упрочняющего покрытия

В. С. Сергевнин ✉, И. В. Блинков, Д. С. Белов, А. П. Демиров,
А. В. Черногор, Т. А. Лобова, А. И. Лаптев

Национальный исследовательский технологический университет «МИСИС»
Россия, 119049, г. Москва, Ленинский пр-т, 4, стр. 1

✉ v.s.sergevnin@gmail.com

Аннотация. Исследовано влияние свойств поверхности и приповерхностного слоя твердого сплава на физико-механические и трибологические характеристики arc-PVD-покрытий Mo–Ti–Ni–Si–Al–N, нанесенных на твердосплавные пластины ВК10 и Т14К8. В обоих случаях покрытия характеризовались примерно одинаковым составом, многослойной архитектурой и нанозеренной структурой с размером кристаллитов 6–10 нм. При этом твердость, модуль упругости и относительная работа пластической деформации покрытий существенно отличались и составляли 27,6 ГПа, 647 ГПа, 38,2 % и 34,2 ГПа, 481 ГПа, 46,2 % соответственно на подложках ВК10 и Т14К8. Одновременно минимальный износ и повышенная адгезионная прочность также были свойственны покрытиям, сформированным на твердом сплаве Т14К8. Обнаруженный эффект объясняется с позиции повышенных значений сжимающих макронапряжений, возникающих в покрытии. Значения данной характеристики для исследованного покрытия имели максимальное значение ~5,2 ГПа при нанесении на твердый сплав Т14К8 против ~3,2 ГПа для покрытия, нанесенного на ВК10. При этом наиболее протяженная диффузионная зона между компонентами подложки и покрытия и связанная с ней структурно-фазовая неоднородность формируются на границе покрытие–подложка при нанесении на подложку Т14К8.

Ключевые слова: покрытия, arc-PVD, макронапряжения, твердость, граница подложка–покрытие

Благодарности: Исследование выполнено за счет гранта Российского научного фонда № 19-19-00555, https://rscf.ru/project/19-19-00555/.

Для цитирования: Сергевнин В.С., Блинков И.В., Белов Д.С., Демиров А.П., Черногор А.В., Лобова Т.А., Лаптев А.И. Влияние твердосплавной инструментальной основы ВК10 и Т14К8 на свойства упрочняющего покрытия. *Известия вузов. Порошковая металлургия и функциональные покрытия*. 2023;17(3):55–66. https://doi.org/10.17073/1997-308X-2023-3-55-66

Introduction

The studies conducted in the field of functional nanostructured surface coatings development have shown that multicomponent coating structures with different architectures based on nitrides exhibit superior operational performance compared to two and three component systems. These coatings possess enhanced elastic properties, resulting in greater resistance to plastic deformation. The inclusion of additional components in mononitride coatings leads to a reduction in average crystallite sizes and an increase in microdeformation, offering a potential approach to achieve coating materials that combine high hardness and resistance to destruction. Furthermore, these systems exhibit elevated heat resistance and thermal stability [1–5].

The fabrication process of Mo–Ti–Ni–Si–Al–N ion plasma arc vacuum coatings on heat resistant alloy substrates, as well as their properties, are discussed in reference [6]. The coating exhibits a multilayer structure consisting of nanograins with a crystallite size ranging from approximately 6 to 10 nm. The hardness of the coating is approximately 48 GPa, and it demonstrates high ratios of hardness to the Young modulus: $H/E = 0.12$ and $H^3/E^2 = 0.61$ GPa. These values indicate that the material has increased resistance to both elastic and plastic deformations [7; 8]. The coating shows a cohesive pattern of destruction when subjected to scribing, with partial substrate opening observed at an indenter load of approximately 70 N. Additionally, it is important to mention the tribological properties of the coating.

The combination of the aforementioned properties suggests that these coatings hold great potential for use as surface hardening for cutting tool [9–11]. However, the influence of the tool substrate's nature on the functional properties of these coatings remains unsolved. Several studies in this field have shown that the performance of substrate-coating composites is significantly affected by factors such as substrate composition, hardness, surface roughness, and the coefficients of thermal expansion of both the coating and the substrate.

This research aims to investigate the influence of two different types of hard alloys substrates on the properties of the hardening coating and the resulting substrate-coating composite. By examining the obtained results, we can determine the role of the substrate in shaping the functional properties of the coating and identify its most promising application.

Experimental

Coatings were applied to the surface of hard alloy substrates, specifically HG40 and HS123 hard alloy grades, which are commonly used for semifinal and rough milling [15; 16]. The coatings were fabricated using the arc-PVD method, which involves ion plasma vacuum arc spraying. The equipment used for this process included three evaporated cathodes (made of molybdenum, Al–Si alloy with 20 at. % and Ti–Ni alloy with 50 at. %). Toroidal electromagnetic separators were employed to prevent the deposition of sprayed material into the coating structure. To ensure uniform deposition, a kinematic rotating mechanism of the planetary type was used, rotating the substrates at a rate of 1 rpm with respect to the evaporated cathodes.

The coatings were deposited in a nitrogen atmosphere at $P_{N_2} \sim 3\cdot10^{-1}$ Pa. The electric arc current supplied to the evaporate cathodes was 120 A, while a negative bias voltage (U_c) –120 V was applied to the substrates. Prior to the coating deposition, the processed items' surfaces were subjected to preliminary gas abrasive processing using a mixture of air and corundum abrasive particles with a particle size distribution of 20–30 µm. This process resulted in a surface roughness of $R_a \sim 0.1$ µm. The thickness of the obtained coatings was 4 ± 0.1 µm.

The morphology of the coating was analyzed using JSM-7600F and JSM-6700F scanning electron microscopes (JEOL, Japan). The transversal cross-section structure of the Mo–Ti–Ni–Si–Al–N coatings was examined using a JEM-1400 transmission electron microscope, utilizing bright and dark field imaging, microdiffraction, and phase composition estimation.

X-ray photoelectron spectroscopy (XPS) was used to determine the bond energies of the elements present in the coating material, along with the simultaneous determination of their concentrations and the plotting of concentration profiles. This analysis was carried out using a Versa ProbeII device (ULVAC-PHI, Japan). Layer-by-layer analysis was conducted by spraying the coating surface with an argon ion beam with an energy of 2 keV and a 2×2 mm^2 grid, corresponding to an etching rate of 13 nm/min for SiO_2. The diameter of the analyzed region was 100 μm, and photoemission was excited using monochromatic AlK_α radiation with a power of 25 W. High-resolution photoelectron spectra were obtained with an analyzer transmission energy of 11.75 eV and a data acquisition density of 0.1 eV/step.

The diffusion zone at the interface between the coating and substrate was analyzed using electron Auger spectroscopy with a PHI-680 instrument (Physical Electronics, USA). Layer-by-layer ion etching of the material was performed using argon ions with energies of 1 and 2 keV at rates of approximately 5 and 20 nm/min, respectively, within a 1×1 mm grid and an incident angle of 60°.

The hardness (*H*) and elasticity modulus (*E*) of the Mo–Ti–Ni–Si–Al–N coatings applied to HG40 (WC–10Co) and HS123 (WC–14TiC–8Co) substrates were determined using continuous indentation in the load range of 5 to 100 mN, following the Oliver–Pharr method [17]. The relative work of plastic deformation was estimated based on the obtained loading-unloading curves, which was then used to estimate fracture toughness. The measurements were conducted with the indenter penetration depth not exceeding 10 % of the coating thickness to ensure that the material did not influence the determined parameters, in accordance with requirements of ISO/CD 14577.

The coefficient of friction and wear resistance parameters of the coatings were investigated using an automatic Tribometer friction machine (CSM Instruments, Switzerland). Tribological tests were conducted in a pin-on-disk configuration at ambient temperature in an air environment, using an Al_2O_3 counterbody. The normal contact load on the counterbody was 5 N, the friction velocity was set at approximately 10 cm/s, and the friction path length was 100 m. The wear intensity of the samples was determined through optical profilometry using a WYKO NT 1100 device («Veeco», USA).

The adhesion/cohesion strength in the coating–substrate system was estimated by performing scratching tests using a Revetest scratch tester (CSM Instruments, Switzerland). A series of scratches was applied to the coating surface using a diamond indenter with gradually increasing load up to 90 N. During this procedure, contact parameters such as acoustic emission (*AE*) from the contact area, force of friction between the indenter and sample surface (F_f) and the coefficient of friction (μ) were recorded. The critical loads, L_{c1} and L_{c3}, were determined, corresponding to the occurrence of the first scratch and the point at which the indenter made contact with the material, respectively. Additionally, the pattern of material destruction along the scratch was observed using optical microscopy.

The macrostresses in the coating, resulting from the difference in thermal expansion between the coating and substrate, as well as the different specific volume of phases, can be calculated using the Stoney equation. This equation is based on the curvature radius of the coating-substrate composite, which becomes curved due to these macrostresses. When the thickness of the coating is significantly smaller than the thickness of the substrate, the Stoney equation can be used to calculate the macrostresses caused by this difference in thermal expansion [18–21]:

$$\sigma = \frac{1}{6}\left(\frac{1}{R} - \frac{1}{R_0}\right)\frac{E_s t_s^2}{(1 - v_s)t_f}, \tag{1}$$

where E_s represents the Young modulus of the substrate, GPa; v_s is the Poisson ratio of the substrate; R and R_0 are the curvature radii of the substrate before the application of the coating and after the deposition of the substrate-coating composite, respectively, m. The thicknesses of the substrate and coating are denoted by t_s and t_f, respectively, and they were determined by analyzing micro images of transversal fractures using a JSM-6700F scanning electron microscope.

To calculate the curvature radii of the blades before and after the deposition of the coating (R and R_0), profilograms of the sample surface were obtained using an optical profilometer. The following equation was used:

$$R = \frac{L^2}{8b}, \tag{2}$$

where L represents the end-to-end length of the sample upon bending, m; b is the bending parameter.

Results and discussion

The surface morphology of the coatings obtained was characterized by a cellular structure, as depicted in

Figure 1. This structure was formed due to the replication of the relief of the substrate surface by the coating after undergoing preliminary gas abrasive treatment. The parameters of surface roughness (R_a) for all the coatings obtained were measured to be 0.10 ± 0.005 µm, indicating sufficiently uniform morphology.

The application of Arc-PVD Mo–Ti–Ni–Si–Al–N coatings on the utilized substrates resulted in coatings with a multilayer architecture, exhibiting a nanograin structure and crystallite sizes ranging from 6 to 10 nm (Figure 2).

The electron diffraction patterns of the coatings (Figure 3) reveal distinctive lines of electron diffraction. These lines can be attributed to both the TiN and Mo_2N phase due to the observed decrease in intraplane distances. This indicates the presence and consistent nature of the texture in the coatings formed on the two substrates, where the predominant crystallographic orientation of structural constituents aligns in the (100) direction, which corresponds to the direction of coating growth.

The elemental composition of the coatings was investigated using *X*-ray photoelectron spectroscopy (XPS), which provided data on the binding energy of the elements, enabling the determination of their phase composition. Table 1 presents the concentrations of elements in the coating at different depths after etching for 10 and 20 min. The experimental findings revealed the presence of regions within the coating structure enriched with various components. The periodical distribution of elements in the coatings was attributed to the rotation of substrates at a predetermined velocity relative to evaporated cathodes of specific composition. The laminar architecture of the coatings, as observed in Figure 2 using transmission electron spectroscopy (TEM), was further confirmed by concentration profiles obtained during the layer-by-layer etching of the surface with argon ions (Figure 4).

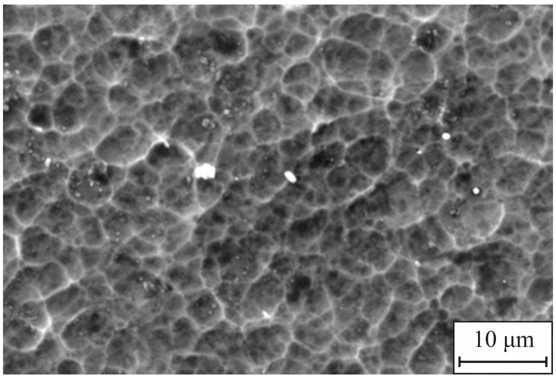

Fig. 1. SEM image of morphology of Mo–Ti–Ni–Si–Al–N coating

Рис. 1. СЭМ-микрофотография морфологии покрытия Mo–Ti–Ni–Si–Al–N

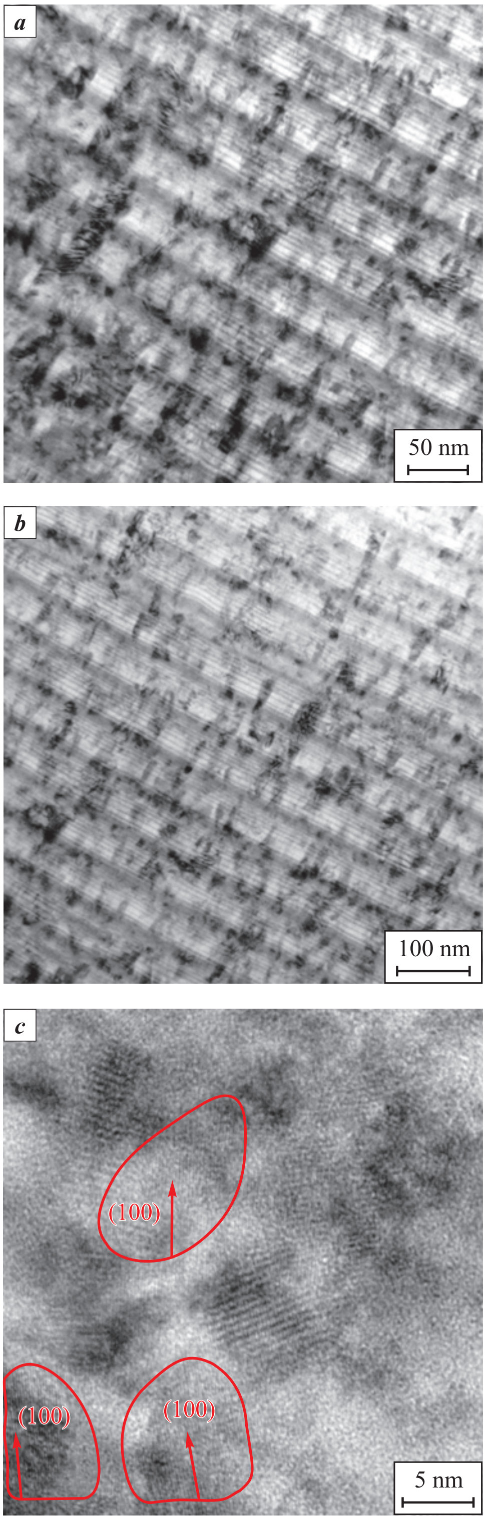

Fig. 2. TEM images of structure of Mo–Ti–Ni–Si–Al–N coatings on carbide alloy substrates HG40 (***a***, ***c***) and HS123 (***b***)

Рис. 2. ПЭМ-изображения структуры покрытий Mo–Ti–Ni–Si–Al–N на твердосплавных основах ВК10 (***a***, ***c***) и Т14К8 (***b***)

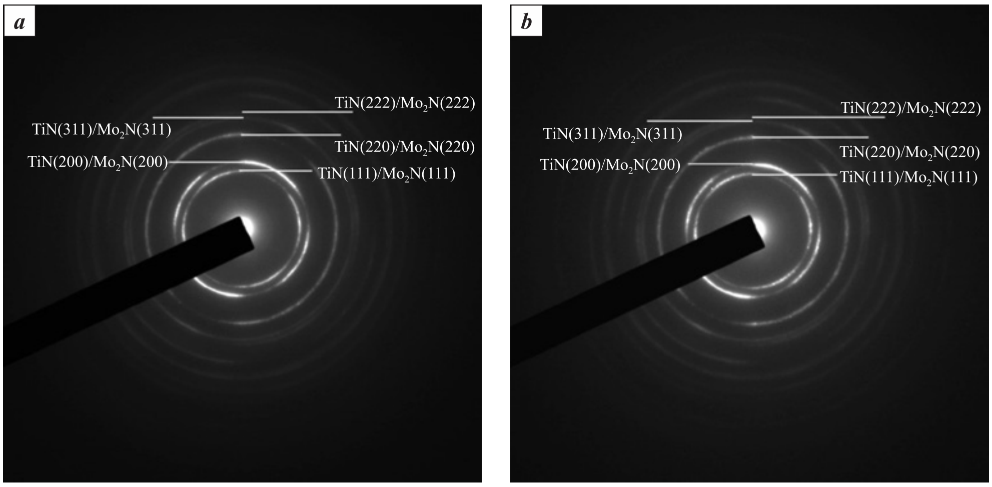

Fig. 3. Electron diffraction patterns of Mo–Ti–Ni–Si–Al–N coating on HG40 (***a***) and HS123 (***b***)

Рис. 3. Электронограммы покрытия Mo–Ti–Ni–Si–Al–N на подложках ВК10 (***a***) и Т14К8 (***b***)

Table 1. **Composition of Mo–Ti–Ni–Si–Al–N coatings on carbide alloy substrates HG40 and HS123 after surface etching with argon ions during XPS (at the depth of ~130 and 260 nm)**

Таблица 1. **Состав покрытий Mo–Ti–Ni–Si–Al–N, сформированных на твердосплавных подложках ВК10 и Т14К8 после травления поверхности ионами аргона в процессе РФЭС (на глубине ~130 и 260 нм)**

Etching duration, min	Concentration of elements, at. %						
	O	N	Ti	Mo	Ni	Al	Si
10	3.5 ± 0.1	45.0 ± 0.1	14.4 ± 0.1	30.0 ± 0.1	5.6 ± 0.1	1.5 ± 0.1	–
20	–	41.3 ± 0.1	8.3 ± 0.1	26.4 ± 0.1	4.7 ± 0.1	14.6 ± 0.1	4.7 ± 0.1

It is important to consider that XPS signal accumulation occurs from a region with a depth of several nanometers. As a result, the concentration profiles of coating elements obtained during the etching of the coating surface with argon ions may exhibit smoothed boundaries between individual layers [22]. This introduces some inconsistency in our understanding of the structure of the coatings, as observed through TEM data, which show well-defined layer boundaries, and XPS data, which exhibit smoothly varying concentration profiles of elements within the layers.

The coatings applied on two different substrates consisted of Mo$_2$N, AlN, Si$_3$N$_4$, TiN and Ni. This is supported by the analysis of energy spectra of photoelectrons from Mo 3d, Al 2p, Si 2p, Ti 2p and Ni 2p, which exhibit bond energies of 228.2 (3d5/2), 74.0, 102.2, 455.0 (Ti 2p3/2) and 853.1 (2p3/2) eV respectively [23–26].

Table 2 provides an overview of the hardness (H), elasticity modulus (E) and relative work of plastic deformation (W_p) for the coatings on different substrates.

The coatings that were obtained and had similar elemental and phase compositions when applied to different hard alloy substrates exhibited notable differences in terms of hardness. These differences were observed while adhering to the “ten percent” rule during hardness measurements [27]. However, despite the similar average coefficients of friction of approximately 0.6 observed during tribological tests (Figure 5), the wear of the coatings manifested in various manners.

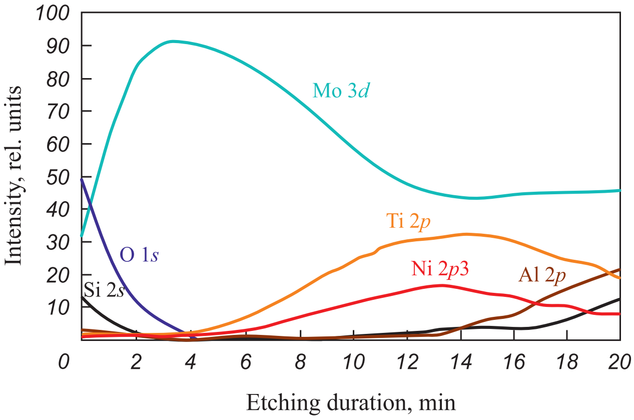

Fig. 4. Distribution of chemical elements in Mo–Ti–Ni–Si–Al–N coatings on carbide substrates during argon ion etching (nitrogen excluded)

Рис. 4. Распределение химических элементов в покрытии Mo–Ti–Ni–Si–Al–N на твердосплавных подложках в процессе травления ионами аргона (без учета азота)

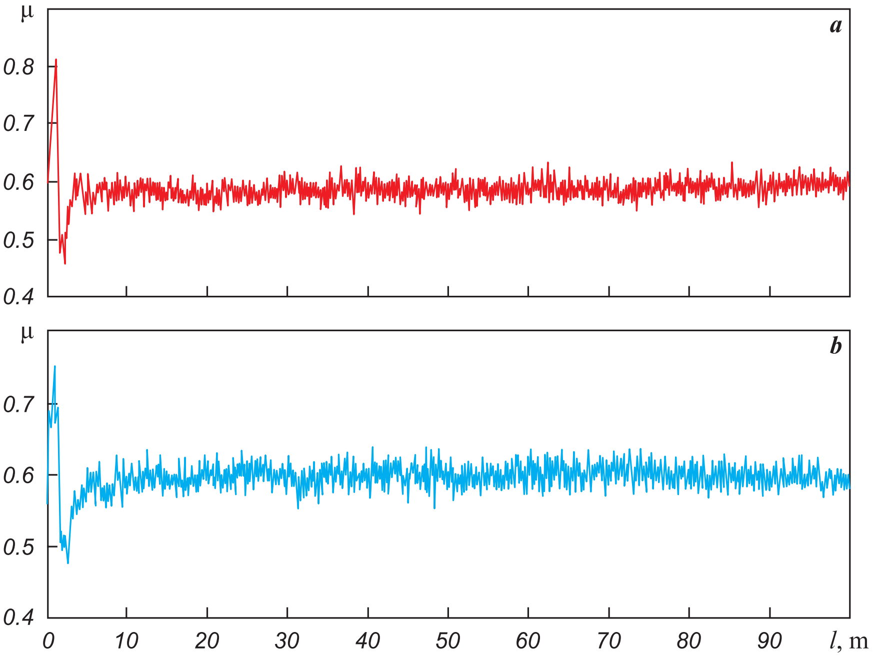

Fig. 5. Friction coefficient as a function of friction path for Mo–Ti–Ni–Si–Al–N coating on HG40 (***a***) and HS123 (***b***) at a load of 5 N on Al_2O_3 counterbody

Рис. 5. Зависимость коэффициента трения от пути трения для покрытия Mo–Ti–Ni–Si–Al–N на подложках ВК10 (***а***), Т14К8 (***b***) при нагрузке 5 Н на контртело из Al_2O_3

Based on the wear track profiles shown in Figure 6, it can be observed that the Mo–Ti–Ni–Si–Al–N coating on HS123 substrates experienced minimal wear, with the track depth comparable to the roughness of initial coating surface. On the other hand, the coatings on HG40 substrates exhibited wear of approximately $2.622 \cdot 10^{-5}$ $mm^3/(N \cdot m)$. These results can likely be attributed to the differing hardness of the Mo–Ti–Ni–Si–Al–N coating on the different substrates.

It is important to note that the nature of the substrate also plays a significant role in the adhesion between the coating and the substrate.

Table 2. **Physicomechanical properties of the considered samples of Mo–Ti–Ni–Si–Al–N coatings HG40 and HS123 substrates**

Таблица 2. **Физико-механические характеристики исследуемых образцов покрытий Mo–Ti–Ni–Si–Al–N и подложек ВК10 и Т14К8**

Substrate	E, GPa	H, GPa	W_p, %
Samples with coating			
HG40	647 ± 25	27.6 ± 1.1	38.2 ± 1.5
HS123	481 ± 19	34.2 ± 1.3	46.2 ± 1.8
Samples without coating			
HG40	574 ± 22	12.9 ± 0.5	–
HS123	520 ± 20	17.4 ± 0.7	–

Figure 7 depicts the variations in three recording parameters (AE, F_f and μ) in relation to the of scratch length and increasing load on the indenter during the measurement of the scratching process on the coatings applied to HG40 and HS123 substrates. The coatings in both series undergo destruction in multiple stages as a result of the diamond indenter. As the load

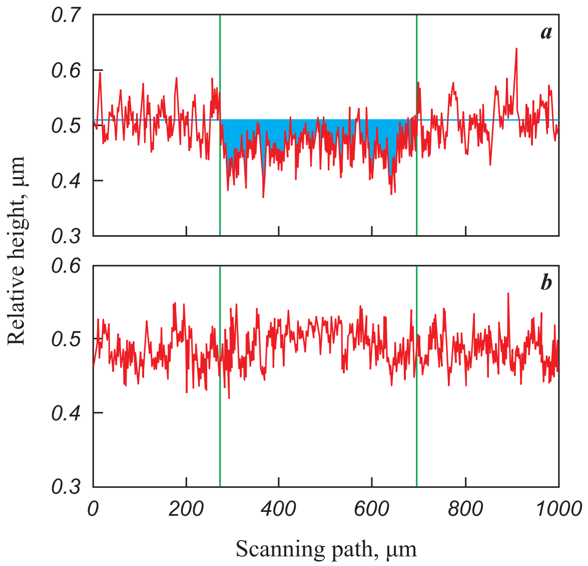

Fig. 6. Profilograms of wear tracks of Mo–Ti–Ni–Si–Al–N coating on HG40 (***a***) and HS123 (***b***) substrates

Рис. 6. Профилограммы дорожек износа покрытия Mo–Ti–Ni–Si–Al–N на подложках ВК10 (***а***) и Т14К8 (***b***)

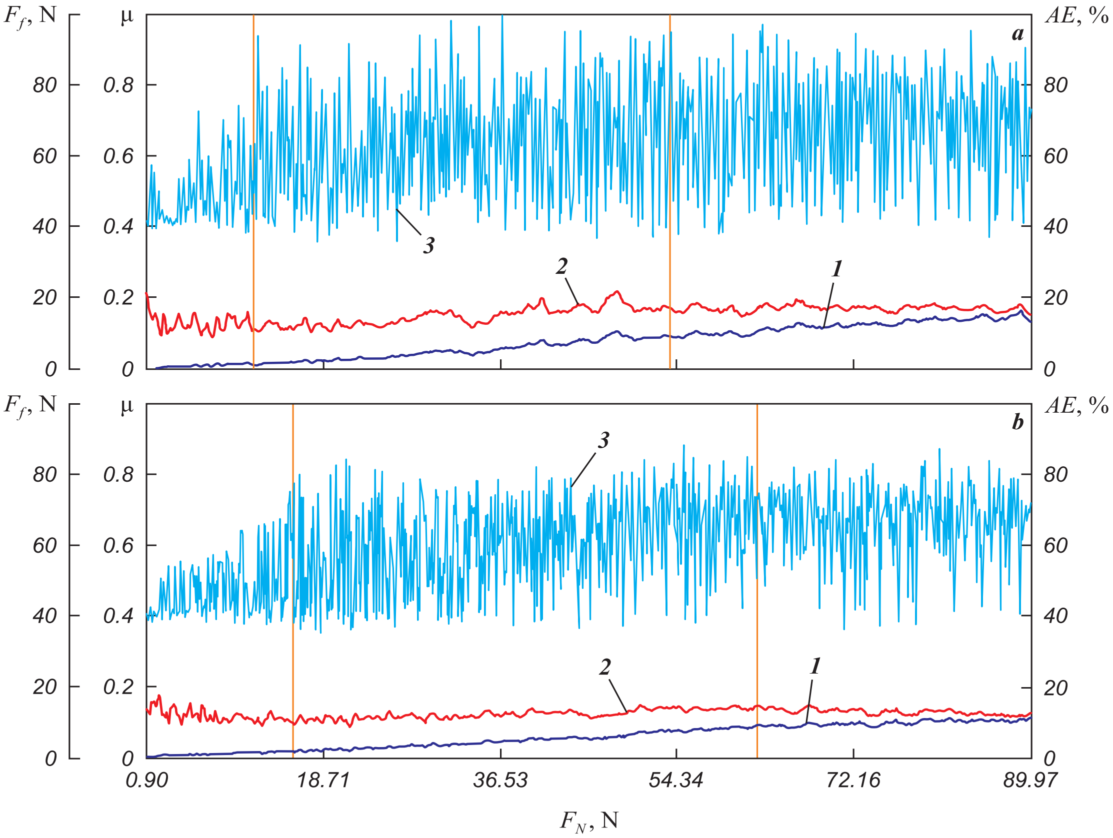

Fig. 7. Friction force (F_f) (***1***), coefficient of friction (μ) (***2***), acoustic emission (*AE*) (***3***) during scratch test of Mo–Ti–Ni–Si–Al–N coatings on HG40 (***a***) and HS123 (***b***) substrates

Рис. 7. Зависимости силы трения (F_f) (***1***), коэффициента трения (μ) (***2***), акустической эмиссии (*AE*) (***3***) при скретч-тесте покрытий Mo–Ti–Ni–Si–Al–N на подложках ВК10 (***a***) и Т14К8 (***b***)

increases, the indenter progressively penetrates into the coating, eliminating surface irregularities and intermittently contacting the surface. During this stage, the signal amplitude of acoustic emission exhibits an increase, while the intensity remains relatively constant, albeit at a negligible level.

A significant drop in amplitude (*AE*) occurs at loads of approximately 11.7 and 15.6 N (L_{c1}) on the indenter for both HG40 and HS123 coatings, as shown in Figure 7. This drop indicates the initiation of the first cracks in the coating. Visual examination of the scratch bottom (Figure 8) confirms the presence of cracks and detachment of coating fragments. Partial wear of the coatings on HG40 and HS123 substrates occurs at loads (L_{c3}) on the indenter of approximately 53.7 and 62.5 N, respectively. Simultaneously, the slope angle of the force F_f curve (*1*) and the coefficient of friction μ (*2*) change as a function of the applied load (refer to Fig. 7). These changes are attributed to the penetration of the indenter into the substrate, which has a lower hardness compared to the coating material.

The hardness, wear, and adhesion of coatings with the same composition, thickness, and structural properties were found to be influenced by the nature of the substrate onto which they were deposited. To investigate this phenomenon, macrostressed states in the formed coating-substrate composites were analyzed.

In this analysis, sufficiently thin substrates were fabricated from the considered hard alloys, with average thicknesses of approximately 425.12 μm and 449.67 μm, respectively. Mo–Ti–Ni–Si–Al–N coatings of the aforementioned compositions, with thicknesses ranging from 4.11 to 4.21 μm, were then applied onto these substrates. The curvature radii were measured before and after the deposition of the coatings. By employing Equation (1) and utilizing published data on the Poisson ratios of the hard alloy substrates, as well as experimentally obtained elasticity moduli of the substrates (as shown in Table 3), the macrostresses (σ) in the coatings were calculated. The results of these calculations are summarized in Table 3. As evident from the presented results, the coatings formed on HS123 substrates exhibited the highest values of σ, indicating the presence of high levels of compressive macrostresses. These compressive macrostresses can account for the elevated hardness of the coatings on these substrates, which, in turn, influ-

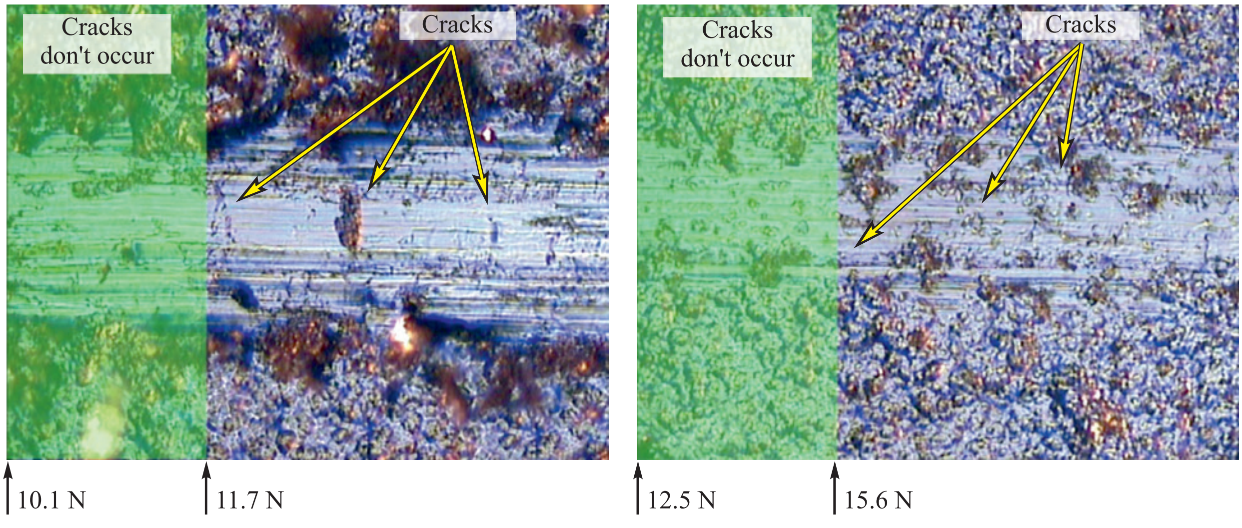

a ***b***

Fig. 8. Images of a scratch fragment formed during the scratch test of Mo–Ti–Ni–Si–Al–N nanostructured coatings on HG40 (***a***) and HS123 (***b***) substrates upon increasing load on indenter

Рис. 8. Изображения участка царапины, формирующейся в процессе скретч-теста наноструктурных покрытий Mo–Ti–Ni–Si–Al–N на подложках ВК10 (***a***) и Т14К8 (***b***) при увеличивающейся нагрузке на индентор

ences their wear resistance [28; 29]. The significant role of compressive macrostresses in relation to coating hardness is further supported by the experimental findings of other researchers [30–35].

The higher adhesion strength observed for Mo–Ti–Ni–Si–Al–N coatings on HS123 substrates, compared to HG40 substrates, can be attributed to the relatively higher macrostresses achieved in the former case. These macrostresses can have a significant impact on the nucleation and propagation of cracks during scribing in the relatively brittle coating material (L_{c1}) as well as on the subsequent fragmentation of its continuous layer and the opening of the substrate (L_{c2}) [36; 37].

The observed differences in macrostresses between the considered coatings on HG40 and HS123 hard alloy substrates, despite their relatively equal coefficients of linear thermal expansion ($5.8\cdot10^{-6}$ and $6.0\cdot10^{-6}$ K^{-1} respectively), owhich determine the thermal component of macrostresses, may be associated with the structural phase (concentration) heterogeneity of the coating material, including the transitional zone between the coating and substrate. Auger spectrometry was employed to analyze the regions adjacent to the coating-substrate interface for the two substrates.

Figure 9 illustrates the concertation profiles of the distribution of elements, which are components of both the substrate and the coating, in boundary regions. From the presented results, it can be inferred that the size of the diffusion region is maximized at the Mo–Ti–Ni–Si–Al–N coating–HS123 alloy composite, with a size of approximately 1.55 µm, compared to its size of approximately 0.82 µm for the HG40 substrate.

The larger size of the diffusion zone in the Mo–Ti–Ni–Si–Al–N coating on HS123 substrate is the reason behind the higher macrostresses detected, primarily due to its concentration constituents. This is further supported by the longer length of the transient zone at the interface between the growing coat-

Table 3. **Macrostresses calculated by the Stoney method achieved in Mo–Ti–Ni–Si–Al–N-coating–substrate composite**

Таблица 3. **Результаты расчета методом Стони макронапряжений, реализующихся в композите «Mo–Ti–Ni–Si–Al–N-покрытие–подложка»**

Substrate	σ_{calc}, GPa	R, m	R_0, m	t_s, 10^{-6} m	t_f, 10^{-6} m	ν_s	E_s, GPa
HG40	–2.9	3.55	1.69	449.67	4.21	0.22	574
HS123	–5.2	4.75	1.08	420.52	4.15	0.21	520

Notations: σ_{calc} – calculated macrostresses; R – substrate curvature radius before application of coating; R_0 – curvature radius of coating–substrate composite; t_s – substrate thickness; t_f – coating thickness; ν_s – Poisson ratio of substrate; E_s – substrate elasticity modulus.

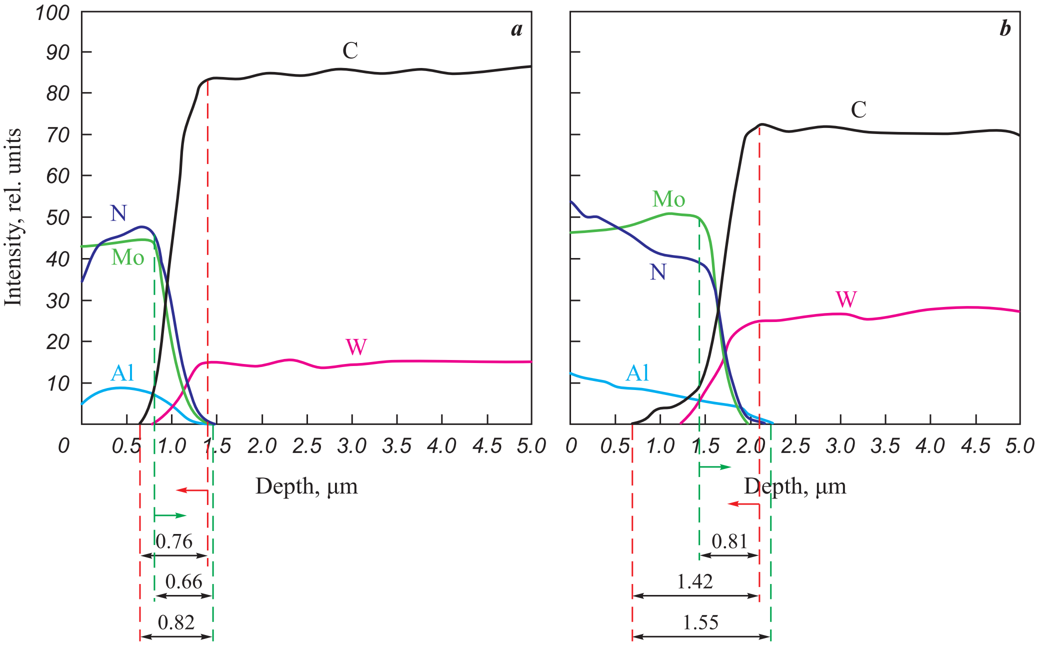

Fig. 9. Distribution of elements in Mo–Ti–Ni–Si–Al–N coating and HG40 (***a***) and HS123 (***b***) substrates at the coating–substrate interfaces

Рис. 9. Распределение элементов покрытия Mo–Ti–Ni–Si–Al–N и подложек ВК10 (***a***) и Т14К8 (***b***) на границах раздела покрытие–подложка

ing and the HS123 substrate. This longer length can be attributed to a local increase in the temperature of this region during the formation of the coating, which is caused by the lower heat conductivity of the HS123 substrate compared to the HG40 substrate [38; 39]. The lower heat conductivity of the HS123 substrate, in comparison that of the HG40 material, approximately 67 W/(m·K), results in insufficient heat removal from the zone of heat release during coating formation. This heat release is caused by the absorption of latent heat released during ion braking, condensation of vapor atoms, and heat transfer by radiation from the vaporizer. As a result, the heat is not effectively dissipated, leading to a localized increase in temperature in the transient zone.

Conclusions

The Mo–Ti–Ni–Si–Al–N hardening coating, characterized by a multilayer architecture with a nanograin structure and crystallite sizes of 6–10 nm, was deposited onto HG40 and HS123 hard alloy substrates using ion plasma vacuum arc deposition. The resulting nano-indentation measurements indicated a hardness of 27.6 GPa and an elasticity modulus of 647 GPa for HG40, accompanied by a relative work of plastic deformation of 38.2 %. Likewise, for HS123, the coating demonstrated a hardness of 34.2 GPa, an elasticity modulus of 481 GPa, and a relative work of plastic deformation of 46.2 %.

The coatings obtained, with roughly equivalent elemental and phase compositions, when applied to diverse hard alloy substrates and meeting the “ten percent” rule in nano-indentation, exhibited distinct physicochemical properties. Specifically, the Mo–Ti–Ni–Si–Al–N coating on the HS123 hard alloy substrate displayed the highest hardness and the lowest wear, along with superior adhesion strength. This phenomenon can be attributed to the achievement of maximum compressive macrostresses within the coating (approximately 5.2 GPa) in this particular case, surpassing the coatings with similar compositions on HG40 substrates (approximately 2.9 GPa). The observed variation in physicochemical properties, despite the relatively small difference in coefficients of linear thermal expansion between the hard alloy substrates, can be attributed to the presence of a diffusion zone of greater length at the interface between the substrate and coating. This diffusion zone, along with accompanying structural phase heterogeneities, influences the magnitude of concentration macrostresses that contribute to the hardening of the coating.

References / Список литературы

1. Pogrebnjak A.D., Eyidi D., Abadias G., Bondar O.V., Beresnev V.M., Sobol O.V. Structure and properties of arc evaporated nanoscale TiN/Mon multilayered systems. *International Journal of Refractory Metals and Hard Materials*. 2015;48:222–228.
https://doi.org/10.1016/j.ijrmhm.2014.07.043

2. Chang H.-W., Huang P.-K., Yeh J.-W., Davison A., Tsau C.-H., Yang C.-C. Influence of substrate bias, deposition temperature and post-deposition annealing on the structure and properties of multi-principal-component (AlCrMoSiTi)N coatings. *Surface and Coatings Technology*. 2008;202(14): 3360–3366.
https://doi.org/10.1016/j.surfcoat.2007.12.014

3. Lai C.-H., Cheng K.-H., Li S.-J., Yeh J.-W. Mechanical and tribological properties of multi-element (AlCrTaTiZr)N coatings. *Surface and Coatings Technology*. 2008;202(15): 3732–3738.
https://doi.org/10.1016/j.surfcoat.2008.01.014

4. Sergevnin V.S., Blinkov I.V., Volkhonskii A.O., Belov D.S., Kuznetsov D.V., Gorshenkov M.V., Skryleva E.A. Wear behaviour of wear-resistant adaptive nano-multilayered Ti–Al–Mo–N coatings. *Applied Surface Science*. 2016;388;Part A:13–23.
https://doi.org/10.1016/j.apsusc.2016.06.102

5. Vereschaka A., Grigoriev S., Sitnikov N., Batako A. Delamination and longitudinal cracking in multi-layered composite nanostructured coatings and their influence on cutting tool life. *Wear*. 2017;390–391:209–219.
https://doi.org/10.1016/j.wear.2017.07.021

6. Blinkov I.V., Volkhonskii A.O., Chernogor A.V., Sergevnin V.S., Belov D.S., Polyanskii A.M. Structure, composition, and properties of Arc PVD Mo–Si–Al–Ti–Ni–N coatings. *Inorganic Materials*. 2018;54(5):437–445.
https://doi.org/10.1134/S0020168518050023

Блинков И.В., Волхонский А.О., Черногор А.В., Сергевнин В.С., Белов Д.С., Полянский А.М. Структура, состава и свойства ионно-плазменных вакуумно-дуговых покрытий Mo–Si–Al–Ti–Ni–N. *Неорганические материалы*. 2018;54(5):458–466.
https://doi.org/10.7868/S0002337X18050056

7. Leyland A., Matthews A. On the significance of the *H*/*E* ratio in wear control: A nanocomposite coating approach to optimized tribological behavior. *Wear*. 2000;246(1-2): 1–11. https://doi.org/10.1016/S0043-1648(00)00488-9

8. Tsui T.Y., Pharr G.H., Oliver W.C., White W.C. Nanoindentation and nanoscratching of hard carbon coatings for magnetic disks. *MRS Online Proceedings Library*. 1995;383(1):447–452.
https://doi.org/10.1557/PROC-383-447

9. Veprek S., Holubar P., Veprek-Heijman M. Industrial applications of hard and superhard nanocomposite coatings on tools for machining, forming, stamping and injection molding. *Advanced Materials Research*. 2016;1135:218–233.
https://doi.org/10.4028/www.scientific.net/AMR.1135.218

10. Fox-Rabinovich G., Yamamoto K., Beake B., Gershman I., Kovalev A., Veldhuis S., Aguirre M., Dosbaeva G., Endrino J. Hierarchical adaptive nanostructured PVD coatings for extreme tribological applications: the quest for nonequilibrium states and emergent behavior. *Science and Technology of Advanced Materials*. 2012;13(4):043001.
https://doi.org/10.1088/1468-6996/13/4/043001

11. Sergevnin V.S., Blinkov I.V., Belov D.S., Smirnov N.I., Volkhonskii A.O., Kuptsov K.A. Wear and erosion of arc-PVD multilayer Ti–Al–Mo–N coatings under various conditions of friction and loading. *The International Journal of Advanced Manufacturing Technology*. 2018;98(1): 593–601. https://doi.org/10.1007/s00170-018-2235-z

12. Shima M., Okado J., McColl I.R., Waterhouse R.B., Hasegawa T., Kasaya M. The influence of substrate material and hardness on the fretting behaviour of TiN. *Wear*. 1999;225-229:38–45.
https://doi.org/10.1016/S0043-1648(99)00062-9

13. Drábik M., Truchlý M., Ballo V., Roch T., Kvetková L., Kúš P., Influence of substrate material and its plasma pretreatment on adhesion and properties of WC/a-C:H nanocomposite coatings deposited at low temperature. *Surface and Coatings Technology*. 2018;333:138–147.
https://doi.org/10.1016/j.surfcoat.2017.10.081

14. Seidl W.M., Bartosik M., Kolozsvári S., Bolvardi H., Mayrhofer P. H. Influence of coating thickness and substrate on stresses and mechanical properties of (Ti,Al,Ta)N/(Al,Cr)N multilayers. *Surface and Coatings Technology*. 2018;347:92–98.
https://doi.org/10.1016/j.surfcoat.2018.04.060

15. Kagnaya T., Boher C., Lambert L., Lazard M., Cutard T. Wear mechanisms of WC–Co cutting tools from high-speed tribological tests. *Wear*. 2009;267(5-8):890–897.
https://doi.org/10.1016/j.wear.2008.12.035

16. Weidow J., Zackrisson J., Jansson B., Andréna H.-O. Characterisation of WC–Co with cubic carbide additions. *International Journal of Refractory Metals and Hard Materials*. 2009;27(2):244–248.
https://doi.org/10.1016/j.ijrmhm.2008.11.007

17. Oliver W.C., Pharr G.M., An improved technique for determining hardness and elastic modulus. *Journal of Materials Research*. 1992;7(6):1564–1583.
https://doi.org/10.1557/JMR.1992.1564

18. Stoney G.G. The tension of metallic films deposited by electrolysis. *Proceedings of the Royal Society A*. 1909;82(553):172–175.
https://doi.org/10.1098/rspa.1909.0021

19. Pureza J.M., Lacerda M.M., De Oliveira A.L., Fragalli J.F., Zanon R.A.S. Enhancing accuracy to Stoney equation. *Applied Surface Science*. 2009;255(12):6426–6428.
https://doi.org/10.1016/j.apsusc.2009.01.097

20. Blinkov I.V., Volkhonskii A.O., Belov D.S., Sergevnin V.S., Chernogor A.V., Kiseleva T.V., Bondarev A.V. Superhard nanostructured ceramic–metal coatings with a low macrostress level. *Technical Physics Letters*. 2018;44(2): 167–169. https://doi.org/10.1134/S1063785018020165

Блинков И.В., Волхонский А.О., Белов Д.С., Сергевнин В.С., Черногор А.В., Киселева Т.В., Бондарев А.В. Высокотвердые наноструктурные керамико-металлические покрытия с низким уровнем макронапряжений. *Письма в журнал технической физики*. 2018;(4):80–86.
http://dx.doi.org/10.21883/PJTF.2018.04.45642.17083

21. Shiri S., Ashtijoo P., Odeshi A., Yang Q. Evaluation of Stoney equation for determining the internal stress of DLC thin films using an optical profiler. *Surface and Coatings Technology*. 2016;308:98–100.
http://dx.doi.org/10.1016/j.surfcoat.2016.07.098

22. Chernogor A.V., Blinkov I.V., Belov D.S., Sergevnin V.S., Volkhonskii A.O. Analysis of the structure of multilayer nanocrystalline coatings based on plasma mass transfer parameters calculated by the monte carlo method. *Technical Physics Letters*. 2019;45(2):75–81. https://doi.org/10.1134/S1063785019020056

Черногор А.В., Блинков И.В., Белов Д.С., Сергевнин В.С., Волхонский А.О. Анализ структуры многослойных нанокристаллических покрытий на основе параметров массопереноса плазмы, вычисленных методом Монте-Карло. *Письма в журнал технической физики*. 2019;(3):16–20. http://dx.doi.org/10.21883/PJTF.2019.03.47265.17575

23. Bertóti I. Characterization of nitride coatings by XPS. *Surface and Coatings Technology*. 2002;151-152:194–203. https://doi.org/10.1016/S0257-8972(01)01619-X

24. Crist B.V. Handbook of the elements and native oxides. California: LLC XPS International, 1999. 560 p.

25. Sanjines R., Wiemer C., Almeida J., Levy F. Valence band photoemission study of the Ti–Mo–N system. *Thin Solid Films*. 1996;290-291:334–338. https://doi.org/10.1016/S0040-6090(96)09082-7

26. Wang T., Zhang G., Ren S., Jiang B. Effect of nitrogen flow rate on structure and properties of MoN_x coatings deposited by facing target sputtering, *Journal of Alloys and Compounds*. 2017;701:1–8. http://dx.doi.org/10.1016/j.jallcom.2017.01.077

27. Pharr G.M., Oliver W.C. Measurement of thin-film mechanical properties using nanoindentation. *MRS Bulletin*. 1992;17(7):28–33. https://doi.org/10.1557/S0883769400041634

28. Mayrhofer P.H., Mitterer C., Hultman L., Clemens H. Microstructural design of hard coatings. *Progress in Materials Science*. 2006;51(8):1032–1114. https://doi.org/10.1016/j.pmatsci.2006.02.002

29. Veprek S., Veprek-Heijman M.G.J., Karvankova P., Prochazka J. Different approaches to superhard coatings and nanocomposites. *Thin Solid Films*. 2009;476(1):1–29. https://doi.org/10.1016/j.tsf.2004.10.053

30. Kulikovsky V., Bohac P., Franc F., Deineka A., Vorlicek V., Jastrabik L. Hardness, intrinsic stress, and structure of the a-C and a-C:H films prepared by magnetron sputtering. *Diamond and Related Materials*. 2001;10(3-7):1076–1081. https://doi.org/10.1016/S0925-9635(00)00525-2

31. Mayrhofer P.H., Tischler G., Mitterer C. Microstructure and mechanical/thermal properties of Cr–N coatings by reactive unbalanced magnetron sputtering. *Surface and Coatings Technology*. 2001;142–144:78–84. https://doi.org/10.1016/S0257-8972(01)01090-8

32. Mayrhofer P.H., Kunc F., Musil J., Mitterer C. A compatarive study on reactive and nonreactive unbalanced magnetron sputter deposition of TiN coatings. *Thin Solid Films*. 2001;415(1–2):151–159. https://doi.org/10.1016/S0040-6090(02)00511-4

33. Rickerby D.S. Internal stress and adherence of titanium nitride coatings. *Journal of Vacuum Science & Technology A*. 1986;4(6):2809–2814. https://doi.org/10.1116/1.573683

34. Window B., Harding G.L., Horrigan C., Bell T. Stress and microhardness in sputter deposited molybdenum and chromium films. *Journal of Vacuum Science & Technology A*. 1992;10(5):3278–3282. https://doi.org/10.1116/1.577855

35. Jaroš M., Musil J., Haviar S. Interrelationships among macrostress, microstructure and mechanical behavior of sputtered hard Ti(Al,V)N films. *Materials Letters*. 2019;235:92–96. https://doi.org/10.1016/j.matlet.2018.09.173

36. Wang Q., Zhou F., Zhou Z., Li L. K.-Y., Yan J. An investigation on the crack resistance of CrN, CrBN and CrTiBN coatings via nanoindentation. *Vacuum*. 2017;145:186–193. https://doi.org/10.1016/j.vacuum.2017.08.041

37. Vereschaka A.A., Grigoriev S.N. Study of cracking mechanisms in multi-layered composite nano-structured coatings. *Wear*. 2017;378-379:43–57. http://dx.doi.org/10.1016/j.wear.2017.01.101

38. Davis J.R. Tool materials: ASM Specialty Handbook. ASM International, 1995. 501 p.

39. Schultrich B., Poeβnecker W., Thermal conductivity of cemented carbides. *Journal of Thermal Analysis and Calorimetry*. 1998;33(1):305–310. https://doi.org/10.1007/BF01914616

Information about the Authors

Viktor S. Sergevnin – Cand. Sci. (Eng.), Master of Teaching, Department of Functional Nanosystems and High-Temperature Materials, National University of Science and Technology "MISIS" (NUST MISIS).
ORCID: 0000-0002-4007-435X
E-mail: v.s.sergevnin@gmail.com

Igor V. Blinkov – Dr. Sci. (Eng.), Professor, Department of Functional Nanosystems and High-Temperature Materials, NUST MISIS.
ORCID: 0000-0001-8619-6259
E-mail: biv@misis.ru

Dmitry S. Belov – Cand. Sci. (Eng.), Master of Teaching, Department of Functional Nanosystems and High-Temperature Materials, NUST MISIS.
ORCID: 0000-0002-7053-5540
E-mail: dm.blv@yandex.ru

Сведения об авторах

Виктор Сергеевич Сергевнин – к.т.н., учебный мастер кафедры функциональных наносистем и высокотемпературных материалов, Национальный исследовательский технологический университет «МИСИС» (НИТУ МИСИС).
ORCID: 0000-0002-4007-435X
E-mail: v.s.sergevnin@gmail.com

Игорь Викторович Блинков – д.т.н., профессор кафедры функциональных наносистем и высокотемпературных материалов, НИТУ МИСИС.
ORCID: 0000-0001-8619-6259
E-mail: biv@misis.ru

Дмитрий Сергеевич Белов – к.т.н., учебный мастер кафедры функциональных наносистем и высокотемпературных материалов, НИТУ МИСИС.
ORCID: 0000-0002-7053-5540
E-mail: dm.blv@yandex.ru

Alexander P. Demirov – Laboratory Assistant-Researcher, Department of Functional Nanosystems and High-Temperature Materials, NUST MISIS.
ORCID: 0000-0002-5014-2993
E-mail: apdemirov@gmail.com

Aleksey V. Chernogor – Master of Teaching, Department Functional Nanosystems and High-Temperature Materials, NUST MISIS.
ORCID: 0000-0001-5385-5369
E-mail: avchernogor@gmail.com

Tamara A. Lobova – Dr. Sci. (Eng.), Professor, Export Control Specialist, NUST MISIS.
E-mail: smazka39@mail.ru

Alexander I. Laptev – Dr. Sci. (Eng.), Chief Researcher, Research Laboratory of Superhard Materials, NUST MISIS.
E-mail: laptev@misis.ru

Александр Павлович Демиров – лаборант-исследователь кафедры функциональных наносистем и высокотемпературных материалов, НИТУ МИСИС.
ORCID: 0000-0002-5014-2993
E-mail: apdemirov@gmail.com

Алексей Витальевич Черногор – учебный мастер кафедры функциональных наносистем и высокотемпературных материалов, НИТУ МИСИС.
ORCID: 0000-0001-5385-5369
E-mail: avchernogor@gmail.com

Тамара Александровна Лобова – д.т.н., профессор, специалист по экспортному контролю, НИТУ МИСИС.
E-mail: smazka39@mail.ru

Александр Иванович Лаптев – д.т.н., гл. науч. сотрудник научно-исследовательской лаборатории сверхтвердых материалов, НИТУ МИСИС.
E-mail: laptev@misis.ru

Contribution of the Authors

V. S. Sergevnin – formulated a the basic concept, formulated the purpose and objectives of the study, prepared the manuscript, formulated conclusions, studied the structure and composition of coatings and macrostressed state of samples with coatings.
I. V. Blinkov – scientific advising, edited the manuscript and conclusions.
D. S. Belov – analyzed the research results, prepared the illustrative material, conducted experiments on the physicomechanical properties of coatings.
A. P. Demirov – conducted research on the structure and composition of coatings, provided resources.
A. V. Chernogor – conducted experiments on deposition of coatings.

T. A. Lobova – conducted tribological studies of samples with coatings.
A. I. Laptev – studied the adhesive strength of coatings with carbide substrate.

Вклад авторов

В. С. Сергевнин – формирование основной концепции, постановка цели и задачи исследования, подготовка текста, формулирование выводов, проведение исследований макронапряженного состояния образцов с покрытиями.
И. В. Блинков – научное руководство, редактирование текста и выводов.
Д. С. Белов – анализ результатов исследований, подготовка иллюстративного материала, проведение экспериментов по изучению физико-механических свойств покрытий.
А. П. Демиров – проведение исследований структуры и состава покрытий, обеспечение ресурсами.
А. В. Черногор – проведение экспериментов по осаждению покрытий.
Т. А. Лобова – проведение трибологических исследований образцов с покрытиями.
А. И. Лаптев – исследования адгезионной прочности покрытий с твердосплавной подложкой.

Received 24.03.2023
Revised 19.04.2023
Accepted 21.04.2023

Статья поступила 24.03.2023 г.
Доработана 19.04.2023 г.
Принята к публикации 21.04.2023 г.

Nanostructured Materials and Functional Coatings
Наноструктурированные материалы и функциональные покрытия

UDC 621.793

https://doi.org/10.17073/1997-308X-2023-3-67-78

Research article
Научная статья

TaC-based wear-resistant coatings obtained by magnetron sputtering and electro-spark deposition for wedge gate valve protection

A. D. Sytchenko[1], **M. N. Fatykhova**[1], **V. P. Kuznetsov**[2] , **K. A. Kuptsov**[1],
M. I. Petrzhik[1], **A. E. Kudryashov**[1], **Ph. V. Kiryukhantsev-Korneev**[1]

[1] **National University of Science and Technology "MISIS"**
4 bld. 1 Leninskiy Prosp., Moscow 119049, Russia
[2] **Ural Federal University named after the First President of Russia B.N. Yeltsin**
19 Mira Str., Yekaterinburg 620002, Russia

✉ alina-sytchenko@yandex.ru

Abstract. Ta–Zr–Si–B–C coatings were deposited by magnetron sputtering (MS) of a $TaSi_2$–Ta_3B_4–$(Ta, Zr)B_2$ multi-component target in an Ar + C_2H_4 gas mixture. TaC–Cr–Mo–Ni based coatings were obtained by electro-spark deposition (ESD) using TaC–Cr–Mo–Ni electrode. The composition and structure of the coatings were studied using scanning electron microscopy, energy-dispersive spectroscopy, glow discharge optical emission spectroscopy and *X*-ray diffraction. Mechanical and tribological properties of coatings were determined using nanoindentation and pin-on-disk tests. The study showed that the coatings have a homogeneous and defect-free structure, with the main structural component being the fcc-TaC phase. The MS coating exhibited a 30 % higher concentration of the TaC phase compared to the ESD coating. The TaC crystallite sizes for the MS and ESD coatings were 3 and 30 nm, respectively. The presence of a high fraction of the carbide phase and small crystallite size for the MS coating resulted in superior hardness ($H = 28$ GPa) compared to the ESD sample ($H = 10$ GPa). Both coatings exhibited similar values of the friction coefficient (about 0.15) and demonstrated reduced wear rates ($<10^{-7}$ $mm^3/(N{\cdot}m)$). The deposition of coatings on a steel substrate led to a decrease in the friction coefficient by five times and the wear rate by four orders of magnitude. Pilot tests were conducted on coatings applied to wedge gate valve of shut-off devices used in the oil and gas industry for pumping liquids. The results indicated that the service life of the steel wedge gate valve increased by 25 and 70 % with deposited MS and ESD coatings, respectively.

Keywords: magnetron sputtering, electro-spark deposition, coatings, TaC, friction coefficient, wear resistance

Acknowledgements: This work was performed with financial support by Russian Science Foundation (project no. 23-49-00141).

For citation: Sytchenko A.D., Fatykhova M.N., Kuznetsov V.P., Kuptsov K.A., Petrzhik M.I., Kudryashov A.E., Kiryukhantsev-Korneev Ph.V. TaC-based wear-resistant coatings obtained by magnetron sputtering and electro-spark deposition for wedge gate valve protection. *Powder Metallurgy and Functional Coatings*. 2023;17(3):67–78. https://doi.org/10.17073/1997-308X-2023-3-67-78

Покрытия на основе карбида тантала, полученные методами магнетронного распыления и электроискрового легирования, для повышения износостойкости деталей запорной арматуры

А. Д. Сытченко[1] ✉, М. Н. Фатыхова[1], В. П. Кузнецов[2], К. А. Купцов[1], М. И. Петржик[1], А. Е. Кудряшов[1], Ф. В. Кирюханцев-Корнеев[1]

[1] **Национальный исследовательский технологический университет «МИСИС»**
Россия, 119049, г. Москва, Ленинский пр-т, 4 стр. 1
[2] **Уральский федеральный университет имени первого Президента России Б.Н. Ельцина**
Россия, 620075, г. Екатеринбург, ул. Мира, 19

✉ alina-sytchenko@yandex.ru

Аннотация. Покрытия Ta–Zr–Si–B–C осаждались методом магнетронного распыления (МР) многокомпонентной мишени $TaSi_2$–Ta_3B_4–(Ta, Zr)B_2 в среде Ar + C_2H_4. Покрытия на основе TaC–Fe–Cr–Mo–Ni были получены путем электроискрового легирования (ЭИЛ) с использованием электрода TaC–Cr–Mo–Ni. Состав и структура покрытий исследовались с помощью сканирующей электронной микроскопии, энергодисперсионной спектроскопии, оптической эмиссионной спектроскопии тлеющего разряда и рентгенофазового анализа. Механические характеристики определялись методом наноиндентирования. Трибологические свойства исследовались на машине трения в режиме возвратно-поступательного движения. Выявлено, что покрытия обладают однородной бездефектной структурой и основной структурной составляющей является ГЦК-фаза TaC. Ее концентрация в МР-покрытии на 30 % выше, чем в ЭИЛ- покрытии. Размеры кристаллитов TaC для МР- и ЭИЛ-покрытий составляли 3 и 30 нм соответственно. Высокая доля карбидной фазы и малый размер кристаллитов обеспечили более высокую твердость МР-покрытия (H = 28 ГПа) по сравнению с ЭИЛ-образцом (H = 10 ГПа). Покрытия характеризовались близкими значениями коэффициента трения (около 0,15) и приведенного износа ($<10^{-7}$ мм^3/(Н·м)). Осаждение на стальную подложку привело к снижению коэффициента трения в 5 раз и приведенного износа на 4 порядка. Проведены опытно-промышленные испытания покрытий, осажденных на клиновые задвижки запорной арматуры для перекачки жидкости, используемые в нефтегазовой промышленности. Результаты испытаний показали, что ресурс работы стальной клиновой задвижки возрос на 25 и 70 % при осаждении МР- и ЭИЛ-покрытий соответственно.

Ключевые слова: магнетронное распыление (МР), электроискровое легирование (ЭИЛ), покрытия, TaC, коэффициент трения, износостойкость

Благодарности: Работа выполнена при финансовой поддержке Российского научного фонда (проект № 23-49-00141).

Для цитирования: Сытченко А.Д., Фатыхова М.Н., Кузнецов В.П., Купцов К.А., Петржик М.И., Кудряшов А.Е., Кирюханцев-Корнеев Ф.В. Покрытия на основе карбида тантала, полученные методами магнетронного распыления и электроискрового легирования, для повышения износостойкости деталей запорной арматуры. *Известия вузов. Порошковая металлургия и функциональные покрытия*. 2023;17(3):67–78. https://doi.org/10.17073/1997-308X-2023-3-67-78

Introduction

One of the problems that modern production faces is the wear of parts and metal structures during operation. To enhance wear resistance and extend the service life of these components, a viable approach involves modifying only the surface of the products through the application of protective coatings. Two prominent coating deposition technologies, electro-spark deposition (ESD) [1] and magnetron sputtering (MS) [2] are promising coating deposition technologies in demand in the industry.

ESD is based on the phenomenon of electric erosion occurring during spark discharge, which leads to the transfer of erosion products from the electrode surface to the substrate. This method offers several advantages, including high adhesion, the ability to perform localized surface treatment, minimal thermal impact on the substrate, and relaxed requirements for surface preparation before application [3–5]. On the other hand, the technology of MS involves coating formation through atomic fluxes during vacuum atomization of the cathode material, facilitated by the flow of anomalous glow discharge. This method is characterized by its versatility in working with various substrates, and the resulting coatings demonstrate a low concentration of defects, a dense homogeneous structure, and a uniform distribution of elements throughout the coating's thickness [6–8].

Until recently, the utilization of ESD and MS techniques had primarily been confined to applications within the domain of metalworking tools, encompassing cutting, stamping, or rolling tools. The effectiveness of the ESD approach in enhancing the durability of tools such as rolling mills [9], drills [10] and stamps [11] is noteworthy. Similarly, the favorable outcomes of employing MS coatings have been documented in the reinforcement of components like punches [12], cold rolling rollers [13], cutting lathe plates, end mills [14–16], and stamps [17].

In recent years, the range of applications for strengthening protective coatings through ESD and MS processes has significantly broadened. Notably, efforts have been directed towards the application of MS coatings to heat-generating element pipes [18; 19] and boiler components for biomass combustion [20]. ESD coatings have exhibited impressive performance when utilized on blades within the high-temperature zone of gas turbine engines [21], gas turbines within thermal and nuclear power plants [22], as well as on bearings [23], components of internal combustion engines [24], elements of power hydraulic cylinders [25], pumps within tractor hydraulic systems and agricultural machinery [26], and marine infrastructure installations [27], among others. Additionally, the application of ESD coatings to rods of hydraulic cylinders for drilling pumps [28] has shown promising outcomes.

The potential effectiveness of the MS and ESD methods finds applicability in a range of objects, including components within isolation valves employed within the oil and gas sector. These components are susceptible to significant wear resulting from abrasion and the impact of abrasive particles. The wear endured by these valve components stands as a prevalent cause of equipment malfunctions and incidents [29]. The matter of intensified wear and ensuing failures of these elements is explored in scholarly works [30; 31]. A remedy to address this challenge lies in the coating of isolation valve components. Metallic coatings (Zn, Cu, Al–Cr) applied through galvanic and ion-plasma techniques, as well as via plasma sputtering and laser cladding, have been examined in this context. These investigations have indicated the potential of utilizing coatings characterized by heightened density and enhanced resistance to corrosion [32]. Numerous strategies aimed at extending the operational life of isolation valve elements through ion-plasma technologies, particularly MS, have been detailed in [33].

Tantalum carbide is emerging as a promising material for electrode applications in both magnetron sputtering and electro-spark deposition methods. It finds application as a protective coating due to its notable properties: high hardness (from 25 to 45 GPa), elastic modulus (300–450 GPa), resistance to abrasion, corrosion and oxidation, as well as excellent thermal stability (up to 2000 °C) [34; 35]. To mitigate the propensity of TaC to exhibit brittle behavior under loading and the potential for fracture due to cracking, binary coatings are imbued with specific elements. These elements include:

– elements that demonstrate solubility within the basic phase (Cr, Mo, V, Ni, Zr, etc.). The integration of these elements significantly enhances the properties of base coatings by inducing lattice deformation through the creation of new solid solutions [36];

– amorphous elements like Si and B, which play a pivotal role in reshaping the structure of the coating. This leads to the formation of a nanocomposite characterized by superior mechanical properties, wear and corrosion resistance [37–39].

The objective of this study was to generate wear-resistant coatings using tantalum carbide as a foundation, employing both magnetron sputtering and electro-spark deposition techniques. These coatings were intended to provide protection for components utilized in isolation valves.

Experimental

Ta–Zr–Si–B–C coatings were deposited by magnetron sputtering using a $TaSi_2$–Ta_3B_4–(Ta, Zr)B_2 ceramic target (composition, wt. %: 70.8 Ta, 18.6 Si, 7.4 Zr and 2.9 B). The target with a diameter of 120 mm and a thickness of 6 mm, was produced by hot pressing of milled products obtained from self-propagating high-temperature synthesis [40]. The coatings were deposited using a UVN-2M vacuum installation (AO Quartz, Russia) [41]. The magnetron was powered by a Pinnacle+ 5×5 source (Advanced Energy, USA). Power, voltage and current parameters were 1 kW, 500 V and 2 A, respectively. The coatings were applied in an Ar + C_2H_4 gas mixture, where Ar (99.9995 %) and C_2H_4 (99.95 %) gases were used. The gas flow rate was controlled by gas supply system (Eltochpribor, Russia), maintained a flow rate of 15 sccm Ar and 10 sccm C_2H_4. The operating conditions were a residual pressure of $\sim 10^{-3}$ Pa and a working gas pressure of 0.1–0.2 Pa. The deposition procedure was carried out for 40 min.

The vacuum electro-spark deposition method [36; 42] was employed to administer a TaC–Cr–Mo–Ni coating, using a TaC–Fe–Cr–Mo–Ni electrode. The preparation of electrodes involved the cold pressing of powders: Cr grade RN-1S (particle size fraction <60 μm), Ni (PNK-0T2, <20 μm), Mo (PM99.95, <5 μm) and TaC (MRTU 9-09-03443-77, <5 μm). The powders were blended in specified proportions (wt. %: 67.5%TaC–12.5%Mo–7.5%Ni–12.5%Cr) using a planetary mill, Activator-4M (Russia). The application of coatings was carried out under the subsequent technological conditions:

– electrode rotation speed 1000 rpm;
– electrode scanning rat 500 mm/min;
– scanning step 0.5 mm;
– electrical pulse frequency 100 Hz;
– pulse voltage 100 V;
– pulse duration 50 μs;

– working pressure within the vacuum chamber 0.5 Pa;

– application medium – Ar.

Model substrates for coating deposition consisted of PH1 steel discs (wt. %: 77.2%Fe–14.6%Cr–3.8%Ni–3.6%Cu–0.8%Si) measuring 45 mm in diameter. Coatings were also applied onto the wedge and seats of wedge gate valves composed of PH1 steel. Prior to coating, the substrates underwent cleaning in isopropyl alcohol using a UZDN-2T unit (Russia), operating at a frequency of 22 kHz for 5 min. Preceding the application of coatings via the MS method, the substrates were further cleaned in a vacuum environment using an ion source (Ar^+ ions, 2 keV) for a duration of 20 min.

The coatings elemental composition and structure were studied using the following methods:

– scanning electron microscopy (SEM) employing an S-3400 microscope (Hitachi, Japan) equipped with a Noran-7 Thermo attachment for energy dispersive spectroscopy (EDS);

– glow discharge optical emission spectroscopy (GDOES) using a Profiler 2 installation (Horiba JY, France);

– *X*-ray diffraction (XRD) employing a D2 Phaser diffractometer (Bruker, Germany).

The mechanical properties of the coatings were determined using nanoindentation carried out with a precision Nano-hardness tester (CSM Instruments, Switzerland) equipped with a Berkovich indenter at a load of 8 mN.

For the purpose of tribological assessment, coatings and steel substrates underwent testing at Tribometer (CSM Instruments, Switzerland), equipped with a reciprocating module. When using a steel counterbody, intensive sticking of wear products to the surface of a harder coating occurs, which makes it difficult to assess wear resistance [43]. Test parameters included a load of 2 N, linear velocity of 0.3 cm/s and 300 cycles. Wear tracks of the coatings were examined through optical profilometry, utilizing a WYKO NT1100 instrument (Veeco, USA). The wear areas of the counterbody were analyzed using an Axiovert 25 optical microscope (Carl Zeiss, Germany). The calculation of reduced wear values for both the coatings and counterbody followed the methodology detailed in [44].

Pilot tests were conducted to assess the tightness of the steel gate valve with a rising spindle, featuring a coating applied on the wedge and seats of the locking mechanism. The tests were carried out on a certified stand in compliance with the State Standard GOST 33257 and Specifications TU 3741-001-22986183-2009. The testing took place on a certified test bench utilizing precision control instruments. The testing was performed using water as the testing medium at a temperature of 20 ± 5 °C, with a pressure of 18.0 MPa. The tests were carried out continuously until the maximum number of "open-close" cycles was reached, as determined by the criterion indicating the onset of valve leakage (loss of tightness).

Results and discussion

Table 1 provides the elemental composition and coating thickness details. The MS coating contains a higher content of TaC (45 at. %), which is 30 % more than the carbide phase content in the ESD coating (32 at. %).

Figures 1, *a*, *b* show cross sections SEM images and XRD patterns of the MS and ESD coatings. These images show a homogeneous and defect-free microstructure. The coating thickness was measured as 7 μm for MS and 54 μm for ESD coatings. In the ESD coating, tantalum carbide particles uniformly distributed throughout the entire volume, were observed. These particles had sizes up to 0.2 μm and were embedded in an iron-based metal matrix containing alloyed by Cr, Ni, and Mo. Additionally, localized areas featured larger TaC grains, measuring up to 5 μm. The initial roughness of the ESD coating was determined as R_a = 2.2 μm, while that of the MS coating was 15 nm.

The XRD patterns of the MS and ESD coatings show peaks at 2θ = 34.9, 40.5 and 58.6°, corresponding to the (111), (200), and (220) planes of the TaC FCC phase (JCPDS 89–3831) (as shown in Fig. 1, *c*).

The broadened peaks observed in the MS coating suggest the existence of an amorphous matrix around $TaSi_2$, with the inclusion of zirconium and boron in a dissolved state [38]. In the XRD pattern of the ESD coating, supplementary peaks at positions 44.5 and 64.8° correspond to a solid solution founded on alpha iron α-Fe(Cr, Ni, Mo). The crystallite size of the TaC phase, deduced from the most prominent line (111), was ~3 nm for the MS coating and ~30 nm for the ESD coating. For the MS coating the lattice parameter (*a*) was measured at 0.447 nm, whereas it was 0.441 nm for the ESD coating. This slightly deviates from the value

Table 1. **Elemental composition and thickness of coating**

Таблица 1. **Элементный состав и толщина покрытий**

Sample	Elemental composition, at. %									Thickness, μm
	Ta	C	Si	B	Zr	Mo	Ni	Fe	Cr	
MS	22	31	21	18	8	–	–	–	–	7
ESD	16	18	–	–	–	3	2	50	11	54

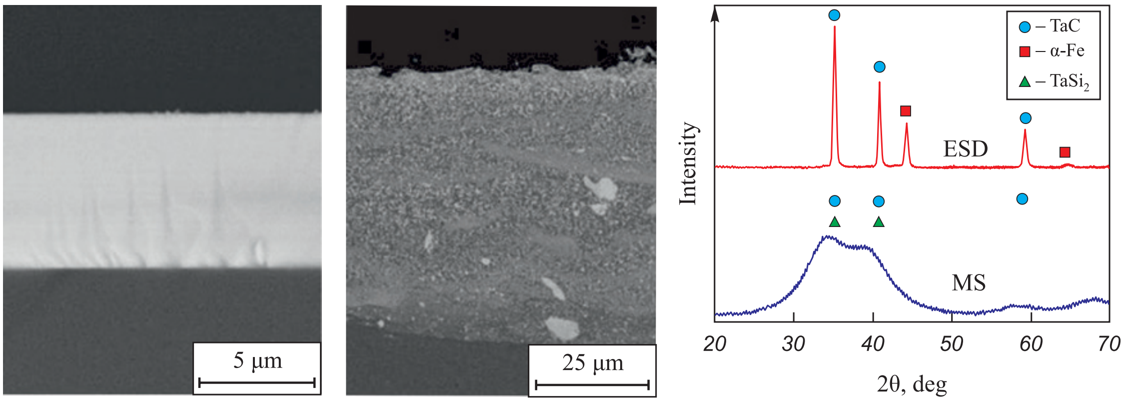

a ***b*** ***c***

Fig. 1. Cross-section SEM images of MS (***a***) and ESD (***b***) coatings and XRD patterns of coatings (***c***)

Рис. 1. СЭМ-микрофотографии поперечных шлифов покрытий, полученных МР (***a***) и ЭИЛ (***b***), и их рентгенограммы (***c***)

of $a = 0.445$ nm, established for the TaC powder standard (JCPDS 89-3831 card). Such variation could be attributed to the presence of compressive stresses (for the MS coating) [45] and tensile stresses (for ESD) [46], or a divergence in the composition of the TaC phase from its stoichiometric state [47].

The mechanical properties of the coatings and substrate, including hardness (H), Young's modulus (E) and elastic recovery (W) are shown in Table 2.

The enhanced mechanical properties exhibited by the MS coating could be attributed to its significant content of the hard carbide phase TaC [49; 50] as well as its finely crystalline structure [38; 51; 52].

Both the ESD and MS coatings demonstrated consistently low coefficients of friction, measuring $\mu = 0.15$ (as illustrated in Figure 2, *a*, and detailed in Table 2). Conversely, for the steel substrate, the friction coefficient (μ) displayed a gradual increase from

Table 2. **Mechanical and tribological characteristics of coatings and substrate**

Таблица 2. **Механические и трибологические характеристики покрытий и подложки**

Sample	H, GPa	E, GPa	W, %	μ	V_w, mm³/(N·m)	
					Coating	Counterbody
MS	28±1	288±5	76±2	0.15	$<10^{-7}$	Sticking
ESD	10±1	278±4	33±1	0.15	$<10^{-7}$	$4.7\cdot10^{-7}$
Steel, Grade PH1	4^*	200^*	–	0.73	$1.2\cdot10^{-3}$	Sticking
* Reference data [48].						

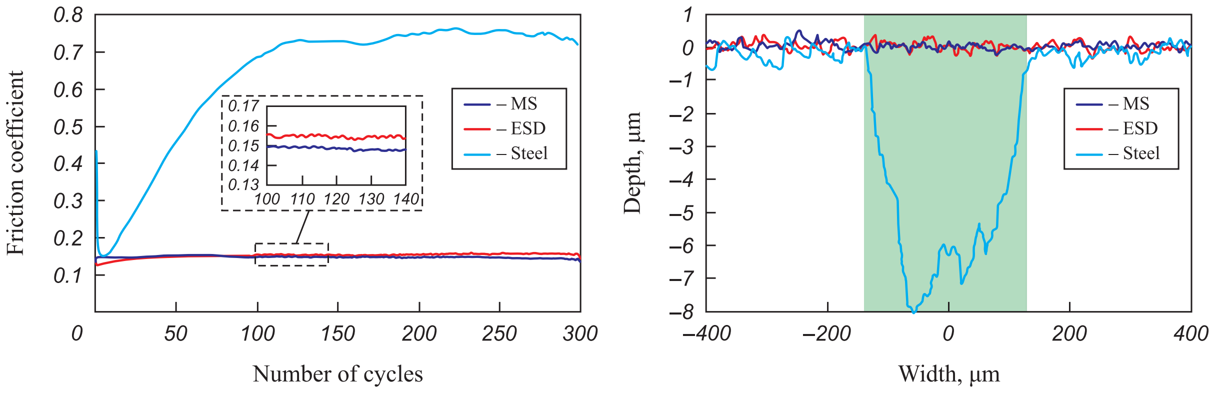

a ***b***

Fig. 2. Friction coefficient depending on the number of cycles (***a***) and 2D profiles of wear tracks (***b***) for coatings and steel substrate

Рис. 2. Зависимость коэффициента трения от количества циклов (***a***) и двухмерные профили дорожек износа (***b***) покрытий и стальной подложки

0.17 to 0.65 during the initial 120 cycles. Following the initial wear-in phase, the friction coefficient stabilized at 0.73. Consequently, the deposition of MS and ESD coatings reduced this parameter by 5 times compared to a steel substrate. This reduced friction coefficient exhibited might be attributed to the beneficial effect of free carbon, which in certain circumstances can be released during the oversaturation of the crystalline carbide phase. This unbound carbon could function as a solid lubricant during friction [53].

In Fig. 2, *b* 2D profiles of wear tracks are presented. The track depth for both MS and ESD coatings remained within the range of surface roughness and did not exceed 150 nm. Conversely, for the steel substrate, the track depth measured 8 μm. The reduced wear (V_w), calculated from these profiles, was below 10^{-7} mm^3/(N·m) for both MS and ESD coatings, while for the steel substrate, it was $1.2 \cdot 10^{-3}$ mm^3/(N·m) (as indicated in Table 2). Notably, the application of MS and ESD coatings substantially enhanced the wear resistance of the steel substrate.

Micrographs of the tribological contact zones on the surface of the Al_2O_3 ball are depicted in Figure 3. In the instance of the MS coating and the steel substrate, a slight sticking of wear products was identified, making it challenging to precisely determine the V_w values for the counterbody. On the other hand, for the ESD coating, the contact area is free from sticking. In this particular scenario, the reduced wear of the Al_2O_3 ball was $4.7 \cdot 10^{-7}$ mm^3/(N·m).

Tests conducted on a steel wedge gate valve revealed that the number of operational cycles before valve leakage for components with MS and ESD coatings reached 3750 and 5100 cycles, respectively. In contrast, steel components managed to withstand only up to 3000 cycles before experiencing leakage. This indicates that the application of MS and ESD coatings extends the service life of a steel wedge valve by 25 and 70 %, respectively.

Fig. 4, *a* presents the appearance of parts coated with MS, along with SEM micrographs of tribological contact regions following pilot tests. Scratches were evident on the part's surface within the tribological contact area, signifying the abrasive nature of wear. Based on SEM and EDS data, three distinct zones can be identified along the inner edges of the tribological contact segments:

1 – corresponds to the original MS coating with a high carbon content on the surface;

2 – corresponds to the coating and oxidized wear products of the substrate;

3 – refers to the substrate material.

In figure 4, *b* the surface of a steel wedge gate with ESD coating is depicted, accompanied by SEM images of segments within the region of tribological contact following pilot tests. Prior to the tests, ESD coatings were subjected to lapping on a lapping plate utilizing 6 μm dispersed diamond powder, achieving a roughness of 500 nm. The SEM image of the ESD-coated part surface exhibits two distinctive areas with varying contrast: the first, appearing as light gray, corresponds

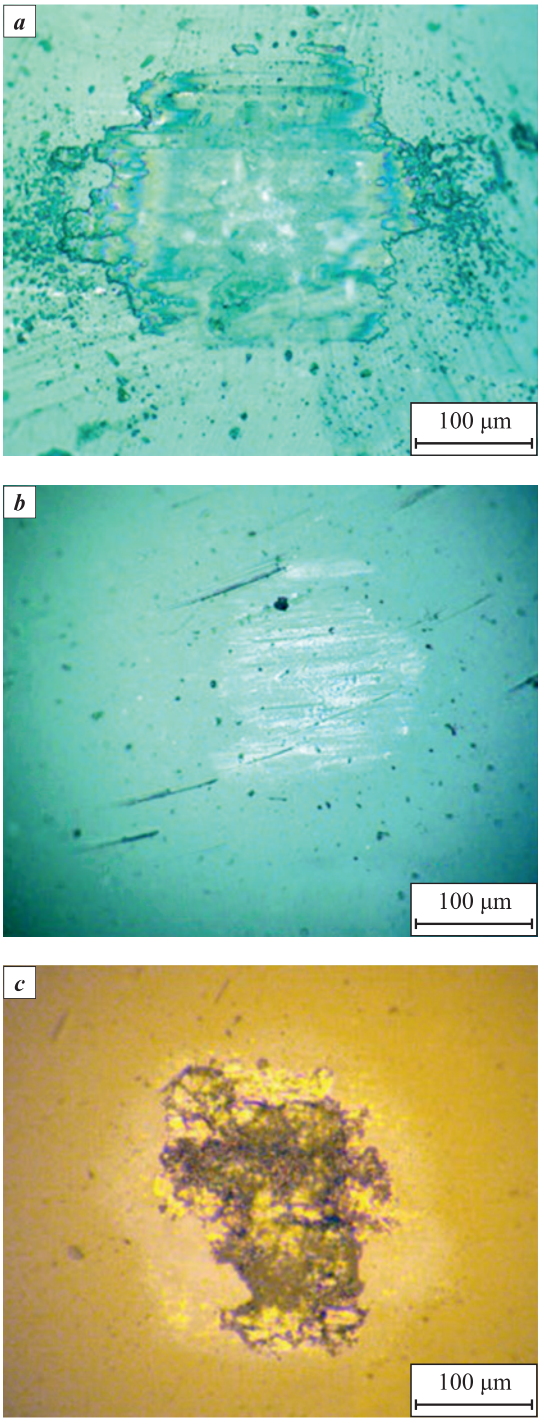

Fig. 3. Micrographs of wear areas of the counterbody after tribological testing of the MS (***a***), ESD coatings (***b***) and the steel substrate (***c***)

Рис. 3. Микрофотографии участков износа контртела после испытания покрытий МР (***a***), ЭИЛ (***b***) и стальной подложки (***c***)

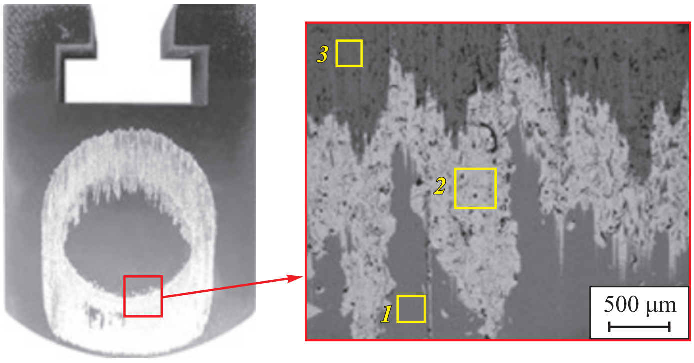

Area	Ta	C	Si	Zr	O	Fe	Cr	Cu	Ni
1	8	82	10	1	–	–	–	–	–
2	14	58	15	2	8	3	–	–	–
3	–	39	–	–	3	44	10	2	2

a

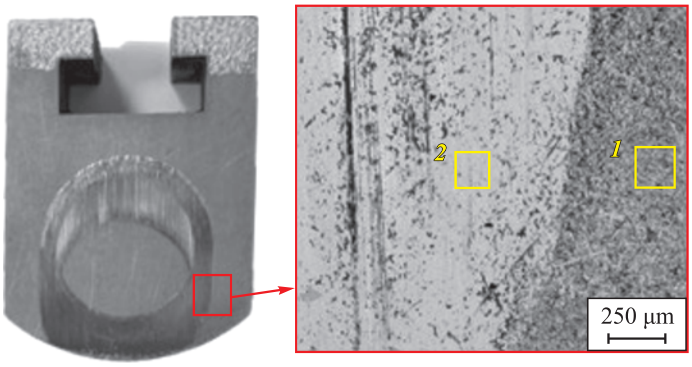

Area	Ta	C	Cr	Mo	Ni	Fe	Si	Cu
1	10	11	9	2	1	67	–	–
2	–	–	16	–	4	76	1	3

b

Fig. 4. Appearance of coated parts after pilot tests, SEM images and composition (at. %) of tribocontact areas for MS (***a***) and ESD (***b***) coatings

Рис. 4. Внешний вид деталей с покрытием после опытно-промышленных испытаний и СЭМ-микрофотографии с указанием состава (ат. %) участков трибоконтакта для покрытий МР (***a***) и ЭИЛ (***b***)

to the worn surface of the steel sample; the second, appearing as dark gray, corresponds to the coating with the following composition in at. %: 10 Ta, 11 C, 67 Fe, 9 Cr, 2 Mo and 1 Ni. Within the region of tribological contact, wear products emerged, consisting of a blend of iron oxide and chromium. These wear products were incorporated into scratches through the frictional process (as depicted in Fig. 4, *b*).

Consequently, no differences were observed in the wear mechanism between the MS and ESD coatings. The thickness of the coating stands out as a pivotal factor influencing wear resistance. The ESD coating, boasting a greater thickness, exhibited the most favorable wear resistance. An advantage of MS coatings lies in the elimination of the need for additional smoothing machining.

Conclusions

1. Ta–Zr–Si–B–C and TaC–Fe–Cr–Mo–Ni coatings based on tantalum carbide were successfully manufactured using magnetron sputtering and electrospark deposition. The MS coating 7 μm thick consisted of $TaSi_2$-based amorphous matrix with dissolved zirconium and boron and TaC crystallites up to 3 nm in size. Meanwhile, the ESD coating 54 μm thick had an alpha-iron matrix and TaC crystallites of up to 30 nm.

2. The TaC concentration in the MS coating exhibited a 30 % increase compared to the ESD coating, consequently endowing it with higher hardness ($H = 28$ GPa versus 10 GPa).

3. Both coatings exhibited a low friction coefficient of 0.15. The minimized wear was below

10^{-7} $mm^3/(N \cdot m)$, while for the steel substrate, it measured $1.2 \cdot 10^{-3}$ $mm^3/(N \cdot m)$. The application of the developed MS and ESD coatings led to a substantial fivefold reduction in the friction coefficient and an enhancement of the service life of the steel wedge gate valve by 25 and 70 %, respectively.

References / Список литературы

1. Barile C., Casavola C., Pappalettera G., Renna G. Advancements in electrospark deposition (ESD) technique: A short review. *Coatings*. 2022;12(10):1536. https://doi.org/10.3390/coatings12101536

2. Kelly P.J., Arnell R.D. Magnetron sputtering: A review of recent developments and applications. *Vacuum*. 2000;56(3):159–172. https://doi.org/10.1016/S0042-207X(99)00189-X

3. Kumar S., Singh R., Singh T.P., Sethi B.L. Surface modification by electrical discharge machining: A review. *Journal of Materials Processing Technology*. 2009; 209(8):3675–3687. https://doi.org/10.1016/j.jmatprotec.2008.09.032

4. Chen Z., Zhou Y. Surface modification of resistance welding electrode by electro-spark deposited composite coatings: Part I. Coating characterization. *Surface and Coatings Technology*. 2006;201(3-4):1503–1510. https://doi.org/10.1016/j.surfcoat.2006.02.015

5. Kudryashov A.E., Zamulaeva E.I., Levashov E.A., Manakova O.S., Petrzhik M.I. Application of electrospark deposition process and modified SHS electrode materials to improve the endurance of hot mill rolls. Part 1. Features of coating formation on SPHN-60 white cast iron substrates. *Surface Engineering and Applied Electrochemistry*. 2019;55(4):390–401. https://doi.org/10.3103/S1068375519040057

Кудряшов А.Е., Замулаева Е.И., Левашов Е.А., Манакова О.С., Петржик М.И. Применение технологии электроискрового легирования и модифицированных СВС-электродных материалов для повышения стойкости прокатных валков стана горячей прокатки. Ч. 1. Особенности формирования покрытий на подложках из белого чугуна СПХН-60. *Электронная обработка материалов*. 2018;54(5):43–55. https://doi.org/10.5281/zenodo.1464851

6. Wang B., Wei S., Guo L., Wang Y., Liang Y., Xu B., Pan F., Tang A., Chen X. Effect of deposition parameters on properties of TiO_2 films deposited by reactive magnetron sputtering. *Ceramics International*. 2017;43(14):10991–10998. https://doi.org/10.1016/j.ceramint.2017.05.139

7. Wenbin F., Mingjiang D., Chunbei W., Mingchun Z., Liang H., Huijun H., Songsheng L. Magnetron sputtering preparation and properties of $SiC/MoSi_2$ oxidation protective coating for carbon/carbon composites prepared. *Rare Metallurgical and Materials Engineering*. 2016;45(10):2543–2548. https://doi.org/10.1016/S1875-5372(17)30031-0

8. Kiryukhantsev-Korneev Ph.V., Sheveyko A.N., Shvindina N.V., Levashov E.A., Shtansky D.V. Comparative study of Ti–C–Ni–Al, Ti–C–Ni–Fe, and Ti–C–Ni–Al/Ti–C–Ni–Fe coatings produced by magnetron sputtering, electro-spark deposition, and a combined two-step process. *Ceramics International*. 2018;44(7):7637–7646. https://doi.org/10.1016/j.ceramint.2018.01.187

9. Kudryashov A.E., Zamulaeva E.I., Levashov E.A., Kiryukhantsev-Korneev Ph.V., Sheveyko A.N., Shvindina N.V. Application of electrospark deposition and modified SHS electrode materials to improve the endurance of hot mill rolls. Part 2. Structure and properties of the formed coatings. *Surface Engineering and Applied Electrochemistry*. 2019;55(5): 502–513. https://doi.org/10.3103/S1068375519050089

Кудряшов А.Е., Замулаева Е.И., Левашов Е.А., Кирюханцев-Корнеев Ф.В., Шевейко А.Н., Швындина Н.В. Применение технологии электроискрового легирования и модифицированных СВС-электродных материалов для повышения стойкости прокатных валков стана горячей прокатки. Ч. 2. Структура и свойства сформированных покрытий. *Электронная обработка материалов*. 2019;55(2):10–22. https://doi.org/10.5281/zenodo.2629552

10. Soma Raju K.R.C., Faisal N.H., Srinivasa Rao D., Joshi S.V., Sundararajan G. Electro-spark coatings for enhanced performance of twist drills. *Surface and Coatings Technology*. 2008;202(9):1636–1644. https://doi.org/10.1016/j.surfcoat.2007.07.084

11. Aksenov L.B., Petrov V.M., Kudryashov A.E., Galyshev A.A. Comparative wear resistance of electrospark alloying coatings using SHS electrodes with nanodispersed modifiers. *Metallobrabotka*. 2010;3(57):15–19. (In Russ.).

Аксенов Л.Б., Петров В.М., Кудряшов А.Е., Галышев А.А. Сравнительная износостойкость покрытий электроискрового легирования с применением СВС-электродов с нанодисперсными модификаторами. *Металлообработка*. 2010;3(57):15–19.

12. Fomin A.A., Fedoseev M.E., Palkanov P.A., Aman A., Koshuro V.A., Shumilin Kh.I. Induction-thermal treatment of steel punches with metal-ceramic coatings and limit strain diagrams for steel 45. *Vestnik SGTU*. 2020;1(84): 87–92. (In Russ.).

Фомин А.А., Федосеев М.Е., Палканов П.А., Аман А., Кошуро В.А., Шумилин Х.И. Индукционно-термическая обработка стальных пуансонов с металлокерамическими покрытиями и диаграммы предельных деформаций для стали 45. *Вестник СГТУ*. 2020;1(84):87–92.

13. Yeldose B.C., Ramamoorthy B. An investigation into the high performance of TiN-coated rollers in burnishing process. *Journal of Materials Processing Technology*. 2008;207(1-3):350–355. https://doi.org/10.1016/j.jmatprotec.2008.06.058

14. Kumar C.S., Urbikain G., López de Lacalle L.N., Gangopadhyay S., Fernandes F. Investigating the effect of novel self-lubricant TiSiVN films on topography, diffusion and oxidation phenomenon at the chip-tool interface during dry machining of Ti–6Al–4V alloy. *Tribology International*. 2023;186:108604. https://doi.org/10.1016/j.triboint.2023.108604

15. Schalk N., Tkadletz M., Mitterer C. Hard coatings for cutting applications: Physical vs. chemical vapor deposition and future challenges for the coatings community. *Surface and Coatings Technology*. 2022;429:127949. https://doi.org/10.1016/j.surfcoat.2021.127949

16. Kiryukhantsev-Korneev F.V., Sheveiko A.N., Komarov V.A., Blanter M.S., Skryleva E.A., Shirmanov N.A., Levashov E.A., Shtansky D.V. Nanostructured Ti–Cr–B–N and Ti–Cr–Si–C–N coatings for hard-alloy cutting tools. *Russian Journal of Non-Ferrous Metals*. 2011; 52(3):311–318. https://doi.org/10.3103/S1067821211030138

Кирюханцев-Корнеев Ф.В., Шевейко А.Н., Комаров В.А., Блантер М.С., Скрылёва Е.А., Ширманов Н.А., Левашов Е.А., Штанский Д.В. Наноструктурные покрытия Ti–Cr–B–N и Ti–Cr–Si–C–N для твердосплавного режущего инструмента. *Известия вузов. Порошковая металлургия и функциональные покрытия*. 2010;(2):39–47.

17. Zeng X.T., Zhang S., Muramatsu T. Comparison of three advanced hard coatings for stamping applications. *Surface and Coatings Technology*. 2000;127(1):38–42. https://doi.org/10.1016/S0257-8972(99)00668-4

18. Berlin E.V., Grigoriev V.Yu., Ivanov A.V., Isaenkova M.G., Klyukova K.E., Stolbov S.D. Structure of the protective chromium coating obtained by a thermal evaporation method in a magnetron discharge on the cladding tube from E110 alloy. *Tsvetnye Metally*. 2019;(4):33–40. (In Russ.). https://doi.org/10.17580/tsm.2019.04.04

Берлин Е.В., Григорьев В.Ю., Иванов А.В., Исаенкова М.Г., Клюкова К.Е., Столбов С.Д. Структура защитного хромового покрытия, полученного методом термического испарения в магнетронном разряде на оболочечных трубах из сплава Э110. *Цветные металлы*. 2019;(4):33–40. https://doi.org/10.17580/tsm.2019.04.04

19. Kratochvílová I., Celbová L., Ashcheulov P., Kopeček J., Klimša L., de Prado E., Dragounová K. A., Luštinec J., Macák J., Sajdl P., Škoda R., Bulíř J. Polycrystalline diamond and magnetron sputtered chromium as a double coating for accident-tolerant nuclear fuel tubes. *Journal of Nuclear Materials*. 2023;578:154333. https://doi.org/10.1016/j.jnucmat.2023.154333

20. Ryzhenkov A.V., Mednikov A.F., Grigoriev S.V., Tkhabisimov A.B., Kachalin G.V., Loginova N.A., Milovanov O.Yu. The use of ion-plasma technologies for the formation of coatings to reduce corrosion and abrasive wear of tubular heating surfaces of a biofuel boiler. *Teploenergetika*. 2023;(10):34–44. (In Russ.). https://doi.org/10.56304/S0040363623100089

Рыженков А.В., Медников А.Ф., Григорьев С.В., Тхабисимов А.Б., Качалин Г.В., Логинова Н.А., Милованов О.Ю. Применение ионно-плазменных технологий формирования покрытий для снижения коррозионного и абразивного износа трубных поверхностей нагрева биотопливного котла. *Теплоэнергетика*. 2023;(10): 34–44. https://doi.org/10.56304/S0040363623100089

21. Yang S., Gao S., Xue W., Wu B., Cheng H., Duan D. Epitaxial growth and oxidation behavior of the NiCoCrAl YTa/Y_2O_3 coating on a nickel-based single-crystal superalloy blade tips, produced by electro spark deposition. *Journal of Alloys and Compounds*. 2023;931:167600. https://doi.org/10.1016/j.jallcom.2022.167600

22. Belyakov A.V., Gorbachev A.N., Mikhailov V.V., Reutov B.F., Fokin A.A. Installations for producing electrospark erosion- and abrasion-resistant coatings on the blades of steam turbines of thermal and nuclear power plants. *Surface Engineering and Applied Electrochemistry*. 2017;53(3):274–284. https://doi.org/10.3103/S1068375517030036

Беляков А.В., Горбачев А.Н., Михайлов В.В., Реутов Б.Ф., Фокин А.А. Установки для формирования эрозионно- и абразивостойких электроискровых покрытий на лопатках паровых турбин тепловых и атомных электростанций. *Электронная обработка материалов*. 2016; 52(5):79–89.

23. Tarel'nik V.B., Paustovskii A.V., Tkachenko Y.G., Martsinkovsky V.S., Konoplyanchenko E.V., Antoshevsky K. Electric-spark coatings on a steel base and contact surface for optimizing the working characteristics of babbitt friction bearings. *Surface Engineering and Applied Electrochemistry*. 2017;53(3):285–294. https://doi.org/10.3103/S1068375517030140

Тарельник В.Б., Паустовский А.В., Ткаченко Ю.Г., Марцинковский В.С., Коноплянченко Е.В., Антошевский К. Электроискровые покрытия на стальной основе и контактной поверхности для оптимизации рабочих характеристик баббитовых подшипников скольжения. *Электронная обработка материалов*. 2017;53(1):37–46. https://doi.org/10.5281/zenodo.1048993

24. Ivanov V.I., Burumkulov F.K. On electrodeposition of thick coatings of increased continuity. *Surface Engineering and Applied Electrochemistry*. 2014;50(5):377–383. https://doi.org/10.3103/S1068375514050056

Иванов В.И., Бурумкулов Ф.Х. Об электроискровом способе нанесения толстослойных покрытий повышенной сплошности. *Электронная обработка материалов*. 2014;50(5):7–12.

25. Velichko S.A., Senin P.V., Ivanov V.I., Martynov A.V., Chumakov P.V. Formation of thick layer electro-spark coatings for restoring worn-out parts of power hydraulic cylinders. *Surface Engineering and Applied Electrochemistry*. 2017;53(2):116–123. https://doi.org/10.3103/S1068375517020119

Величко С.А., Сенин П.В., Иванов В.И., Чумаков П.В. Формирование толстослойных электроискровых покрытий для восстановления изношенных деталей силовых гидроцилиндров. *Электронная обработка материалов*. 2016;52(5):13–20.

26. Burumkulov F.Kh., Ivanov V.I., Velichko S.A., Ionov P.A., Suldin S.P. Increasing of reliability of hydraulic pumps NSh-U by electric spark alloying of the working surfaces of friction couples. *Elektronnaya obrabotka materialov*. 2005;6(41):13–18. (In Russ.).

Бурумкулов Ф.Х., Иванов В.И., Величко С.А., Ионов П.А., Сульдин С.П. Повышение надежности гидронасосов типа НШ-У электроискровым легированием рабочих поверхностей пар трения. *Электронная обработка материалов*. 2005;6(41):13–18.

27. Kuptsov K.A., Antonyuk M.N., Sheveyko A.N., Bondarev A.V., Ignatov S.G., Slukin P.V., Dwivedi P., Fraile A., Polcar T., Shtansky D.V. High-entropy Fe–Cr–Ni–Co–(Cu) coatings produced by vacuum electro-spark deposition for marine and coastal applications. *Surface and Coatings Technology*. 2023;453:129136. https://doi.org/10.1016/j.surfcoat.2022.129136

28. Korotaev D.N., Ivanova E.V. Improvement of electrospark deposition technology of steel units for drilling rigs and mining equipment. *Geologiya i razvedka*. 2022;64(1):88–97. (In Russ.).
https://doi.org/10.32454/0016-7762-2022-64-1-88-97

Коротаев Д.Н., Иванова Е.В. Совершенствование технологии электроискрового легирования стальных деталей буровых установок и горнодобывающего оборудования. *Известия высших учебных заведений. Геология и разведка*. 2022;64(1):88–97.
https://doi.org/10.32454/0016-7762-2022-64-1-88-97

29. Plakhotnikova E.V., Eliseeva T.A. Analysis of the causes of malfunction of electric shut-off valves. *Izvestiya TulGU*. 2013;(11):352–361. (In Russ.).

Плахотникова Е.В., Елисеева Т.А. Анализ причин нарушения работоспособности электроприводной запорной арматуры. *Известия ТулГУ*. 2013;(11):352–361.

30. Vasiliev A.S., Sukhanov Yu.V., Shchukin P.O., Galaktionov O.N. Improving the performance of shut-off pipeline valves. *Inzhenernyi vestnik Dona*. 2014;(3):11. (In Russ.).

Васильев А.С., Суханов Ю.В., Щукин П.О., Галактионов О.Н. Совершенствование эксплуатационных показателей запорной трубопроводной арматуры. *Инженерный вестник Дона*. 2014;(3):11.

31. Rasulov V.A. To the question of the reliability and durability of pipeline wedge valves. *Vestnik armaturostroitelya*. 2016;5(33):52–53. (In Russ.).

Расулов В.А. К вопросу о надежности и долговечности трубопроводных клиновых задвижек. *Вестник арматуростроителя*. 2016;5(33):52–53.

32. Kazantsev M. N., Flegentov I. A., Petelin A. N. Ways to improve the reliability of shut-off valves for main pipelines (on the example of slide gate valves). *Neftegazovoe delo*. 2016;14(4):75–81. (In Russ.).

Казанцев М.Н., Флегентов И.А. Петелин А.Н. Пути повышения надежности запорной арматуры для магистральных трубопроводов (на примере задвижек шиберных). *Нефтегазовое дело*. 2016;14(4):75–81.

33. Kachalin G.V., Ryzhenkov A.V., Mednikov A.F. Modern ion-plasma technologies for hardening elements of fittings for fuel and energy complex equipment. *Neftegaz.RU*. 2015;(1-2):38–41. (In Russ.).

Качалин Г.В., Рыженков А.В., Медников А.Ф. Современные ионно-плазменные технологии для упрочнения элементов арматуры оборудования ТЭК. *Neftegaz.RU*. 2015;(1-2):38–41.

34. Luo H., Yazdi M. A., Chen S., Sun H., Gao F., Heintz O., Monteynard A., Sanchette F., Billard A. Structure, mechanical and tribological properties, and oxidation resistance of TaC/a-C:H films deposited by high power impulse magnetron sputtering. *Ceramics International*. 2022;46(16, Part A):24986–25000.
https://doi.org/10.1016/j.ceramint.2020.06.284

35. Lasfargues H., Glechner T., Koller C.M., Paneta V., Primetzhofer D., Kolozsvári S., Holec D., Riedl H., Mayrhofer P.H. Non-reactively sputtered ultra-high temperature Hf–C and Ta–C coatings. *Surface and Coatings Technology*. 2017;309:436–444.
https://doi.org/10.1016/j.surfcoat.2016.11.073

36. Kuptsov K.A., Antonyuk M.N., Bondarev A.V., Sheveyko A.N., Shtansky D.V. Electrospark deposition of wear and corrosion resistant Ta(Zr)C–(Fe,Mo,Ni) coatings to protect stainless steel from tribocorrosion in seawater. *Wear*. 2021;486-487:204094.
https://doi.org/10.1016/j.wear.2021.204094

37. Du S., Wen M., Yang L., Ren P., Meng Q., Zhang K., Zheng W. Structural, hardness and toughness evolution in Si-incorporated TaC films. *Ceramics International*. 2018;44(8):9318–9325.
https://doi.org/10.1016/j.ceramint.2018.02.144

38. Kiryukhantsev-Korneev P.V. Sytchenko A.D. Vorotilo S.A. Klechkovskaya V.V. Lopatin V.Y. Levashov E.A. Structure, oxidation resistance, mechanical, and tribological properties of N- and C-Doped Ta–Zr–Si–B hard protective coatings obtained by reactive D.C. magnetron sputtering of TaZrSiB ceramic cathode. *Coatings*. 2020;10(10):946.
https://doi.org/10.3390/coatings10100946

39. Veprek S., Veprek-Heijman G.J., Karvankova P., Prochazka J. Different approaches to superhard coatings and nanocomposites. *Thin Solid Films*. 2005;476(1):1–29.
https://doi.org/10.1016/j.tsf.2004.10.053

40. Vorotilo S., Levashov E.A., Kurbatkina V. V., Patsera E.I., Loginov P.A., Lopatin V.Y., Orekhov A.S. Theoretical and experimental study of combustion synthesis of micro-gradient ULTRA high-temperature ceramics in Zr–Ta–Si–B system *Journal of the European Ceramic Society*. 2021;41(9):4728–4746.
https://doi.org/10.1016/j.jeurceramsoc.2021.03.008

41. Kiryukhantsev-Korneev P. V., Sytchenko A.D., Sviridova T.A., Sidorenko D.A., Andreev N. V., Klechkovskaya V.V., Polčak J., Levashov E.A. Effects of doping with Zr and Hf on the structure and properties of Mo–Si–B coatings obtained by magnetron sputtering of composite targets. *Surface and Coatings Technology*. 2022;442:128141.
https://doi.org/10.1016/j.surfcoat.2022.128141

42. Kiryukhantsev-Korneev P.V., Sytchenko A.D., Gorshkov V.A., Loginov P.A, Sheveyko A.N., Nozhkina A.V., Levashov E.A. Complex study of protective Cr_3C_2–NiAl coatings deposited by vacuum electro-spark alloying, pulsed cathodic arc evaporation, magnetron sputtering, and hybrid technology. *Ceramics International*. 2022;48(8):10921–10931.
https://doi.org/10.1016/j.ceramint.2021.12.311

43. Kiryukhantsev-Korneev P.V., Pierson J.F., Bychkova M.Y., Manakova O.S., Levashov E.A., Shtansky D.V. Comparative study of sliding, scratching, and impact-loading behavior of hard CrB_2 and Cr–B–N Films. *Tribology Letters*. 2016;63(3):44.
https://doi.org/10.1007/s11249-016-0729-0

44. Levashov E.A., Shtansky D.V., Kiryukhantsev-Korneev Ph.V., Petrzhik M.I., Tyurina M.Y., Sheveyko A.N. Multifunctional nanostructured coatings: Formation, structure, and the uniformity of measuring their mechanical and tribological properties. *Russian Metallurgy (Metally)*. 2010(10);917–935.
https://doi.org/10.1134/S0036029510100113

45. Abadias G., Chason E., Keckes J., Sebastiani M., Thompson G.B., Barthel E., Doll G.L., Murray C.E., Stoessel C.H., Martinu L. Stress in thin films and coatings: Current status, challenges, and prospects. *Journal of Vacuum*

Science & Technology A. Vacuum Surfaces and Films. 2018;36(2):020801. https://doi.org/10.1116/1.5011790

46. Paustovskii A.V., Gubin Y.V. Stresses in coatings obtained by electro-spark alloying and laser processing (review). *Journal of Materials Science*. 1997;33(6):770–776. https://doi.org/10.1007/BF02355555

47. Chen Z., Zhou N. Surface modification of resistance welding electrodes by electro-spark deposited coatings. Part I. Coating characterization. *Surface and Coatings Technology*. 2006;201(3-4):1503–1510. https://doi.org/10.1016/j.surfcoat.2006.02.015

48. StainlessSteel PH1: нержавеющая сталь. https://can-touch.ru/3d-printing-stainlesssteel-ph1/ (Дата обращения 07.05.2023).

49. Hu J., Li H., Li J., Huang J., Kong J., Zhu H., Xiong D. Structure, mechanical and tribological properties of TaC_x composite films with different graphite powers. *Journal of Alloys and Compounds*. 2020;832:153769. https://doi.org/10.1016/j.jallcom.2020.153769

50. Du S., Zhang K., Wen M., Qin Y., Li R., Jin H., Bao X., Ren P., Zheng W. Optimizing the tribological behavior of tantalum carbide coating for the bearing in total hip joint replacement. *Vacuum*. 2018;150:222–231. https://doi.org/10.1016/j.vacuum.2018.01.050

51. Pogrebnjak A.D., Beresnev V.M. Hard nanocomposite coatings, their structure and properties. *Nanocomposites – New Trends Dev*. 2012;517:1–38. https://doi.org/10.5772/50567

52. Musil J., Zeman P., Baroch P. Hard Nanocomposite Coatings. *Comprehensive Materials Processing*. 2014;4: 325–353. https://doi.org/10.1016/B978-0-08-096532-1.00416-7

53. Sánchez-López J.C., Martínez-Martínez D., López-Cartes C., Fernández A. Tribological behaviour of titanium carbide/amorphous carbon nanocomposite coatings: From macro to the micro-scale. *Surface and Coatings Technology*. 2008;202(16):4011–4018. https://doi.org/10.1016/j.surfcoat.2008.02.012

Information about the Authors

Alina D. Sytchenko – Junior Research Scientist of the Laboratory “In situ Diagnostics of Structural Transformations” of Scientific-Educational Center of Self-Propagating High-Temperature Synthesis (SHS-Center), MISIS–ISMAN, National University of Science and Technology (NUST) MISIS.
ORCID: 0000-0002-8668-5877
E-mail: alina-sytchenko@yandex.ru

Maria N. Fatykhova – Junior Research Scientist of the Laboratory “In situ Diagnostics of Structural Transformations” of SHS-Center, MISIS–ISMAN.
ORCID: 0000-0001-6817-5999
E-mail: mariya.antonyuck@ya.ru

Victor P. Kuznetsov – Dr. Sci. (Eng.), Prof., Department of Heat Treatment and Physics of Metals, Ural Federal University named after the First President of Russia B.N. Yeltsin.
ORCID: 0000-0001-8949-6345
E-mail: wpkuzn@mail.ru

Konstantin A. Kuptsov – Cand. Sci. (Eng.), Senior Researcher of SHS-Center, MISIS–ISMAN.
ORCID: 0000-0003-2585-0733
E-mail: kuptsov.k@gmail.com

Mikhail I. Petrzhik – Dr. Sci. (Eng.), Prof., Department of Powder Metallurgy and Functional Coatings, NUST MISIS; Leading Researcher of the Laboratory «In situ diagnostics of structural transformations” of SHS-Center, MISIS–ISMAN.
ORCID: 0000-0002-1736-8050
E-mail: mi_p@mail.ru

Alexander E. Kudryashov – Cand. Sci. (Eng.), Leading Researcher of the Laboratory «In situ diagnostics of structural transformations” of SHS-Center, MISIS–ISMAN.
ORCID: 0000-0001-6222-4497
E-mail: aekudr@yandex.ru

Philipp V. Kiryukhantsev-Korneev – Dr. Sci. (Eng.), Associate Prof., Department of Powder Metallurgy and Functional Coatings, NUST MISIS; Head of the Laboratory «In situ diagnostics of structural transformations” of SHS-Center, MISIS–ISMAN.
ORCID: 0000-0003-1635-4746
E-mail: kiruhancev-korneev@yandex.ru

Сведения об авторах

Алина Дмитриевна Сытченко – мл. науч. сотрудник лаборатории «In situ диагностика структурных превращений» научно-учебного центра (НУЦ) СВС, МИСИС–ИСМАН, Национальный исследовательский технологический университет (НИТУ) «МИСИС».
ORCID: 0000-0002-8668-5877
E-mail: alina-sytchenko@yandex.ru

Мария Николаевна Фатыхова – мл. науч. сотрудник лаборатории «In situ диагностика структурных превращений» НУЦ СВС, МИСИС–ИСМАН.
ORCID: 0000-0001-6817-5999
E-mail: mariya.antonyuck@ya.ru

Виктор Павлович Кузнецов – д.т.н., профессор кафедры термообработки и физики металлов, Уральский федеральный университет имени первого Президента России Б.Н. Ельцина.
ORCID: 0000-0001-8949-6345
E-mail: wpkuzn@mail.ru

Константин Александрович Купцов – к.т.н., ст. науч. сотрудник НУЦ СВС, МИСИС–ИСМАН.
ORCID: 0000-0003-2585-0733
E-mail: kuptsov.k@gmail.com

Михаил Иванович Петржик – д.т.н., профессор кафедры порошковой металлургии и функциональных покрытий НИТУ МИСИС; вед. науч. сотрудник лаборатории «In situ диагностика структурных превращений» НУЦ СВС, МИСИС–ИСМАН.
ORCID: 0000-0002-1736-8050
E-mail: mi_p@mail.ru

Александр Евгеньевич Кудряшов – к.т.н., вед. науч. сотрудник лаборатории «In situ диагностика структурных превращений» НУЦ СВС, МИСИС–ИСМАН.
ORCID: 0000-0001-6222-4497
E-mail: aekudr@yandex.ru

Филипп Владимирович Кирюханцев-Корнеев – д.т.н., доцент кафедры порошковой металлургии и функциональных покрытий НИТУ МИСИС; зав. лабораторией «In situ диагностика структурных превращений» НУЦ СВС, МИСИС–ИСМАН.
ORCID: 0000-0003-1635-4746
E-mail: kiruhancev-korneev@yandex.ru

Contribution of the Authors

A. D. Sytchenko – conducted structural studies, analyzed the research results, authored the manuscript, and formulated conclusions.

M. N. Fatykhova – conducted tribological studies, analyzed the research results, authored the manuscript, and formulated conclusions.

V. P. Kuznetsov – organized pilot tests of products with coatings.

K. A. Kuptsov – deposition of coatings by electrospark deposition in a vacuum, manuscript revision.

M. I. Petrzhik – determined mechanical characteristics of the coatings.

A. E. Kudryashov – adjusted energy modes of electrospark deposition

Ph. V. Kiryukhantsev-Korneev – applied coatings by magnetron sputtering, provided scientific guidance, and revised the manuscript.

Вклад авторов

А. Д. Сытченко – проведение структурных исследований, анализ результатов исследований, подготовка текста, формулировка выводов.

М. Н. Фатыхова – проведение трибологических исследований, анализ результатов исследований, подготовка текста, формулировка выводов.

В. П. Кузнецов – организация опытно-промышленных испытаний изделий с покрытиями.

К. А. Купцов – нанесение покрытий методом электроискрового осаждения в вакууме, корректировка текста.

М. И. Петржик – определение механических характеристик покрытий.

А. Е. Кудряшов – отработка энергетических режимов электроискрового осаждения.

Ф. В. Кирюханцев-Корнеев – нанесение покрытий методом магнетронного распыления, научное руководство, корректировка текста статьи.

Received 19.05.2023
Revised 20.06.2023
Accepted 26.06.2023

Статья поступила 19.05.2023 г.
Доработана 20.06.2023 г.
Принята к публикации 26.06.2023 г.

Зарегистрирован Федеральной службой по надзору
в сфере связи, информационных технологий
и массовых коммуникаций.
Свидетельство о регистрации **ПИ № ФС77-79230**

Журнал распространяется агентством «Урал-Пресс»
Подписной индекс: 80752 (печатная версия)
05108 (электронная версия)